Dipartimento di

SCIENZE BIOMEDICHE, ODONTOIATRICHE E DELLE IMMAGINI MORFOLOGICHE E FUNZIONALI

CORSO DI DOTTORATO DI RICERCA IN:

BIOINGEGNERIA APPLICATA ALLE SCIENZE MEDICHE

CICLO XXXVII

INNOVATIVE BIOSENSING METHODS FOR NUCLEIC ACIDS DETECTION IN POINT-OF-CARE DEVICES

SSD:CHIM/03 – Chimica Generale ed Inorganica

Tesi redatta con il sostegno finanziario del programma
FSE-REACT-EU, PON “Ricerca e Innovazione” 2014-2020 (D.M. 1061/2021)
Azione IV.4 “Dottorati e contratti di ricerca su tematiche dell'innovazione”

Coordinatore: Ch.mo Prof. Michele Gaeta

Supervisore: Ch.mo Prof.ssa Sabrina Conoci

Dottorando: Paolo Calorenni

ANNO ACCADEMICO
2023/2024

Ad Annamaria…

CONTENTS

Introduction

The analysis of nucleic acids (NA) introduced a disruptive innovation in healthcare, opening towards high throughput diagnosis and personalized therapies in many fields of medicine including infectious diseases, oncology, pharmacogenomics, genetic diseases, diabetes, forensic, and neurological, cardiovascular diseases.

Conventional methods for NA analysis rely on the Real-Time PCR (Polymerase Chain Reaction) reaction, that represent the gold standard for NA analysis offering a high level of specificity and sensibility. The Real-Time PCR works through the cyclic amplification of a specific target sequence through a couple of small complementary oligoribonucleotides (primers), a thermostable DNA Polymerase enzyme and a fluorescent probe, able to label the target sequence during its amplification[1,2].Thanks to the amplification, the number of copies of the NA target is exponentially increased becoming detectable and quantifiable. **Figure 1** reports a typical Real-Time PCR mechanism using specific fluorescent probes for DNA detection.

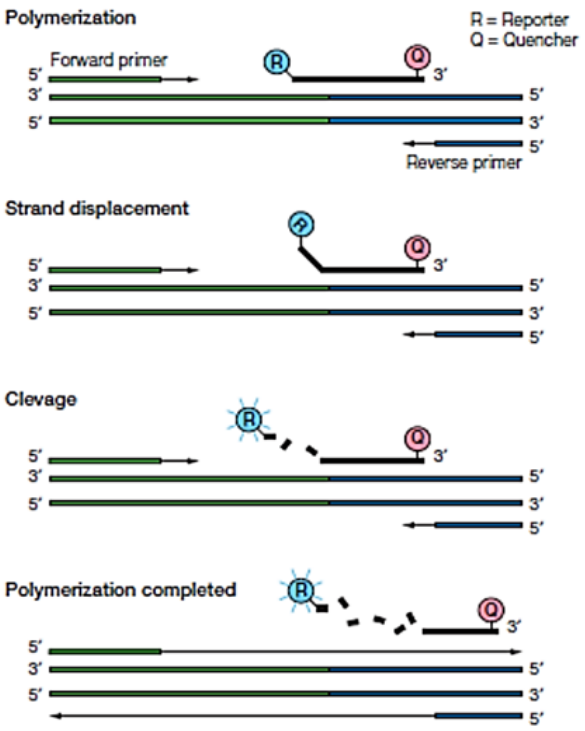

Figure 1. Real-Time PCR mechanism[3].

Within this approach PCR-based methods are widely diffusing in a lot of biomedical fields but their massive use is strongly limited by a series of drawbacks, such as the constrain to specialized laboratories, instruments and staff and the need of long and expensive procedures to perform both the DNA preparation and detection.

To overpass these limitations, a lot of alternative solutions have been introduced so far mostly based on the biosensing approach. Biosensors are analytical systems relying on the synergy between a sensing element (such as enzymes, antibodies, nucleic acids, aptamers, phages, cells etc.), that recognizes and interacts with specific targets producing an input biochemical signal, and a transducer element, that converts the input into an output (electrical, optical, acoustic, etc.) signal used to detect and quantify the targets concentrations[4–6]. Depending on the type of sensing element, biosensors can be very versatile and suitable for a lot of analytical applications, as schemed in **Figure 2.**

Figure 2. Main applications of biosensors.

The interest for biosensors increased significantly over the last fifty years. A Scopus study, indeed, revealed that from 1972 to 2014 the number of publications on biosensors showed an exponential growth[5,7]. This growing attraction was mainly due to the possibility of biosensors to open towards simple, rapid, low-cost and portable analytical solutions that can really improve

the quality of life[5,8,9]. This is the case of the so called genetic Point-of-Care (PoC), consisting in innovative biosensing technologies that empathize the decentralization and simplification of NA analysis. This technologies, indeed, provide a patient-centred diagnostics that can be performed quickly, easily and directly at the patient bed, in the physician office or at home[10,11]. The importance of PoC varies depending on the context. As an example, in intensive care units, PoCs are used to immediately perform a diagnosis and aid in life-saving decisions. At low resources settings, PoCs offer easy-to-use procedures that can be performed regardless of the presence of a laboratory and specialized personell[12]. In primary care settings, PoCs are typically used to prevent unnecessary specialist cares, to guide treatment decisions and to quickly provide reassurance to patients, e.g. excluding a severe disease. Moreover, rapid testing can lead to improved clinical performance as it eliminates potentially long intervals between initial patient examination and discussion of test results[13].

Objective of my Ph.D. thesis was to develop innovative biosensing methods for the detection of nucleic acids and other targets of biomedical interest suitable for PoC applications.

The research has been mainly focused on the molecular biosensing of the nucleic acid kinetoplast (k)DNA of the protozoan *Leishmania infantum* (*L. infantum*), the double-stranded (ds)DNA genome of the bacterium *Pseudomonas aeruginosa* (*P. aeruginosa*) and the single-stranded (ss)RNA genome of the Sars-CoV-2 virus, which are representative of pathogens causing severe infectious disease on human health. As a side activity, I have worked on the development of biosensing methods for the detection of other two biomolecules of diagnostic interest, i.e. microRNA (miRNA) and anti-Aβ peptide antibodies as important biomarkers of the Alzheimer's disease onset.

The reported research activities will be described in the following chapters of my Ph.D. thesis:

1. State-of-the-art of biosensors for biomedical applications.

2. PCR-free biosensing method for the detection of infectious pathogens nucleic acids in a PoC format.

3. Biosensing methods for the detection of Alzheimer's disease associated biomarkers.

CHAPTER 1

State-of-the-art of biosensors for biomedical applications

1. Sensors and biosensors: a background

Sensors are a device that detect different type of biochemical targets by transducing the first chemical interaction into an analytical signal. Sensors consist of three main elements that are schemed in **Figure 1.1**:

1. a sensing element, which is responsible for the biorecognition of the target (or analyte) through a biochemical interaction and a subsequent structural modification producing the input signal.
2. a chemical-physical transducer that converts the input into a detectable and/or quantifiable output signal (electrical, optical, calorimetric, piezoelectric, etc.) for an analytical determination[14] of the target.
3. an electronic system consisting of modules for the output signal amplification, data processing and storage.

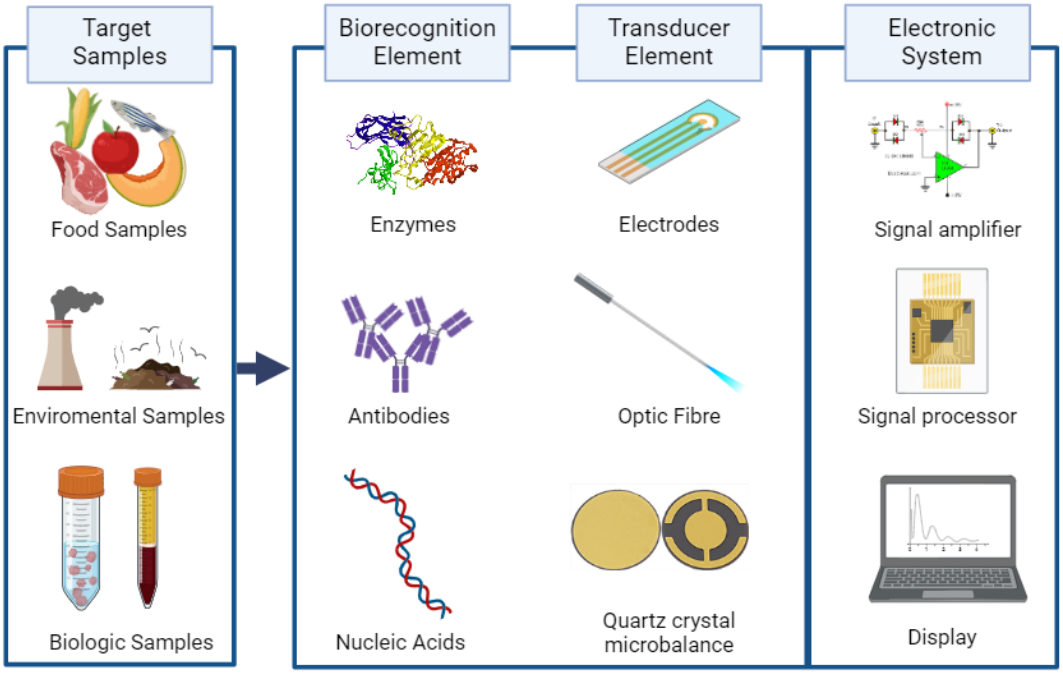

Figure 1.1. Schematic representation of a sensor.

Biosensors were defined as sensors that use specific biochemical reactions mediated by isolated enzymes, immune systems, tissues, organelles, or entire cells to detect target biomolecules via electrical, thermal, or optical signals[15]. IUPAC defines a biosensor as: “a self-contained integrated device capable of

providing specific quantitative or semi-quantitative analytical information using a biological recognition element (biochemical receptor) located in direct spatial contact with a transducer element. A biosensor should be clearly distinguished from a bioanalytical system that requires additional processing steps, such as the addition of reagents. Furthermore, a biosensor should be distinguished from a bio probe that is disposable after a measurement, e.g. single-use, or incapable of continuously monitoring the concentration of the analyte"[16]. The biosensors era started with the development of an amperometric glucose oxidase biosensor published in 1962[17]. This type of biosensor was also the first commercially available biosensor introduced to the market by the Yellow Springs Instrument Company (Ohio, USA) in 1975[18]. There is currently a great interest in research in the field of biosensing, which increased mainly in the last two decades together with the series of potential applications.

Biosensors bring different advantages such as rapid and sensitive detection, portability, low-cost production and possible miniaturization. At a commercial level, biosensors must follow a stringent set of criteria. They must be highly specific and stable for long-term storage. The analysis must proceed without complex pre-treatment. The response should be accurate, precise, reproducible and linear over the entire range of concentrations, with a low noise-to-signal ratio. Depending on their use, they must be biocompatible and able to provide a real-time analysis. As analytical devices, biosensors have already found their application in many fields of human activity, for example in the biological and medical diagnostics[19,20] field and the environmental monitoring[21–24]. Biosensors performances rely on two crucial factors: (i) a sensing and (ii) a transducer element. The general classification of biosensors is based on these two functional elements. Depending on the transducer, biosensors are generally divided into electrochemical, optical, and piezoelectric (mass transport) classes. Electrochemical biosensors work through sensing elements that translate the detected information into an electrical signal proportional to the concentration of the analyte. Optical biosensors rely on the input signal transduction by the absorption, luminescence or scattering analysis. Piezoelectric biosensors have sensing

element attached on a piezoelectric surface so that the interaction with the analyte is transduced into mechanical vibrations, then converted into an electrical signal.

1.1. The sensing element

The primary purpose of the development of a biosensing technology is the choice of the sensing element, which must bring a strong and highly selective affinity towards the analyte of interest. A fundamental understanding of the inherent characteristics of each sensing element is first needed before an in-depth analysis of biosensor performance may occur. More than antibodies, whole cells and bacteriophages, nucleic acids have been widely used as sensing element.

Nucleic acid analysis continues to receive enormous attention from researchers due to its association with various infectious diseases and genetic disorders as well as cancer, which explains the growing need of new type of nucleic acid-based biosensors called genosensors. This technology typically relies on the complementary hybridization between the DNA[25] analyte with appropriate oligonucleotide DNA sequences designed and immobilized on the surface of the biosensor as biorecognition elements[26,27]. This interaction can involve ssDNA, peptide nucleic acids (PNAs)[28,29], locked nucleic acids, G-quadraplexes, aptamers and microRNAs.

An example of DNA-based biosensors was reported by Mao et al.[30], proposing a disposable nucleic acid biosensor (DNAB) for sensitive and low-cost detection of DNA samples in 15 minutes. The device consists of a solid nitrocellulose support and combines the optical properties of gold nanoparticles (Au-NPs), linked to appropriate oligonucleotide probes, and with the efficiency of chromatographic separation. Quantitative detection was performed by reading the intensity of the red bands produced by DNA hybridization with the Au-NP probes with a portable strip reader. The response of the optimized device is highly linear in the target DNA range from 1 to 100 nM, and the Limit-of-Detection (LoD) was estimated at 0.5 nM. The authors

improved the sensitivity of the biosensor by using dual labels with horseradish peroxidase (HRP)-Au-NPs that ensure a rather low detection limit of 50 pM.

A particular type of nucleic acid sensing elements are the aptamers. These are selected by a procedure called Systematic Evolution of Exponential Enrichment Ligands (SELEX)[31] and are single-stranded nucleic acids that possess inner complementary and distinctive binding characteristics for the target analyte capture. Unlike traditional classical[32] hybridization-based nucleic acid assays, aptamers are able to be more specific through Pi bond stacking (π—π), electrostatic interactions, London forces, and hydrogen bonding, often in various combinations. Considering wide variety of targets detected[33–35], aptamers offer the advantages of low cost of synthesis, ease of chemical modification, high thermal stability, and high binding affinities (Kd in low nano- to picomolar ranges). An example is shown in **Figure 1.2**, describing a simple colorimetric assay in which aptamers for Ramos cells were captured between immobilized aptamers on a lateral-flow strip and aptamer-coated gold nanoparticles (AuNP-TD05 Aptamer)[36].

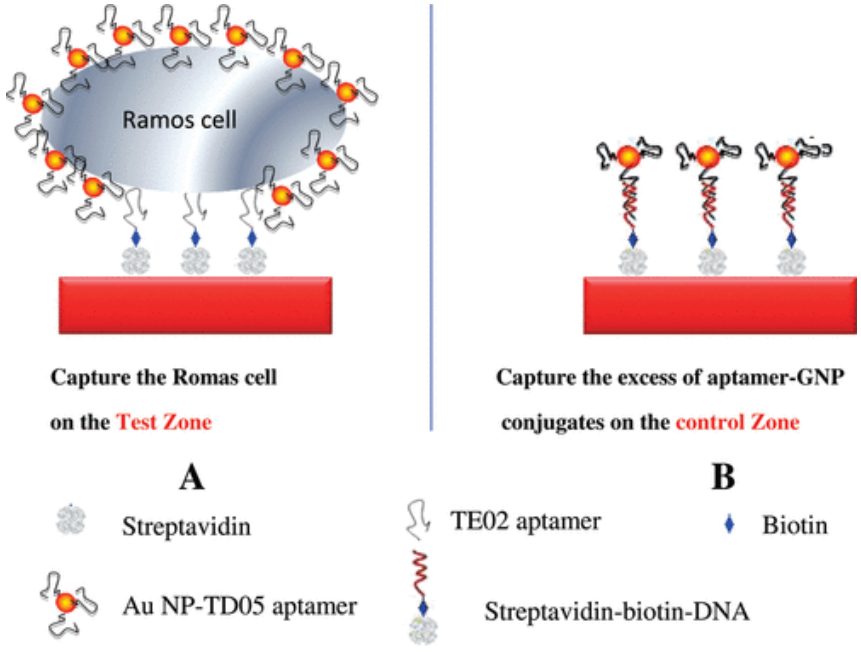

Figure 1.2. Aptamer-based lateral-flow detection of Ramos cells. (**a**) Ramos cell capture on the test line between immobilized aptamer and AuNP-TD05 Aptamer conjugate, and (**b**) hybridization-based capture of excess AuNP-TD05 Aptamer on a control line[36].

The presence of AuNPs resulted in an intense red-colored test line, the intensity of which was correlated with increasing Ramos cells concentration. Aptamers have been coupled with various transduction systems such as electrochemical[37], optical and piezoelectric[38,39] for the detection of a variety of targets.

1.2. Electrochemical biosensors and detection techniques

Among the different biosensor platforms, electrochemical biosensors are probably the most widely used types due to their rapid response, simplicity, and lower costs compared to optical, calorimetric, and piezoelectric biosensors[40]. Furthermore, they allow to operate in complex and turbid media, to use small volumes and to achieve low LoD, between 10^{-7} and 10^{-9} M, by different electroanalytical methods (square wave and cyclic voltammetry, differential pulse voltammetry, chronoamperometry). Furthermore, electrochemical signals in terms of current and potential can be collected using simple, portable, and economical peripheral instruments with low power consumption[41]. Lastly, some electrochemical sensors integrate the biorecognition sensing element into the transducer module (e.g., an electrode or a field-effect transistor), as reported in **Figure 1.3a**, that can be easily miniaturized and batch fabricated on portable devices [42–44], opening towards sensing applications in a PoC format.

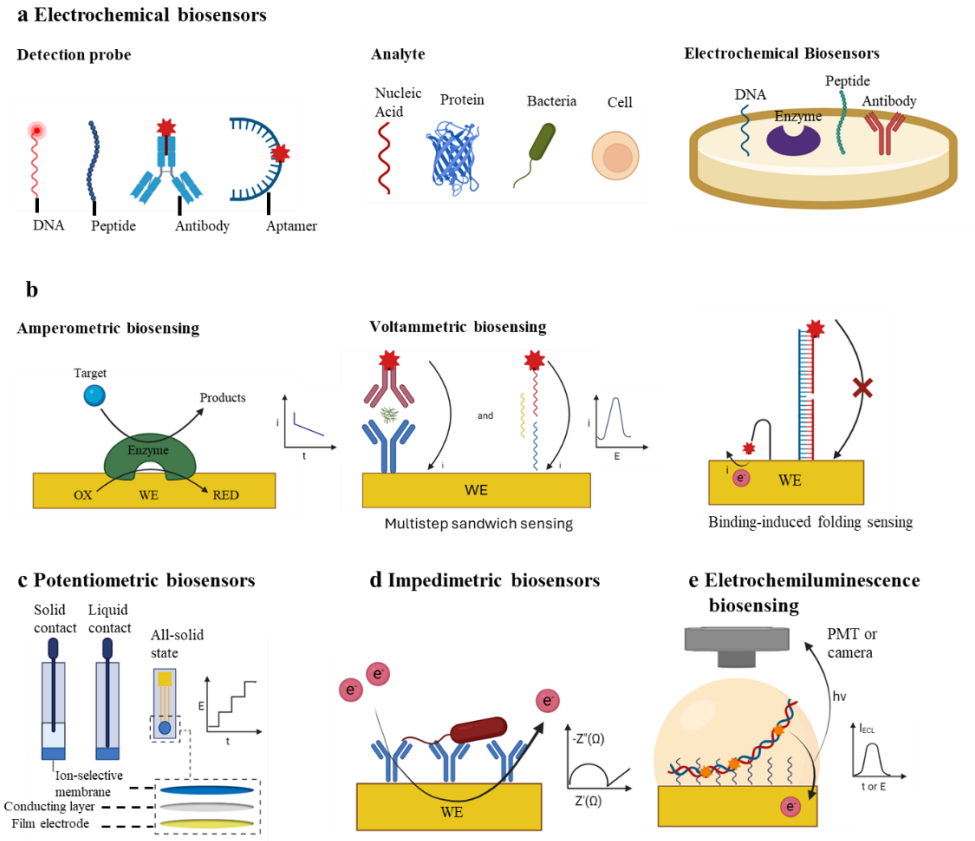

Figure 1.3. Electrochemical biosensors. **a**) Schematic representation of electrochemical biosensors based on different biochemical receptors and detection probes. **b**) Amperometric biosensing of metabolite targets based on an enzyme electrode, including the current–time (i–t) curve and the i signal for quantification. Voltammetric biosensing of proteins or nucleic acids using an antibody-modified or nucleic acid-modified electrode through multistep sandwich sensing, one-step binding-induced folding sensing, including the current–potential (i–E) curve and i signal for target quantification. **c**) Ion-selective electrodes with three different structures, including recording of the potential (E) for target quantification. **d**) Impedimetric biosensing of bacteria based on antibody-modified electrode. **e**) Electrochemiluminescence biosensing of cells based on an aptamer-modified electrode through a sandwich-sensing format, including light intensity (IECL) at excited potential by a photomultiplier tube (PMT) or imaging using a camera for target quantification.

Therefore, electrochemical biosensors are very promising for the development of PoC diagnostic devices. The signal is generally activated by the transfer of electrons or ions onto a conductive transducer through a biorecognition

process. Signals can involve current (i), potential (E), impedance (Z), conductivity (σ), capacitance (C) and light (I)[45–47]. Thanks to their useful characteristics and versatility of use, these analytical instruments are used in the most varied fields: food quality monitoring (detection of glucose, biogenic amines, microorganisms, etc.), environmental monitoring (pesticides, gaseous analytes such as CO and CO_2, fertilizers etc.), in clinical diagnostics (blood glucose level, hormones, neurotransmitters etc.), and finally in forensic science (detection of doping and toxic substances, pathogens etc.) A theoretically preferred category of electrical biosensors for PoC diagnostics are impedimetric because they can directly detect biorecognition events by measuring the non-Faradaic resistance and capacitance properties of the sensing electrode. However, their practical implementation may suffer of unspecific binding with other compounds, leading to low sensitivity and selectivity. Furthermore, although impedimetric biosensors have been significantly improved during the COVID-19 pandemic[48], for example using molecular imprinting technology to fabricate virus-imprinted biosensors for the sensitive detection of whole viral particles[17], their sensing performances, so far, have only been demonstrated using artificial physiological samples instead of clinically relevant samples.

1.2.1. Amperometric and voltametric biosensors

Amperometric and voltammetric biosensors (**Figure 1.3b**) work with a classical three-electrode system, which contains a biosensor as a working electrode (WE) for target recognition, a counter electrode (CE) as a current source and a reference electrode (RE) for applying a stable potential. The current signals are generated by electrochemical reactions on the WE under a potential applied for target quantification.

Amperometric and voltametric biosensors are the most widespread, numerous and most successful electrochemical devices from a commercial point of view, as they are highly sensitive, reliable, economical and rapid. The two sensing techniques are based on the measurement of a current flowing through an electrochemical cell where a voltage is applied to the working electrode. The

voltage is set to produce a faradic process (oxidation or reduction) of the target molecule[49]. The current value is related to the analyte concentration according to the following mathematical equation (1):

in which:

$$i = nFAk_mC \ (1)$$

i = limiting current [A];

n = number of exchanged electrons

F = Faraday constant [C mol^{-1}]

A = working electrode area [cm^2]

km = mass transport coefficient [cm s^{-1}]

C = concentration of electroactive species [mol cm^{-3}]

The difference between the two techniques is their applied potential, which is constant for the amperometric and variable for the voltammetric sensing. Depending on how the potential is changed, the latter can be performed with various techniques, including cyclic voltammetry, differential pulse voltammetry, square wave voltammetry and anodic stripping voltammetry.

Amperometric biosensors are the most widespread sensors for the detection of metabolites (e.g. glucose), in fact, a target-specific enzyme (such as glucose oxidase (GOx)), is immobilized on the WE to catalyze the oxidation of the target at a constant potential[42], exploiting a redox mediator as the ferricyanide complexes. These devices are simple to fabricate, have high sensitivity and selectivity in target detection, making them suitable for PoC applications. Since the concentration of metabolites in non-blood fluids is lower than that in blood (for example, the concentration of glucose in sweat (10–200 μM) it is possible to functionalize the biosensor interface with nanomaterials, such as metal nanoparticles, carbon nanotubes and graphene, to facilitate electron transfer to increase sensitivity and decrease the detection limit[50]. An example, are Au-Pt bimetallic nanocatalysts which in combination with nanoporous hydrogels

enable GOx immobilization and glucose sensing with a sensitivity of 180 μA cm^{-2} $mmol^{-1}$ and a LoD of 0.01 mg dl^{-1} (0.56 μM)[51], **Figure 1.4**. Furthermore, in amperometric biosensors it is possible to implement nanomaterials with enzymatic emulating properties (i.e. artificial nanoenzymes) , avoiding the risk of natural enzymes denaturation. As an example, was developed highly conductive laser-induced graphene (LIG) array with a honeycomb-like 3D microstructure co-decorated with copper(I) oxide and gold nanocatalysts via simple and green electro-deposition and chemical reduction approaches, for a miniaturized electrochemical flexible non-enzymatic biosensor for blood glucose monitoring[52].

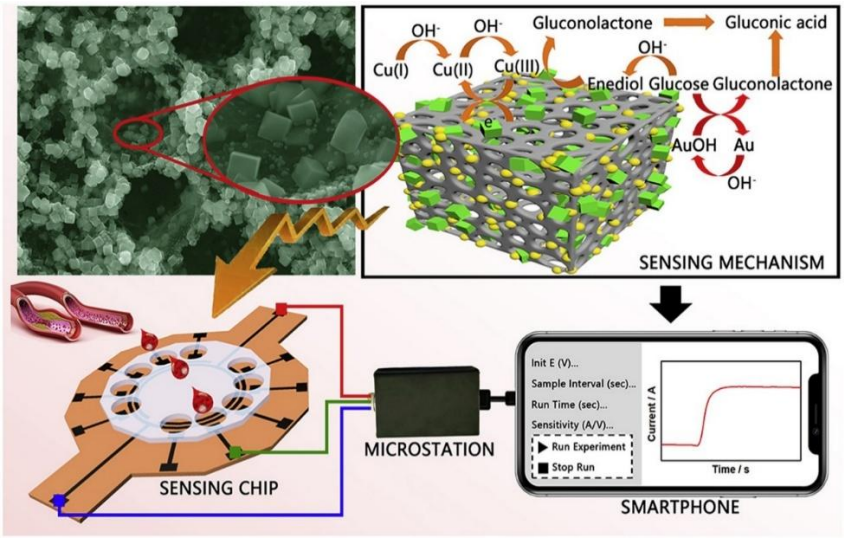

Figure 1.4. Miniaturized, electrochemical, flexible and non-enzymatic biosensor based on laser-induced graphene matrix, co-decorated with Cu_2O and Au nanoparticles for blood glucose monitoring[52].

The biorecognition of other molecular targets that act as crucial biomarkers of important human diseases, mainly consistent in proteins or nucleic acids, requires an additional electroactive labelling that can be operated by enzymes (e.g. alkaline phosphatase), nanomaterials (e.g. nanoparticles) and electroactive molecules (e.g. methylene blue). The voltammetric biosensors are typically used for such diagnostic applications, exploiting techniques such as cyclic voltammetry, differential pulse voltammetry, square wave voltammetry and anodic stripping voltammetry. These sensors can be

fabricated by immobilizing capture biomolecules as sensing elements (e.g. antibodies, antigens, aptamers and DNA probes) on the WE surface, enabling the detection of proteins or nucleic acids via a sandwich approach, represented in the voltammetric sensing scheme of **Figure 1.3b**. Due to the multiple steps required for the sensing interface preparation [42,43], automatic fluidic systems are typically integrated. This is the case of biosensors fabricated on screen-printed carbon electrodes, which are often coupled with a flow injection system to automatically detect multiple protein biomarkers[53,54]. Combining biosensors with automatic fluidic systems simplifies detection. However, device integration remains difficult due to the need for pumps and reservoirs. A simpler alternative to voltammetric sensors that exploit affinity biorecognition are one-step sensors. As an example, a binding-induced folding electrochemical biosensor can be fabricated by site-specific modification of a redox-labeled DNA probe on the WE[55]. Target detection is therefore based on moving the redox tags closer or further away from the electrode surface, resulting in an increase or decrease in the current signal for biosensing the target. Such binding-induced foldable electrochemical biosensors can achieve sample-responsive detection of nucleic acids or detection of some specific proteins using aptamer receptors. However, these devices suffer from low sensitivity which can be amplified using DNA hybridization strategies[56,57]; such as the CRISPR-Cas12a[58] technique.

1.2.2. Potentiometric biosensors

Potentiometric biosensors are based on the measurement of a delta potential between a working electrode and a reference electrode. This delta is a function of the activity of the detected species and, only for dilute solutions, their concentration[59]. The configuration of potentiometric biosensors is generally based on a two-electrode system consisting of a sensing electrode and a reference electrode. These allow direct detection of the target by measuring the potential signal related to the change in surface charge and therefore recognition of the target on the detection electrode. The most commonly used sensing electrodes are ion-selective electrodes (ISEs), made of thin films or

ion-selective membranes, **Figure 1.3c**. Examples of ISEs are glass membrane ISEs (pH electrode), solid membrane ISEs (e.g., crystalline membrane electrodes for F^-, Ag^+, Cl^- and S_2^-) or liquid membrane ISEs (e.g. ionophore-based electrodes for H^+, K^+, Na^+, NH_4^+ , Ca^{2+}) are commercially available. With the support of these ISEs it is possible to detect biological elements such as enzymes, nucleic acids and proteins by integrating the biological element of interest onto the ion-selective electrode to catalyse the reaction that forms the ions or by combining the target biorecognition event with an ionic reaction[60–62].

The equation that relates the measured potential difference and the analyte activity is the Nernst equation (2):

$$E_{cell} = E^0_{cell} - \left(\frac{RT}{nF}\right) lnQ \quad (2)$$

where:

E_{cell} is the observed cell potential at zero current [V];

E^0_{cell} is the standard cell potential [V];

R is the universal gas constant = 8.3143 [J K^{-1} mol^{-1}];

T is the absolute temperature [K];

n is the charge number of electrode reaction;

F is the Faraday constant = $9.6487 \cdot 10^4$ [C mol^{-1}];

Q is the ratio of ion activity at the anode to ion activity at the cathode;

The solid contact ion-selective electrodes, manufactured with solvent-based polymeric membranes, without the use of internal solutions which make them robust and easy to use, allow the analysis of proteins and nucleic acids through the detection of ions released by probes labeled with nanoparticles. An example is the use of a miniaturized solid contact Ag ion-selective electrode that allows the detection of DNA at the femtomolar level[63]. Moreover, there is the possibility of realizing solid-state ISE with conducting nanomaterials to

establish a solid contact under the ion-selective membranes and reference. These ISEs have been implemented in two commercial portable devices for PoC detection of electrolytes and blood gases (i-STAT from Abbott and BGA-102 from Wondfo Biotech), or, be integrated into wearable devices for ion detection in biofluids[64–66].

Lastly, an evolution of ISEs is represented by ion-sensitive field effect transistors (ISFETs). In these devices, the metal gate coated with an insulating layer of silicon nitride (Si_3N_4) and in direct contact with the analyte solution can be coupled with biological elements. In this context, the most widespread biological elements are enzymes, giving rise to the so-called enzymatic FETs[67] (ENFETs) and antibodies, which give immunosensitive FETs (immunoFETs)[68]. The advantages of ISFET are multiple: reduction of background noise, robustness, small size and fast response times.

1.2.3. Impedimetric biosensors

Impedimetric biosensors, reported in **Figure 1.3d**, rely on the electrochemical impedance spectroscopy (EIS) technique, which focuses on the analysis of the resistive and capacitive properties of detected molecules. The output signal is detected via a small-amplitude sinusoidal excitation signal[69,70] covering a wide range of alternating current (AC) frequencies, typically from 10 mHz to 100 kHz[71]. EIS applied voltage can be represented as follows (3):

$$Z = \frac{V(t)}{I(t)} = \frac{1}{Y} = \frac{V_0 sin(2\pi f t)}{I_0 \sin(2\pi f t + \varphi)} \quad (3)$$

where:

V(t) and I(t) are voltage-time and current-time functions, respectively

Y is the complex conductance or admittance

V_0 and I_0 are the maximum voltage [V] and current [A] signals

f is the frequency of the sine wave AC [s^{-1}]

t is the time [s]

φ is the phase shift between the voltage-time and current-time functions.

Usually, this technique obtains information by the three main parameters of the electrochemical cell: ohmic resistance of the solution, capacitance of the electrode/solution interface and rate constant of the electrochemical reaction. Equivalent circuit models are useful for the interpretation of impedance spectra (Nyquist or Bode plot), and constitute a valuable technique for the characterization, analysis and study of coatings, batteries, fuel cells and corrosion phenomena. Impedimetric biosensors are built to monitor a biological reaction on the surface of electrodes. When a biorecognition element is immobilized on the surface of the electrode the recognition process occurs and the parameters described previously will be influenced[14]. A variety of biomolecules can be used as sensing elements, such as enzymes, antibodies, oligonucleotides (oligos), whole cells and microorganisms, being immobilized on the sensing surface of the working electrodes. The most used biorecognition elements in impedimetric biosensors are antibodies and oligos. Zhao et al.[72] exploited electroactive indicators to characterize single-stranded (ss) and double-stranded (ds) DNA using impedance spectra. Results from the impedimetric spectra of a bare gold, dsDNA/Au, and ssDNA/Au electrode in a $Co(bpy)_3^{3+}$ solution showed that $Co(bpy)_3^{3+}$ concentrated on the DNA-modified electrodes a due to its interaction with the dsDNA or ssDNA anchored to the surface. Ferrocenium hexafluorophosphate ($FcPF_6$) has also been used as an electroactive indicator[73]. Single-stranded hepatitis B virus (HBV) DNA was immobilized on a gold electrode surface via a carboxylate ester as a link between the 3'-hydroxy end of the DNA and the self-assembled monolayer of the carboxyl group of the thioglycolic acid (TGA). By monitoring the impedance spectra, the Fc^+ interactions with ss- and dsDNA were highlighted which confirmed the immobilization and hybridization reaction with the surface. The mechanism of interaction between $FcPF_6$ and HBV ss- or ds-DNA immobilized on the electrode surface was also found to be electrostatic. Since 2007, a wide variety of so-called impedimetric immunosensors have been reported for the detection of different bacteria[71] and enzymes. For example, Cortina et al. [74] developed an impedimetric urea biosensor using the ether polymer Röhm

Pharma Eudragit S-100, which is a copolymer of methyl methacrylate and methacrylic acid that undergoes a degradation process at pH values above 7. In this enzymatic biosensor, hydrolysis of urea by urease, which causes an increase in pH, triggers polymer degradation and generates an increase in capacity, followed by EIS.

1.2.4. Electrochemiluminescence (ECL) biosensors

The ECL biosensors, schemed in **Figure 1.3e**, are based on the electrogenerated chemiluminescence, also called electrochemiluminescence (ECL). This technique consists in the light production by a luminophore species (an atom, a molecular entity or a nanoparticle) that is excited by an electrochemical reaction[75–78] and the subsequent electron-transferring at the electrode surface. The initial electrochemical input, indeed, trigs a cascade of chemical reactions that undergo highly exergonic homogeneous electron-transfer reactions to generate the electronically excited state of the luminophore. It relaxes to the ground state by emitting a photon. For instance, $[Ru(bpy_3]^{2+}$ is a model ECL luminophore that is largely used even nowadays and Tokel and Bard reported in the 1970s the first example of ECl derived from electrogenerated species of the $[Ru(bpy_3)]^{2+}$ complex[79]. The discovery of ECL emission in aqueous media with efficient coreactants such as tri-n-propylamine (TPrA)[80] has led to successfully commercialized bioassays for clinical diagnostics[81,82]. Similar to amperometric and voltammetric biosensors, electrochemiluminescence biosensors also work with a three-electrode system, in which the WE is modified with the recognition element to serve as a biosensing electrode. ECL is a technique with high sensitivity, good reproducibility, and high spatial and temporal control, making it a powerful analytical tool for biosensing a variety of disease molecules, including DNA, miRNA, proteins, and tumor cells[76,83,84]. An innovative ECL application has been designed for PCR-free detection of the dsDNA genome of hepatitis B virus (HBV)[47], Figure 5.

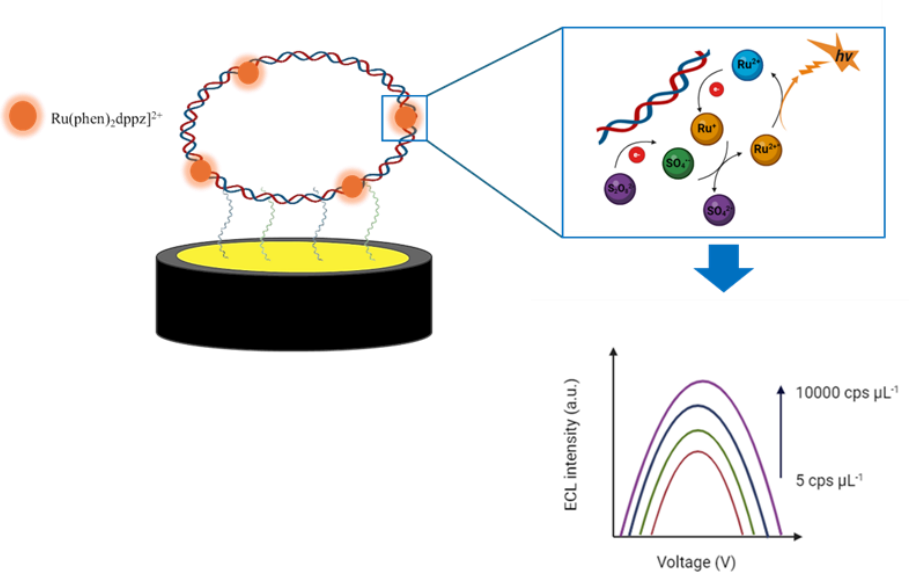

Figure 1.5. Scheme of ECL-PCR-free biosensing strategy[47]: Immobilization of specific probes on the surface of a gold electrode; recognition of ds-HBV by surface cooperative hybridization and intercalation of $[Ru(phen)_2dppz]^{2+}$. The intercalating complex in synergy with the coreactant, potassium persulfate ($K_2S_2O_8$), emits photons that allow the entire HBV genome to be detected.

The proposed approach relies on the synergy between the cooperative hybridization mechanism, performed by a sensing array of selective capture oligonucleotide probes, and the ECL detection, performed by $[Ru(phen)_2dppz]^{2+}$ complex, can detect the genetic target with LoD of 0.05 copies μL^{-1}, lower than the average LoD of PCR-based methods. Moreover, by changing the selectivity of the probes array, the strategy can be applied to the sensing of other pathogens, thus, opening towards the development of new diagnostic devices for massive bacterial and viral infectious diseases screening in a PoC format. In the work of Kerr et al. is described the construction of a ECL system with the help of a portable potentiostat and a smartphone camera to detect miRNA-21 through a molecular beacon detection strategy with magnetic bead-based electrochemiluminescence[85]. Lastly, some evidences report combinations of the ECL method with charge-coupled cameras and conventional microscopes for bioimaging applications where it is possible to simultaneously detect multiple biomarkers through spatial or potential resolution[86].

1.3. Optical Biosensors and detection techniques

Optical biosensors rely the analyte detection on its light absorption and emission properties[87]. The main components of an optical biosensor are: a light source, a detection probe as sensing element (DNA, peptide, antibody, aptamer, etc.), schemed in **Figure 1.6a**, a transducer tightly integrated with the probe and an optical detection system[88]. These biosensors can be divided into two categories: label-based and label-free[89]. A label-based detection uses a fluorescent or colorimetric label and detects the analyte by observing the fluorescence intensity or colour change[90]. This type of detection is very sensitive and can achieve very low LoDs[5,90]. Instead, in label-free detection, which is simpler and cheaper, a signal is generated directly from the interaction between the target molecule and the optical transducer. There are several spectroscopic transduction methods to detect optical signals resulting from these biosensors, for example: light absorption, diffuse reflectance, luminescence (fluorescence, phosphorescence, chemiluminescence, bioluminescence), fluorescence quenching, Raman, surface plasmon resonance (SPR), interferometry[91]. The surface plasmon resonance (SPR) optical biosensor is the most widely used one[92,93], which occurs on the surface of a metal (or other conducting materials) at the interface of two transparent media with different refractive indices. The most common applications for optical biosensors are in the biomedical field, for example in the diagnosis of infectious diseases[94]. There are also nanomaterial-based optical biosensors designed with exosomal biomarkers for early cancer diagnosis[95]. Fluorescent resonance energy transfer (FRET) biosensors are constantly used for the detection of bioactive molecules and for monitoring cellular behavior[96]. Thanks to technological progress, more performing optical transducers, as those based on photonic crystals, interferometry, etc., have been included to favour the implementation of sensors specificity and responsiveness.

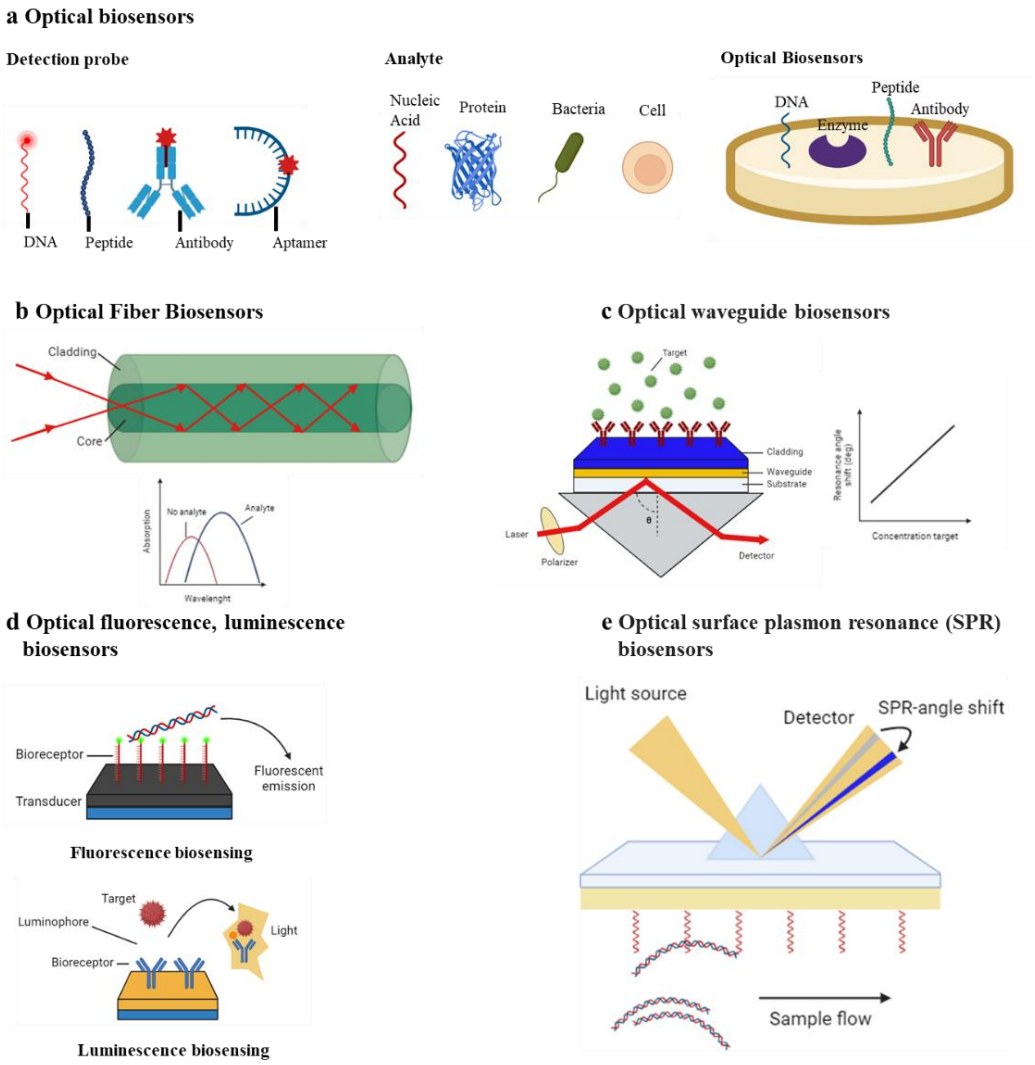

Figure 1.6. Optical biosensors. **a**) Detection probes and relative biochemical analytes. **b**) Optical fiber biosensors, based on total internal reflection light guiding mechanism and variations in absorption spectra of light depending on the analyte characteristics. **c**) A typical optical waveguide biosensor, based on a thin, optically transparent film with a refractive index that is higher than adjacent substrate and superstrate mediums. **d**) Optical fluorescence and luminescence biosensors, based on the measurement or imaging of the light emitted by a different luminescence reactions. **e**) Surface plasmon resonance (SPR) biosensor, based on the variation of the refractive index once the biomolecules have bonded to the surface which generates the SPR angle.

1.3.1. Optical fiber biosensors

Optical fiber-based biosensors, described in **Figure 1.6b**, are analytical devices consisting of a fiber core, a cladding, a metal coating and a sensitive layer for the detection of analytes. These optical biosensors can be classified into two different categories: intrinsic sensors, where the interaction with the analyte takes place within an element of the optical fibre; and extrinsic sensors, in which optical fiber is used to couple light, usually to and from the region where the light beam is affected by the measurand. Optical fiber biosensors use the principle of total internal reflection (TIR) in which the light traveling through the core of the fiber is surrounded by a cladding. A part of the coating region is replaced with the metal coating and the detection probes. Probes are immobilized on the fiber core to react with the analyte. The usual purpose is to produce a signal that is proportional to the analyte concentration towards which the probe is sensitive. Numerous recent works reported optical fiber biosensors applications. Molecular recognition processes are very important in the study of biological phenomena as well as in the development of these biosensors. **Figure 1.7** shows a portable and low-cost borosilicate glass fiber optic biosensor for the detection of *Escherichia coli* (E. coli) using the variation of the refractive index of the glass fiber[97]. E. coli can also be recognized with promising materials such as the biofunctionalized polydiacetylene lipids p-10,12-pentacosadiino-1-N-(3,6,9-trioxaundecylanide)-α-D-mannopyranoside (MPDA), synthesized from 10,12-pentacasadiinoic acid (PDA)[98].

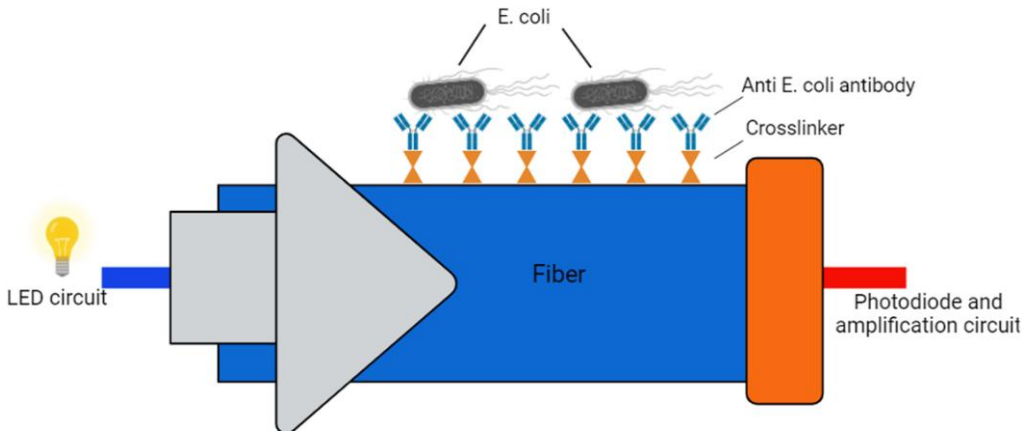

Figure 1.7. Schematic representation of the glass optical fiber biosensor with antibodies immobilized on the surface. As light travels through the glass fiber, the evanescent field interacts with the bacteria on the surface of the fiber[97].

The mixed (MPDA/PDA) monolayer resulted in a colour change of the film that allowed to quantify E. coli by UV-VIS absorption spectroscopy. Lastly, another optical fiber biosensor has been reported for the detection of the CD44 protein[99], whose main function is the recognition of hyaluronic acid in particular areas such as embryonic connective tissues and the outline of invasive cancerous lesions. The biosensor is based on a spherical optical fiber tip that was functionalized with anti-CD44 antibodies detecting the target of interest with an achieved LoD of 17 pM.

1.3.2. Optical waveguide biosensing

Optical waveguide biosensors due to their ultra-small size, high sensitivity, detection and label-free are perfectly suitable for biosensing. Compared with traditional sensors that rely on electrical signals for sensing, the optical waveguide sensor has lighter mass, smaller volume and lower power consumption[100–102]. The working principle of optical waveguides can be explained by attenuated total reflection (ATR). When light propagates in the dense medium of the waveguide, a leakage field is generated on the surface of the waveguide. They consist of a sensing layer, cladding and waveguide layers placed on a substrate as shown in **Figure 1.6c**. The most used biosensor in biochemical detection is the Mach-Zehnder interferometer[103] that, thanks to the dual-arm structure, can achieve real-time detection and reduce the error caused by multiple measurements of a single arm. Recently, the research direction is aimed at improving the optical waveguide structure especially towards the composite structure. For example, Liu and his colleagues recently introduced a highly sensitive biosensor based on a silicon nitride slot waveguide with a slot waveguide sensing arm while a slot waveguide reference arm strip[84].

1.3.3. Fluorescence and luminescence biosensing

In this class of biosensors, the light coming from a fluorescence/luminescence process is detected using appropriate photodiodes or photomultipliers. In **Figure 1.6d**, the typical structure of a fluorescent and luminescent biosensor is shown. Fluorescent biosensors have made great progress in recent years and are widely used in many scientific fields such as biology, chemistry, medicine and others[104–107]. The operating principle is based on the intensity of the fluorescence which is recorded as a readout signal for the analytes. They have many advantages including rapid response, multiple assays, high sensitivity and selectivity[108–110].

Fluorescence detection is very sensitive, so that several parameters need to be considered when building the biosensor. A brighter fluorescent tag and signal amplification technology are usually applied. Researchers explored new signal amplification strategies that could significantly improve the fluorescence signal and sensitivity[111]. Among these, cyclic signal amplification (CSA) technology is one of the most useful due to its low-cost and versatile design principles. CSA technology utilized the hybridization of nucleic acids or enzymes for nucleic acids to release the analyte, which will be recycled for further increase the fluorescence outputs of the biosensors. Therefore, after the CSA, the fluorescence signal could be amplified many folds to achieve highly sensitive and low limit of detection for biomolecules. . Therefore, the fluorescence signal can be amplified many times to achieve a highly sensitive and low detection limit for biomolecules. The most commonly used CSA methods include rolling circle amplification (RCA), and enzyme-assisted amplification (EAA)[112,113]. The first method is a signal amplification technology commonly used to construct fluorescent biosensors[114]. It is a relatively simple and powerful technique for isothermal DNA replication. RCA contains a circular DNA and a linear complementary primer[115], as shown in **Figure 1.8**. Circular DNA is used as a template, and the primer is hybridized with circular DNA, which then forms a single strand of DNA containing a large number of repeated sequences by polymerization, which can trigger the increase of fluorescence signal through amplification.

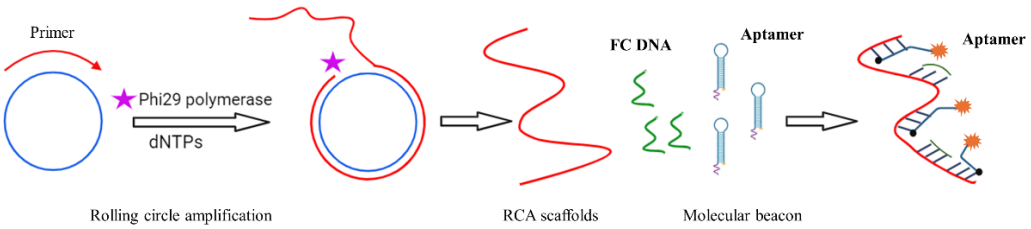

Figure 1.8. Schematic illustration of circular DNA as a template for RCA[115].

Lastly, the enzyme-assisted amplification (EAA) refers to the CSA reaction assisted by different enzymes (such as exonuclease, endonuclease and ligase) for nucleic acids that operate different signal amplification patterns. The released analyte can, then, trig another round of probes activation through the amplification process. Therefore, by EAA sensitivity and selectivity of fluorescent biosensors can be significantly improved [116,117]. Zhou et al. proposed a method for sensitive detection of miRNA based on EAA[118] that achieved a LoD of 1 pM and a good suitability for cancer cells applications.

Other luminescent biosensors exploit the sensing on the measurement of light produced by bio-chemiluminescence (BL, CL), thermochemiluminescence (TCL) or electrochemiluminescence (ECL) reactions. Their main advantage is the improved sensitivity due to the high detectability of photons released by these chemical reactions. For example, it is known that the light emitted by chemiluminescence arises from an exergonic chemical reaction that produces an intermediate in its singlet excited state, which undergoes radiative decay. Chemiluminescent assays generally use direct labeling with isoluminol and acridinium esters, the sensitivity of which can be up to the nanomolar level and the signal-to-noise ratio is very high. In particular, acridinium salts show a higher quantum yield in aqueous media than luminol derivatives[119]. However, sensors based on bioluminescence have the peculiar characteristic of providing much higher quantum yields, compared to classical chemiluminescence methods, due to the light emission resulting from a singlet excited state enzyme-product complex. Bioluminescence mainly rely on enzymes like luciferase that in presence of ATP gives luminescence allowing ultrasensitive detection down to the part per million (ppm) level in several bioanalytical applications[120,121].

1.3.4. Surface plasmon resonance (SPR) biosensing

Surface plasmon resonance (SPR) biosensors, **Figure 1.6e**, are probably the most studied and used optical biosensors due to their advantages such as (i) label-free detection, (ii) dynamic measurement of binding–unbinding kinetics to observe the reaction mechanism occurring over the sensing surface, and (iii) high sensitivity. SPR is a technology that detects alterations in the localized refractive index (resonant angle) to evaluate the bonding of molecules on a metal surface. Variations in the refractive index generate surface plasmons (large groups of electrons in an oscillating state) which are proportional to the mass of the sample (for example antibodies) immobilized on the biosensor[122,123]. The unitary SPR signal is defined as the resonance unit (RU), and is equivalent to a critical angle shift of 10^{-4} degrees which corresponds to approximately 1 pg (picogram)/mm^2 of analyte-bound surface area[45]. At the beginning of the experiment, in the absence of the target analytes, the initial RU value coincides with the resonance angle. The variation of the refractive index within a layer of thickness h can be calculated as (4):

$$\Delta n_d = (\frac{dn}{dc})_{vol} \frac{\Delta \Gamma}{h} \quad (4)$$

where:

$(\frac{dn}{dc})_{vol}$ is the increase of refractive index n with the volume concentration of analyte c; ΔΓ is the concentration of the bound target on the surface. The development of SPR-based sensors was introduced by Kretschmann and Reather in 1968, who introduced the conventional prism-based configuration[124]. Since then, SPR-based research has grown exponentially, with the development of different configurations for creating new sensors towards PoC applications. To develop these devices, the sensing layer is prepared on a thin metal-coated glass substrate (~50 nm) and the analyte is flowed into a microfluidic channel close to the sensing layer to enable biorecognition. Bai et al.[125] presented an SPR-based biosensor for the detection of avian influenza virus (AIV) H5N1 using a selected aptamer as the recognition element, described in **Figure 1.9**.

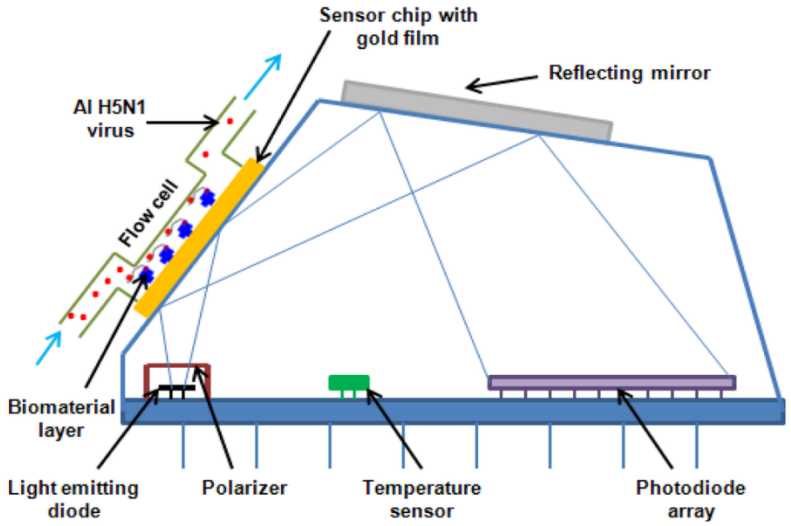

Figure 1.9. Internal configuration of the SPR-based aptasensor for the AIV detection[125].

The sensing device was fabricated by immobilizing the biotinylated aptamer on a streptavidin-coated gold surface. The sensor had an analysis time of 1.5 hours and showed applicability in poultry swab samples. Preliminary studies have shown highly sensitive virus detection in the range of 0.5–10 µg/mL along with a high precision.

The detection of AIV using a cooperative DNA hybridization mechanism was proposed by Kim et al.[126] by a study based on quantitative monitoring of thiolated oligonucleotides during the hybridization process.

Palau et al.[127], instead, demonstrated a direct analysis of RNA-RNA binding at the 3' end of hepatitis C virus (HCV), by which biological interactions were analyzed through complex mutation and reverse genetics experiments, involving 5BSL3.2, i.e. a stem loop located in the HCV NS5B coding region.

1.4. Medical biosensors for Point-of-Care testing

As described before, one of the most important applications of biosensors are the point of care testing (PoCT), which consist in diagnostic or prognostic test that allows rapid results to be obtained for the diagnosis of or monitoring of diseases. This type of test must be performed quickly, easily, without the aid of

expensive instrumentation and specialized staff as a laboratory is not necessary[128,129]. Currently, with its ability to generate rapid results, the research focused on PoCT is shifting towards massive screening and early diagnosis of diseases in order to effectively manage treatments, thus, reducing the mortality rate.

The most established PoC platforms are the Lab-on-a-chip (LoC) devices, shown in **Figure 1.10**. These are miniaturized devices able to provide various analyses such as biochemical operations, chemical synthesis, DNA sequencing onto a single chip which otherwise would have been performed in laboratory taking sufficient amount of time. Due to the miniaturization of these biochemical operations, better diagnostic speed, cost efficiency, ergonomy, sensitivity and so on can be achieved. There are different materials by which it is possible to fabricate lab-on-chip biosensors including: glass, silicon, thermoplastic polymers, based on paper and polydimethylsiloxane (PDMS). The last two are the most widely used due to their low cost and easy manufacturing[130].

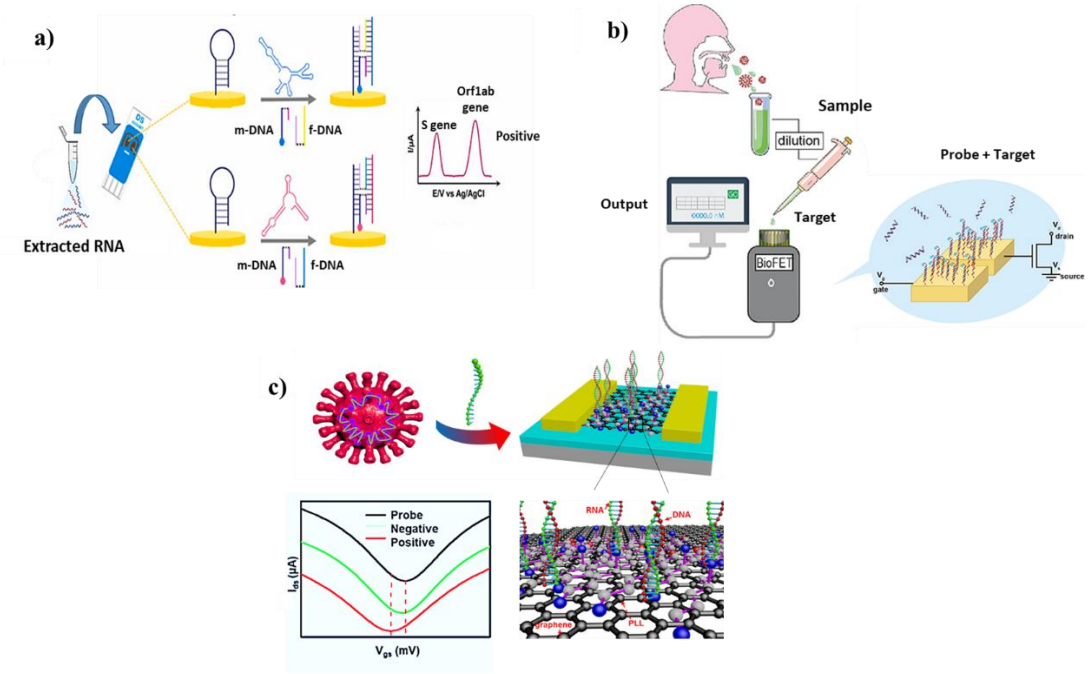

Figure 1.10.Schematic illustration of LoC devices. a) Electrochemical sensor based on four-way junction (4-WJ) hybridization for the detection of SARS-CoV-2b) EDL-

gated BioFETs to rapidly detect SARS-CoV-2 viral RNA in saliva and c) GFET biosensor for SARS-CoV-2 RNA detection[48].

LoCs are suitable for several applications mostly concerning molecular diagnostics, in which these devices allows a faster nucleic acids detection based on microscale thermal shifting at high speeds[131]. Some evidences in literature report an application of LoCs in non-small cell lung cancer diagnosis[132]. This device was based on an integrated volumetric bar graph chip made of nanoporous glass (NPG V-Chip) in which a lung cancer biomarker, carcinoembryonic antigen (CEA), was conjugated to the surface of the NPG and quantified. The reaction was aided by adding hydrogen peroxide to produce oxygen gas. This then pushed the red ink through the serpentine channels to form a bar graph, indicating that the further the red ink moves, the higher the concentration of CEA in the sample.

A special type of PoC are labeled PoCs, in which the target itself is not the transducer. When the target is present starts a series of events that lead to a detectable signal. One of the most consolidated labelled PoC system is based on the enzyme-linked immunosorbent assay (ELISA)[133]. The technology relies on capture antibodies bounded to the sensing surface and able to recognize a specific antigen target. Once interacted, a labelled secondary antibody (linked to nanoparticles or enzymes) binds to the captured antigen forming a molecular sandwich. Other evidences report labelled PoC applications in molecular diagnostics, using DNA probes as sensing elements. One of these concern the sensing of human papillomavirus (HPV)[134], focused on the genetic plasmids of HPV types 6, 11, 16 and 18. Targets were first amplified and labelled by fluorescent primers in PCR and, then, flowed into a microfluidic system exposing oligonucleotide capture probes selective for each HPV strains. After hybridization with capture probes, the amplified and labelled targets were revealed by their fluorescence using an optical reader.
Labelled PoC systems, however, have the main disadvantages of time required to label the sample and need to operate in specific laboratories. These limitations have been overcome by label-free techniques.

Instead, label-free PoC devices don't require a target labelling and consequently eliminates all sample processing steps and lab constraining[135]. Moreover, many of these methods involve nanomaterials for detection[136]. An example of label-free PoC systems concerned the detection of tobramycin, with a LoD of 3.4 μM, using an SPR-based aptasensor. This method measured several biomarkers in blood serum and worked in both direct and sandwich tests[137].
However, a main drawback of label-free PoCs is that samples often need to be amplified before use, and without this, a lower sensitivity may be observed.

Lastly, it is important to mention the PCR-free PoCs and their genomic detection strategies which will be the central topic of the following thesis. The PCR-free approach for the DNA/RNA detection introduced a new frontier of molecular diagnostics where the viral genome is directly revealed without its amplification. To accomplish this type of alternative molecular analysis, however, is very important to guarantee the best compromise between a high-resolution analysis, which could be able to provide the sensitive and accurate revelation of a few copies of a genetic target, and an integrable and miniaturizable dedicated measurement setup that is consistent with the idea of a PoC application[48].

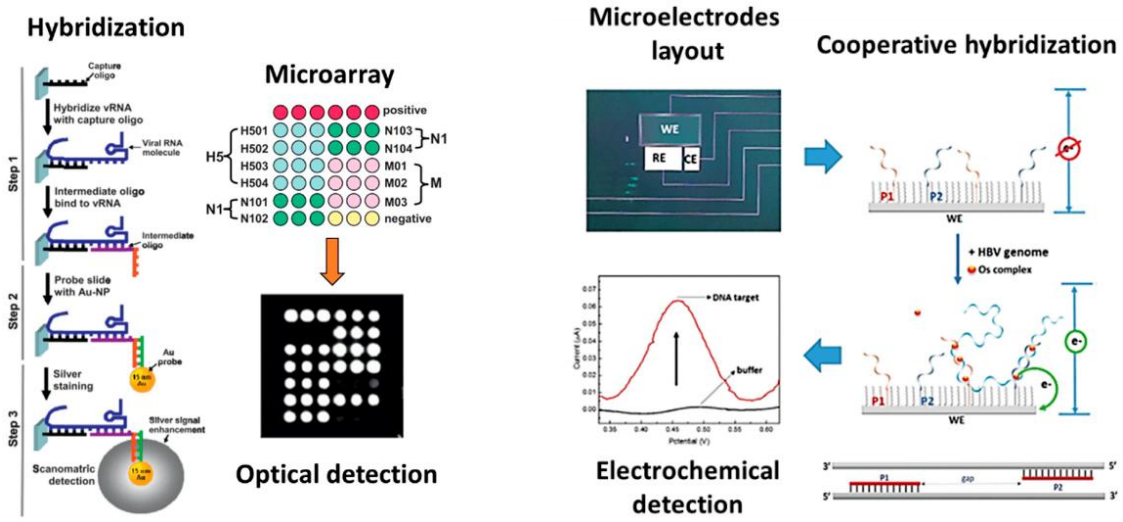

Figure 1.11. PCR-free genomic detection strategies in genetic PoC systems[138].

So, alternative PCR-free genomic detection strategies, reported in **Figure 1.11**, have been proposed in genetic PoC[138].Zhao et al., for example, developed a PCR-free system for the rapid detection of avian influenza virus H5N1[139], **Figure 1.11.a**. The system was a modified microarray platform with immobilized oligos used to directly and specifically hybridize the H5N1 RNA and, then, allow another poly-A-tailed intermediate oligos to form a sandwich complex with the target. Furthemore, in 2017, Sciuto et al. proposed a technology for portable and rapid electrochemical detection of HBV without NA amplification[140], **Figure 1.11b**. The device consisted of a silicon miniaturized chip containing three microelectrodes and the chemical strategy employed was based on the hybridization between the target viral genome and two specific oligonucleotide probes grafted on top of the WE of the chip. Thus, from these simple examples it is clear that these new biosensors, most of which have not yet been thoroughly studied and commercialized, involve a variety of detection strategies suitable for providing rapid and accurate analysis of the virus towards its early and massive screening and active surveillance for the containment of viral infections.

CHAPTER 2

PCR-free Biosensing method for the detection of infectious pathogens nucleic acids in a PoC

2. State-of-the-art on PCR-free biosensor for infectious diseases

The detection of nucleic acids is nowadays of extreme importance in many medical fields for early and accurate diagnosis, personalized therapy, and preventive screening. In this context, DNA/RNA identification and quantification through molecular methods provides relevant clinical advantages with respect to the traditional laboratory methods, such as bacterial cultures or antibody detection, being much faster (hours vs days for bacterial cultures), specific (allowing the detection of genotypes), sensitive (few copies of pathogens in a sample) and accurate (able to detect different microorganisms through the specific molecular biomarkers). However, molecular methods typically need an amplification step achieved through the well-known PCR reaction that is intrinsically quite laborious because it involves a multi-step and expensive process (about 15$ to 80$ per sample), thus, limiting its utilization to specialized laboratories[141]. Therefore, although current PCR-based methods are well-established and consolidated, they are not suitable to be used by unqualified personnel, in decentralized applications and at competitive costs, which represents a strong limitation for molecular analysis massive use in public health.

Actually, the recent period of coronavirus disease 2019 (COVID-19) pandemic brought a growing need of fast and reliable methods for pathogen microorganisms detection[142–144] combining the high sensitivity and accuracy level of PCR-based molecular analysis with the speed and low costs of rapid immunological tests, pointing to achieve a significant breakthrough in diagnostics and genetic detection. This led to the introduction of the Genetic Point-of-Care technologies[11,145] (G-PoC) that brought important advantages concerning the simplified and time-costs saving analytical protocols (performable also by untrained personnel), the low power supply and the miniaturizable and integrable system architecture that makes the analysis suitable for low-resource settings applications[146,147]. G-PoC are mostly based on the PCR-free approach that excludes any pre-amplification of the genetic

target by PCR, thus, simplifying the sample preparation and the required instrumentation. However, this approach is extremely challenging since the direct detection of the target must be performed at a very low concentration of template. This is the case of the infectious diseases in which the concentration of bacterial or viral genome is restricted to low copy number per microliters of biological fluids (saliva, blood, etc.). Therefore, only few examples of PCR-free methods have been reported in the literature so far and, consequently, a limited number of devices has been proposed[85]. Furthermore, most of them used indirect strategies for pathogens detection that achieved high LoDs and were constrained to complex lab instrumentations[148 140 149]. Additionally, all the reported methods needed a sample pre-treatment or labelling step, thus, increasing the level of complexity[150].

A fundamental prerequisite to achieve an effective PCR-free detection of the pathogens NA is the design of an innovative sensing strategy for the molecular detection of genetic/genomic targets and its combination with a highly efficient transduction method, as schemed in **Figure 2.1**. The strategy should rely on the use of two or more oligonucleotides that bind the same NA target sequence by a mechanism called cooperative hybridization[151]. The oligonucleotides used as sensing elements or probes are typically immobilized via different grafting and anchoring approaches onto silicon-metal surfaces to form the sensing array. Immobilization of the probes on the surface is the crucial step for this DNA detection strategy. Various methods, such as covalent binding, adsorption, and trapping, have been employed to stabilize DNA on various surfaces[152]. Once immobilized, the probes can capture the molecular target via cooperative hybridization and cause the recognition event that is properly revealed by electrochemical, optical or electrical techniques. Among these, the electrochemical detection is widely used since it provides low LoDs, the possibility to consistently downscale the entire sensing system, cost-effectiveness, easy-to-use procedures and rapid responses[153,154]. In parallel, in order to increase the yield and stability of probes-target interaction via cooperative hybridization is, also, important to achieve the right dimension and degree of conservation of the genetic region inside the target that is recognized

by the probes. Moreover, it is necessary to choose the best composition of probes, in terms of guanine-cytosine content percentage (GC%), annealing temperature and chemical derivatization to improve the capture performances in the PCR-free sensing.

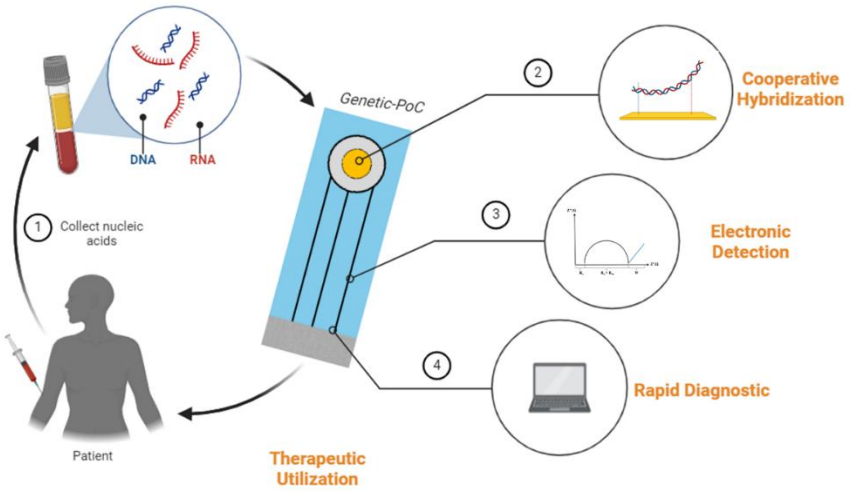

Figure 2.1 PCR-free approach for nucleic acid detection through the mechanism of cooperative hybridization.

Consistently, in this section is described the development of a PCR-free sensing strategy for the molecular detection of three pathogen microorganisms of relevant importance for human health: *L. infantum* (LI) protozoan; the *P. aeruginosa* (PA) bacterium; SARS-CoV-2 (SC) virus. The whole genome or not amplified genetic materials of these pathogens have been chosen as used-case target for the PCR-free detection via cooperative hybridization. These targets were: the circular kDNA of LI; the dsDNA genome of PA; the ssRNA genome of SC. In a first step, three combinations of oligonucleotide probes, for each target, have been defined by an approach that started with a study of the most significative genes belonging to the genomes of the above reported targets. The probes have been, then, customized with specific 5' thiol-derivatizations, needed by the subsequent functionalization procedures. Lastly it has been developed the chemical protocol for the functionalization of gold (Au) working electrodes surface of selected use cases with the three types of capture probes specific and genetic material. The effectiveness of probes anchoring, genetic material hybridization and coverage of the electrodes

surface has been, also, characterized by contact angle (CA) measurements, electrochemical impedance spectroscopy (EIS), cyclic voltammetry (CV) and X-ray photoelectron spectroscopy (XPS).

2.1. Development DNA strategy for PCR-free molecular detection of *Leishmania infantum*

Leishmania, a protozoan parasite, causes leishmaniasis or kalaazar disease[155]. Leishmaniasis is one of the chief parasitic diseases that causes epidemic and is transmitted through infected blood transfusions, sand fly bites and the reuse of infected needles[156]. Visceral leishmaniasis (VL) as one of the most severe clinical manifestations of leishmaniasis, is caused by the species of LI parasite that can cause a high rate of mortality. In VL, LI parasite migrates to the visceral organs of bone marrow, spleen and liver[157]. As the main host of LI, dogs are considered as the primary reservoirs for human Leishmania infections[158]. Clinical presentation in this host is characterized by renal alterations, prolonged fever, splenomegaly, hepatomegaly, ocular lesions, skin disease, and respiratory system and cardiovascular disorders. It is estimated that there are >400000 new cases of VL each year with > 40000 deaths[159]. Hence, early and accurate diagnosis and proper management of L. infantum infection is highly important. Generally, leishmaniasis is confirmed by (i) amastigotes presence by microscopic recognition; (ii) detection of the parasite genomic DNA, LI consists in a small minicircular DNA, between 0.8 and 2 Kbp, in tissue samples; (iii) enzyme-linked immunosorbent assay (ELISA); (iv) indirect immunofluorescence assay test (IFAT); and (v) detection of the parasite reproductive form in the spleen aspirates or bone marrow[160,161]. Although these methods can be considered for VL diagnosis and can bring reliable results, specific limitations have been found for these methods[161]. Furthermore, molecular biology techniques, such as spot, dot, and squash blots, as well as ELISA, lack of rapidity, sensitivity and specificity for the isolates[162–164]. Although the results obtained from PCR, RFLP, RT-PCR and conventional PCR are quantitative and reliable, they require a well-equipped

laboratory and technical complexity[165,166]. Hence, there is a growing need to develop rapid, sensitive, selective, cheap and reliable methods for the *Leishmania* identification.

Several detection methods have been reported for the detection of LI mostly based on electrochemical detection, which allows to obtain useful information on the electrical double layer formation and biointerface performance. An example was from Nanani-Vanani et al[167], that proposed an electrochemical biosensor for the detection of LI based on the immobilization of a DNA probe sequence on a gold surface coated by a layer of polyaniline matrix with a terminal thiol group (PANIAuNp). The probe-target DNA binding was assayed by electrochemical impedance spectroscopy and cyclic voltammetry. These types of DNA-based electrochemical sensors have gained considerable popularity due to their wide implementation for the detection of mutated genes, target DNA sequences, and various diseases[168].

In the present section, the development of a PCR-free sensing method for the molecular detection and quantification of LI is reported. The method brings an improvement of the conventional NA detection in terms of time-/cost- saving, since exclude the PCR amplification step keeping a high level of sensitivity and selectivity, and suitability for PoC applications, due to the miniaturizability of the analytical system architecture. The developed sensing method relies on a gold surface functionalization based on the grafting of specific thiol-modified oligonucleotides probes used for the selective recognition of LI via a cooperative hybridization mechanism.

2.1.1. Experimental

The capture probes selection and design for the recognition of the minicircle kinetoplast (k)DNA of LI have been performed by a first investigation of literature. The work of Mary et al. in 2004[169] reported the performances of two highly selective primers used for the Real-Time (q)PCR amplification of the kDNA. These primers were specifically designed to recognize an inner region

of the kDNA, whose sequence is highlighted in the map and detail reported in **Figure 2.2a** and **2.2b**. The two oligonucleotides, for convenience, have been named “LI_P1” and “LI_P2” and have been identified as optimal solution in terms of recognition sequence size, 140 bp, and annealing temperature, around 60 °C. In order to anchor the oligonucleotide probes on the surfaces to be treated, these have been 5’-derivatized with thiol chemical group (-SH) for the creation of the interfaces used in the pathogens biosensing application. A chain of 6 carbon atoms (C6) has been also added at 5’ end of each sequence to act as spacer for the right orientation of probes once anchored to the surface, **Table 2.1.** The thiol-modified probes LI_P1/2-T, both purchased from MetaBion (Planegg, Germany), were grafted on top of the gold (Au) surface and the subsequent formation of a self-assembled monolayer (SAM). The couple of anchored probes were, then, exposed in the right orientation for the synergic interaction with the molecular target in the cooperative hybridization, enhancing both yield and stability of the target capture.

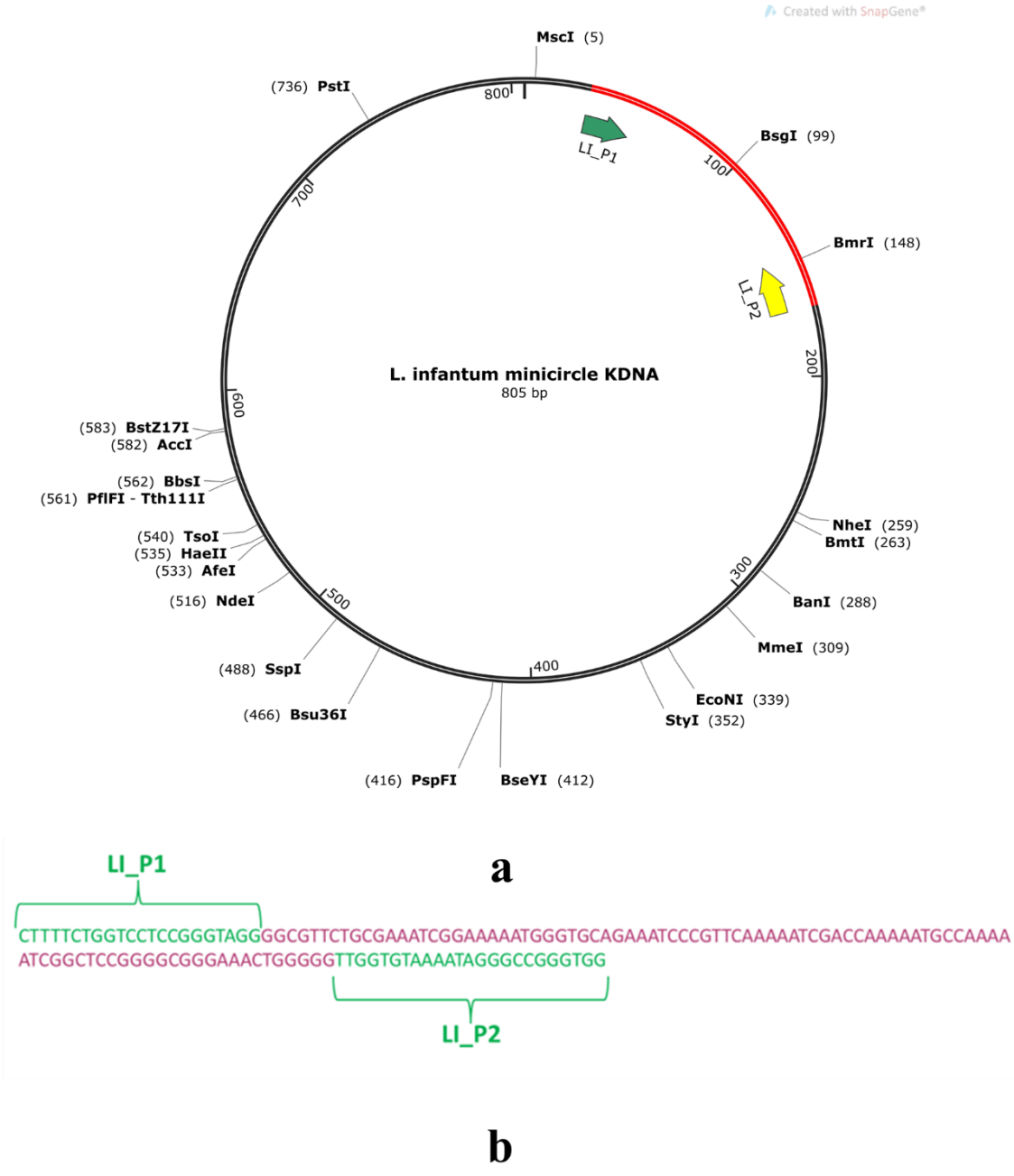

Figure 2.2 a) Map of the 800 bp kDNA of *L. infantum*. b) LI_P1 and LI_P2 recognition sequence.

Table 2.1. Use case thiol-modified probes

Probe	Sequence 5'-3'
LI_P1-T	HS-C6-CTTTTCTGGTCCTCCGGGTAGG
LI_P2-T	HS-C6-CCACCCGGCCCTATTTTACACCAA

For the target preparation, extracted and purified LI kDNA samples at a concentration of 10^8 cps/µL were provided by the group of Prof. Varani from University of Bologna and diluted in DNAse and RNAse-free water to the working concentration, from 10^6 to 10^{-1} cps/µL.

The chemical functionalization of the gold surface was fully characterized by contact angle (CA) and surface-free energy (SFE) analysis using an gold-sputtered silicon sample as substrate. We performed the surface characterization analysis using four replicates of each functionalization step.

The substrate used, instead, for the sensing tests was a commercial gold electrode from CH Instruments. We performed the electrochemical analysis using five replicates for each functionalization step, five replicates for each tested kDNA concentration and three of zero-dose measurement (blank), which is considered a baseline measurement. In this case, the correct functioning of the biosensor and its ability to recognize LI kDNA was evaluated electrochemically with cyclovoltammetry (CV) and electrochemical impedance spectroscopy (EIS) measurements, performed in collaboration with the group of Prof. Prodi and Prof. Valenti of the University of Bologna.

2.1.1.1. Gold-sputtered silicon substrate functionalization

The gold-sputtered silicon substrate of 0.55 cm x 1 cm was functionalized with LI probes (Table 2.1) and kDNA target according to the chemical protocol schemed in **Figure 2.3.** First, it was carried out a step of surface cleaning that has been deeply optimized in order to find the best compromise between dust and unspecific organic dendrites removal and surface gold layer preservation. The gold substrate was placed inside a Teflon container and, initially, 10-fold rinsed with distilled water. Subsequently, a basic piranha solution (H_2O_2 : NH_3 : H_2O = 1:1:4) was spotted at 70°C for 2 minutes to completely clean the surface. At the end of the process, the substrate was rinsed abundantly with ultrapure water and fluxed with nitrogen. Subsequently, the substrate was incubated with a 1 µM solution of thiol-modified probes, suspended in PBS 0.01 mM at pH = 6.0, at 25°C for 4 h with 40 rpm of stirring.

This condition was required to allow the probes to be efficiently dispersed and favour the thiol-gold complex formation in a SAM configuration. The SAM enabled the probes to be exposed in the right orientation for the sensing interaction with the genetic target. Then, a washing step with PBS removed the unbound probes from the surface. For the not amplified genetic target hybridization, kDNA was directly used at a final concentration of 10^7 copies/µL in PBS at pH 5.5, prepared by diluting the 10^{10} copies/µL stock solution. The final gold interface functionalized with LI_1/LI_2 probes were dipped in kDNA solution at 50 °C for 3.5 h. Then, the unbound kDNA was washed away from surface by PBS buffer.

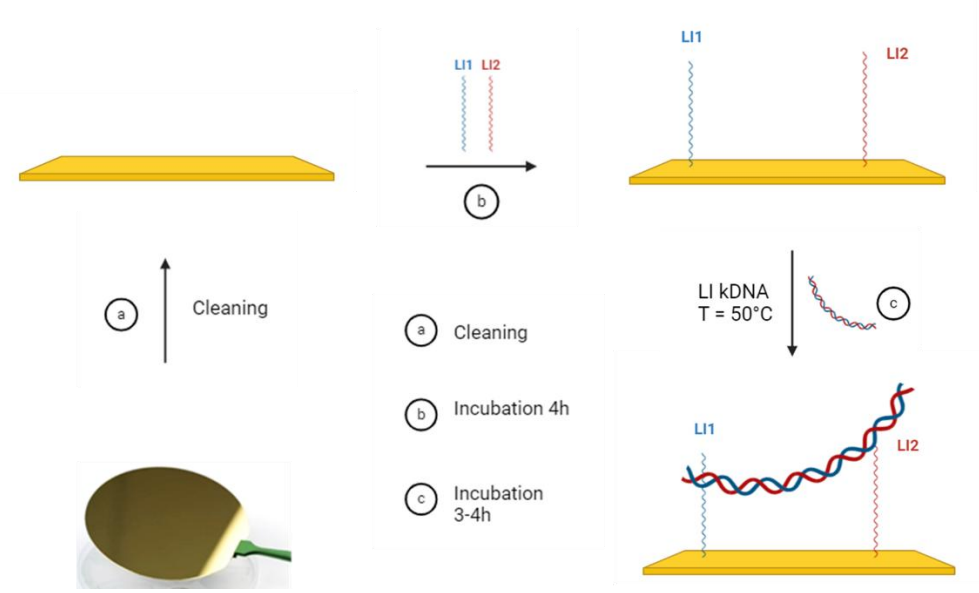

Figure 2.3. Gold substrate preparation, a) Surface cleaning with basic piranha solution; b) Immobilization of specific probes LI_1 and LI_2 and c) recognition of LI kDNA by surface cooperative hybridization.

2.1.1.2. Commercial gold electrode functionalization

A CHI101 gold electrode was functionalized as reported in **Figure 2.4**. First, the electrode surface has been cleaned using the following treatment: polishing of the Au surface with alumina slurry and washing by sonication in 50% ethanol for 5 min; cyclic voltammetry in 0.5 M H_2SO_4, in the range of −1 V to 1 V for 10 cycles; drying with Ar gas. Next, LI_P1-T and LI_P2-T thiol 5'-terminated probes were dissolved in PBS 0.01 M (pH 6.0) buffer at a

concentration of 1 μM and immobilized on the surface according to the following procedure: electrodes were kept at "Room Temperature (RT)" for 4 h immersed in the solution containing the thiol-terminated probes. Probes target the conserved region of the kDNA minicircle molecules, a part of Leishmania spp. entire genomic DNA (gDNA)[170]. The distance between the two internal ends is 94 base pairs (bp) when aligned against *L. infantum* kDNA sequence (Accession number Z35273.1). The SAM enabled the probes to be exposed in the right orientation for the sensing interaction with the genetic target. Afterwards, they were gently washed with PBS 0.01 M (pH 6.0) followed by an overnight blocking procedure with 10 μM of $C_6H_{14}OS$ dissolved in PBS 0.01 M (pH 6.0) to stabilize the assembled layer of LI_1 and LI_2 specific probes. For the not amplified genetic target hybridization, kDNA was used at a different concentration (1, 10, 10^2 and 10^4 copies/μL) in PBS at pH 5.5, prepared by diluting the 10^{10} copies/μL stock solution. The final gold interface functionalized with LI_1/LI_2 probes were dipped in kDNA solution at 50 °C for 3.5 h. Then, the unbound kDNA was washed away from surface by PBS buffer.

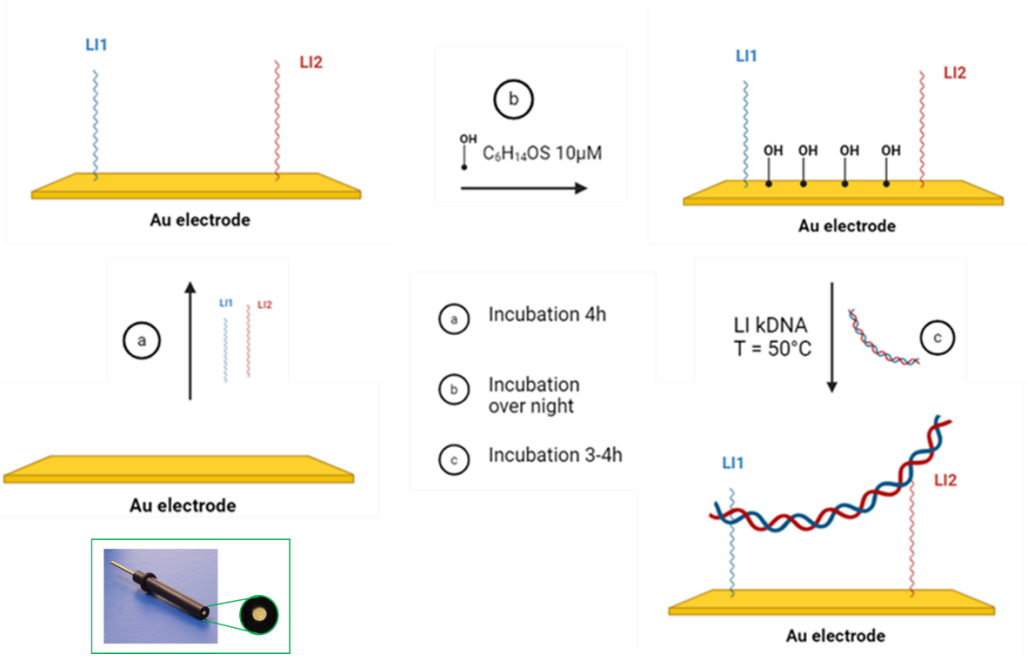

Figure 2.4. Electrode gold surface preparation; a) Immobilization of specific probes LI_1 and LI_2 and of b) 6-Mercapto-1-hexanol on the surface of a gold electrode; c) recognition of LI kDNA by surface cooperative hybridization.

2.1.2. Surface characterization analysis and sensing tests

Once functionalized, the gold substrates were used for two task: 1) *sensing surface chemical-physical characterization*; 2) *PCR-free sensing of LI kDNA by electrochemical analysis*.

The first task was focused on the investigation of the wettability and isoelectric properties of the sensing surface and was performed by CA and SFE analysis. For the measurements, a drop of 1 µL of ultrapure water was spotted on top of the gold substrate and the CA of drop was acquired after 10s. The analysis was performed on a clean gold substrate, used as reference, and substrates functionalized with probes and probes-target interfaces. All contact angle values, measured in four replicas (n = 4). In parallel, the SFE was also evaluated by applying the Owens Wendt Rabel and Kaelble (OWRK) model[171,172] in CA. In this case, it was dosed 1µL of ultrapure water and 1µL of diiodomethane as reference values for the SFE calculation. For the isoelectric properties analysis, the CA of 0.2 M phosphate buffer at pH 6.01, 0.2 M acetic acid/acetate buffers at pH 5.05, 4.01, acetate solution at pH 3.1 and hydrochloric acid 0.1 M at pH 2 drops were measured on step-by-step functionalized gold substrates. This acidic pH range, from 2 to 7, has been chosen to include the value of 5.5 at which the cooperative hybridization between LI probes and kDNA occurs.

The second task devoted to the PCR-free sensing test was performed electrochemically and characterised step by step by CV and EIS analysis. The starting training was carried out at the University of Bologna supervised by the Proff. Giovanni Valenti and Luca Prodi. The electrochemical measurements were performed by using the portable potentiostat PalmSens4 (Palm Instrument, The Netherlands) connected to a laptop and controlled by PSTrace 5.10 software. An electrochemical cell was built to connect CHI101 Au electrode used as working electrode (WE), a Pt wire used as counter electrode (CE) and an Ag/AgCl electrode as reference electrode (RE). The measurements were carried out using a solution of 5 mM ferro/ferricyanide (1:1 v/v) in 0.1 M phosphate buffer (Pb) pH 6.8 as redox probe at room temperature.

In the case of EIS measurements, a frequency range between 0.1 Hz and 100 KHz, 10 frequencies per decade, at an open circuit potential, with a voltage amplitude of 0.01 V, was used. The electron transfer process, $[Fe(CN)_6]^{3-} + 1e^- \rightleftarrows [Fe(CN)_6]^{4-}$, has been studied using EIS[173,174]. Experimental data were fitted using PSTrace software for a common Randles circuit, **Figure 2.5.** This equivalent circuit, which is one of the simplest possible models describing processes at the electrochemical interface, consists of an active electrolyte resistance RS in series with the parallel combination of the double-layer capacitance constant phase element (CPE). To the above-mentioned components, the charge transfer resistance (R_{ct}) and the Warburg impedance (W) are added. The latter are related to the electron transfer process and the diffusivity of the redox probe between the solution and the electrode surface, respectively. CV measurements were performed in the range of − 0.35 V to + 0.6 V voltage with a scan rate of 0.1 V/s, optimized for these electrodes previously by Nikolau et al.[47]

.

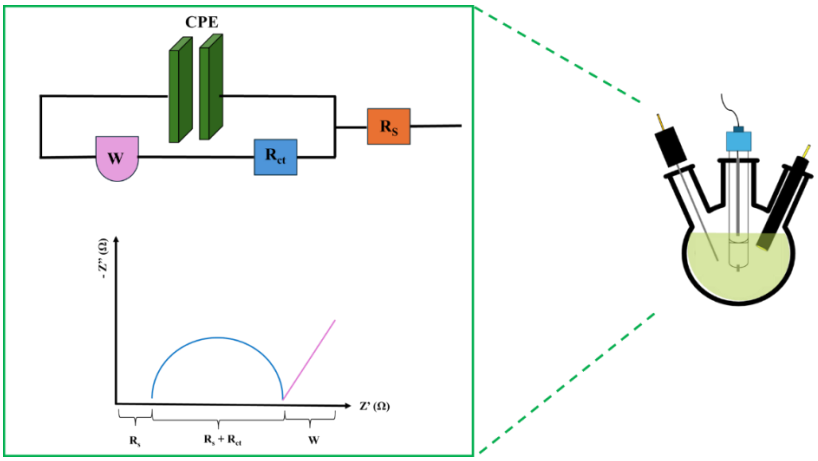

Figure 2.5. Schematic representation of equivalent Randles circuit. Rs: Ohmic resistance; Rct: charge transfer resistance; W: Warburg impedance; CPE: constant phase element.

2.1.3. Results and discussion

2.1.3.1. Sensing surface chemical-physical characterization

The bio-interface is a crucial component for biosensor since it strongly affects the bio-recognition processes and then, the performance of the sensing. This is particularly relevant for PCR-free detection where the starting target concentration are very low.[175] Therefore, CA characterization of DNA-gold functionalised interface has been performed in order to investigate the changes of surface charges occurring in the interfaces upon the bio derivatization and molecular recognition[176–178]. Contact angle measurements represent a fast and cheap way to evaluate the surface chemical properties of functionalized interfaces. CA is thermodynamically defined as function of a three-phase mechanical equilibrium that occurs in a solid-liquid-gas interface that is created by spotting a fluid drop on a solid surface[179]. This equilibrium is described by the Young's equation[180] (2):

$$\gamma_{lv}\, cos\theta y = \gamma_{sv} - \gamma_{sl} \quad (2)$$

where γ_{lv}, γsv and γsl represent, respectively, the liquid-vapor, solid-vapor and solid-liquid interfacial tensions and θy is the CA, as illustrated in **Figure 2.6a.** CA is primarily used to evaluate the surface wettability and morphology but, by controlling the variables related to the three-phase interface, CA could be used to study the surface isoelectric properties too.

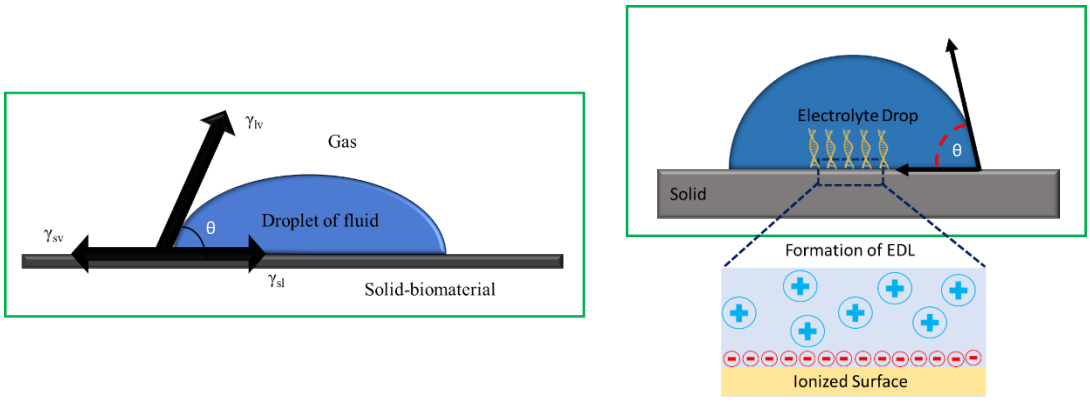

Figure 2.6. a) Contact angle (θ) in a three-phases interface formed by the liquid droplet on a solid-biomaterial and the surrounding gas. b) Scheme of the electrical double layer (EDL) produced by the droplet and the exposed surface charged functional groups.

The study of correlation between wettability[181] and CA allows to understand how the droplet diffuses on the solid substrate and to evaluate the droplet tendency to form surface interactions with the solid. Therefore, through this combined investigation is possible to obtain fundamental information on surface functionalization processes and applications based on phases interactions.

The correlation between surface wettability and pH can be, also, used as valid tool for the study of isoelectric properties and charge density of functionalized interfaces. The spotting of a drop of an electrolyte solution onto an interface create an electric double layer (EDL)[182], as shown in **Figure 2.6b.** Within EDL, the combination of counterions of drop with the charges of functional groups exposed by the interface generates an electrostatic attractive force and a potential that at certain pH decrease to zero (potential of zero charge, PZC), identifying an isoelectric condition of the functionalized interface. Therefore, by tuning the pH of the drop solution is possible to modify the charges environment of EDL and the CA value as function of the isoelectric properties of the studied interface.

A last parameter that correlates both wettability and surface charges is the surface free energy (SFE) which measures the surface tension of a substrate. SFE arises from molecular interactions at the air-solid interface so that the higher SFE value the more hydrophilic is the solid surface. In our work to calculate the SFE of the functionalized interface we employed the Owens-Wendt-Rabel-Kaelble (OWRK) model[171,172] by which the surface tension of the liquid, γ_{LV}, is calculated by the sum of a dispersive component (γ^{D}_{LV} e.g. Van der Waals interactions) and a polar component (γ^{P}_{LV}, e.g. hydrogen bonding). Also, the solid SFE (γ_{SV}) is a sum of dispersive and polar components such that $\gamma_{SV} = \gamma^{D}_{SV} + \gamma^{P}_{SV}$. The OWRK model, then, combines the liquid surface tension, solid SFE, and liquid-solid contact angle (θ) calculation into the following equation (3):

$$\gamma_{LV}(1 + cos\theta) = 2[(\gamma^{D}_{SV}\gamma^{D}_{LV})^{\frac{1}{2}} + (\gamma^{P}_{SV}\gamma^{P}_{LV})^{\frac{1}{2}}] \quad (3)$$

In this approach the solid is theoretically smooth and chemically homogeneous and the CA is measured from two liquids with known polar and dispersed

fractions of SFE. Every system strives to achieve equilibrium with a free energy state that is as low as possible.

Every system aspires to a state of equilibrium, solids, in particular, form an interface with a liquid to attempt to minimize free energy, therefore having a wettable surface[183]. Therefore, the SFE of a solid is closely related to its wettability, if high the surface of the solid will be wettable.

LI_1 and LI_2 probes were properly designed to recognize an inner region of the *L. infantum* kDNA. The probes sequences have been selected considering both dimension and degree of conservation of the complementary regions inside the genetic target. Moreover, it was guaranteed an optimal sequence composition, with a guanine-cytosine content percentage below 50%, a good melting temperature, between 50°C and 70°C, and a proper chemical derivatization, with alkyl thiol group added at the 5' end of the sequence for the SAM formation on gold.

The CA characterization of step-by-step functionalized DNA-gold interface is shown in Figure 10. The corresponding CA measures are plotted in Fig. 2.9a. Data highlight a marked increase of wettability after the Au cleaning step, passing from 80.76° ± 1.03° to 51.93° ± 3.34° of CA, that could be related to the formation of the thin hydroxyl layer on the gold surface. After the grafting of oligonucleotide probes the wettability increased again, as proved by the relevant decrease in CA of ~ 40° reported in figure 10. The reason of this trend was due to the addition of charges to the gold surface, brought by the hydroxyl, amino and phosphate groups of the oligonucleotide chains that led to a higher number of electrostatic interactions between the water drop and the surface.

The functionalized interface was, then, treated with 10^7 copies/µL of the kDNA target. The cooperative hybridization was performed according to a previous work of PCR-free detection of Hepatitis-B Virus genome.[47] The advantage in using such hybridization mechanism is that the two use-case probes simultaneously recognize and hybridize two close regions of the same kDNA molecule, with a recognition sequence gap of ~ 90 bp that minimizes the steric hindrance[184] in the probe-target interaction and increases both yield and stability of the DNA capture. As shown in **Figure 2.7a**, CA analysis after the

step of kDNA hybridization proved that the interface almost maintained the high hydrophilicity and wettability, reporting a value of 16.58° ± 1.13°. This slight increase of CA value, compared to that measured on interface with probes only, could be due to the molecular recognition.[185] Indeed, the binding between oligo and target chains causes a partial shielding of the charges exposed by functional group of single strand probes affecting the interface polarity.

To support our hypotheses, an SFE analysis in OWRK method was performed on DNA-gold interface before and after the kDNA hybridization. The results for the interface exposing probes only, described in **Figure 2.7b-LI probes**, reported a high SFE value of 73.60° ± 0.90 mN/m with a predominant polar part at 58.27 ± 1.55 mN/m, due to the addition of oligonucleotides charges. The analysis after the kDNA hybridization, in **Figure 2.7b-LI probes-kDNA**, showed an SFE value of 70.66 ± 0.80 mN/m that proved the surface wettability was kept after the cooperative hybridization. However, a lower value of the polar part at 50.17 ± 1.03 mN/m was also observed, clearly proving the double helix formation and the charges shielding effect as consequence of probe-target hybridization.

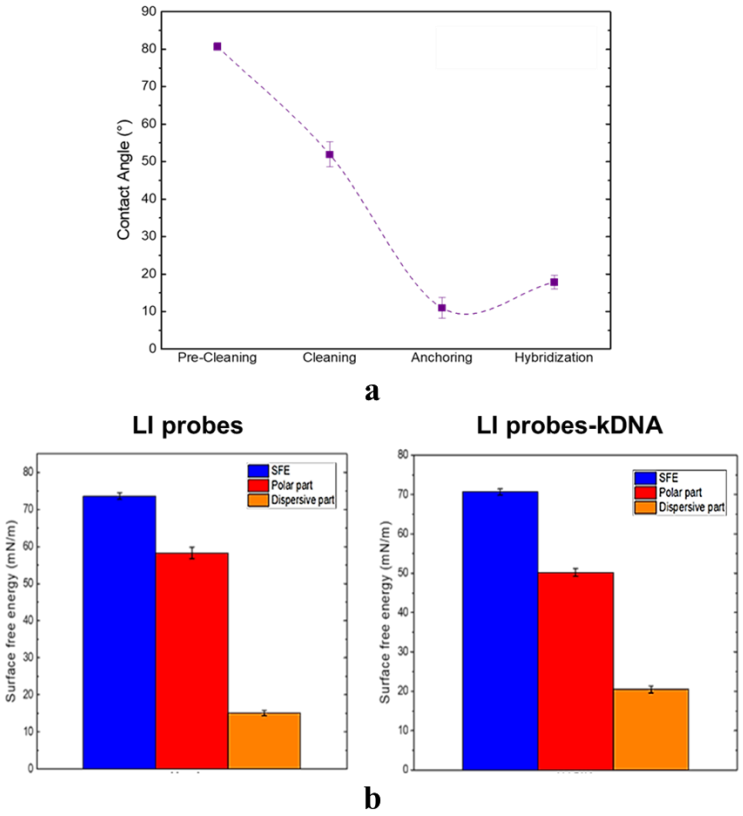

Figure 2.7. a) step-by-step CA characterization of functionalized interface; b) SFE analysis on DNA-gold functionalized interface before (LI probes) and after (LI probes-kDNA) the kDNA hybridization.

To further investigate the bio-interface properties, we performed a CA study at various pH. The isoelectric properties and PZC of LI probes and LI probes-target (kDNA) interfaces have been analyzed through CA measurements at various pHs and results are reported in **Figure 2.8.** Actually, in the aqueous environment of the studied DNA-gold interfaces the equilibrium can be easily altered by changing the pH and the surface hydrophilicity[186] since the anchored biomolecules can be both positively and/or negatively charged with respect to their isoelectric properties and the point of zero charge (PZC).[187–189]

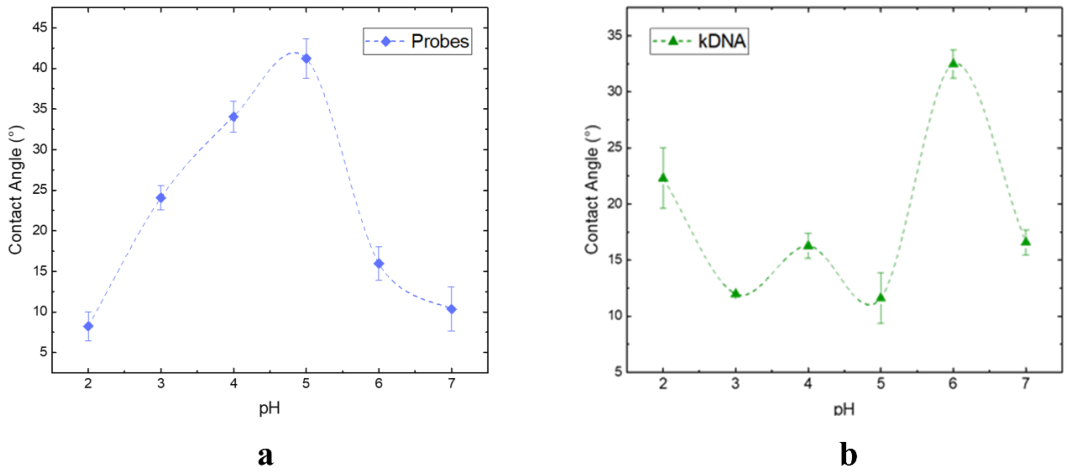

Figure 2.8. CA analysis of LI probes (a) and LI probes-target interface (b) at various pHs.

CA measured on the interface modified with LI probes only, **Figure 2.8a**, reached a maximum of 41.24° ± 2.43° at pH 5, considered as possible PZC value, and decreased at other pHs. This trend could be explained as the consequence of the ionization of DNA amino, hydroxyl and phosphate groups when the pH is away from their PZC causing the increase of interface hydrophilicity and surface wettability.

In the case of interface with LI probes and kDNA, **Figure 2.8b**, the average contact angles highlighted a maximum of 32.47° ± 1.25° around pH 6 and, again, decrease at pHs that were different from the PZC. The pH values obtained for the probes only and for kDNA probes are consistent with the results obtained by. The values of pH 5, **LI-probes**, and pH 6, **LI-probes-kDNA**, are consistent with literature data[184,190]. In fact, the use of acidic or slightly acidic hybridization buffer can lead to the protonation of the -G and –C groups of the nucleic acid that promotes a stronger binding with the probes. Lastly, a slight increase, however, was observed also at pH 2, probably, since the kDNA molecule at that pH tends to denature and alter its isoelectric profile.

This investigation was included in the work entitled “Advanced DNA–Gold Biointerface for PCR-Free Molecular Detection of Leishmania infantum” published on Advanced Materials Interfaces journal in 2024[191].

2.1.3.2. PCR-free sensing of LI kDNA by electrochemical analysis

CV and EIS analysis were used to assay the electrochemical behaviour of the electrode/electrolyte interface at each step of the biointerface fabrication and to perform the LI kDNA PCR-free detection.

The CV and EIS responses obtained by using $[Fe(CN)_6]^{3-/4-}$ as electroactive probe are shown in **Figure 2.9a** and **2.9b**, respectively. In particular, the frequency response from the EIS measurements were fitted to the Randles equivalent circuit (**Figure 2.5**), from which the charge transfer resistance, R_{ct}, was extracted.

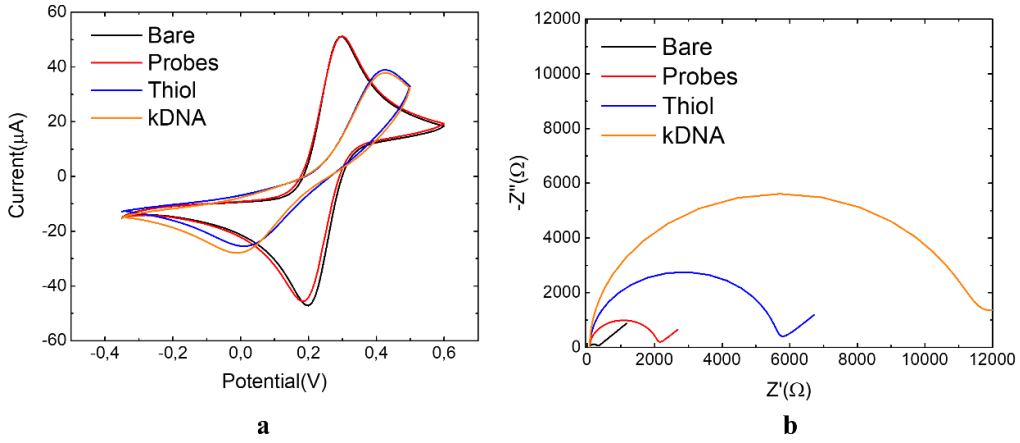

Figure 2.9. Electrochemical characterization of Au electrode interfaces during the multistep biosensor build-up using a L. Infantum DNA concentration of 10^4 cps/μL. a) Cyclic voltammograms and b) Nyquist's Plot recorded in 5 mM $[Fe(CN)_6]^{3-/4-}$ in 10mM PBS.

The voltammograms depicted in **Figure 2.9a**, reveal the effects of different chemical and biological layers on the electrical conductivity and resistivity of the electrode/electrolyte interface, influencing the performance of the WE. In particular, the cooperative hybridization between probe and kDNA produces a significant dysregulation in the magnitude of both voltametric peaks, reported respectively as anodic and cathodic current peaks (I_{pa} and I_{pc}). This is due to a different in the diffusivity of the redox probe near the WE interface, resulting

from the sequential immobilization on the electrode surface of probe, thiols and the final addition of the LI kDNA. Similarly, Nyquist plots show an increase in the total impedance of the system (bare-DNA) indicating that greater coverage of the electrode surface leads to a slower electron transfer rate and greater resistance to charge transfer compared to the platform naked. These phenomena are attributable to the coating layer of the electrode surface, which became thicker with the assembly procedure, thus reducing the permeability $[Fe(CN)_6]^{3-/4-}$ through the immobilization of the layers.

The layer-by-layer electrochemical characterization of the detection strategy gold electrode-based kDNA, resumed in **Table 2.2**, focused on the following types of surface modifications.

Bare-Au: for bare-Au a typical electrochemically reversible couple voltammogram was obtained. In fact, both species (Fe^{2+} and Fe^{3+}) rapidly exchange electrons with the working electrode and the peak-to-peak separation is lower than 59 mV/e^- (**Figure 2.9a**, black line). Consistently, the Nyquist plot (**Figure 2.9b**, black line) shows a smaller semicircle domain in comparison with the modified gold surfaces, indicating a small charge transfer resistance (R_{ct}), meaning a small resistance encountered by the electron as it travels between the redox species and electrode surface. Low R_{ct} values (132Ω) indicate a more electrochemically active surface[192].

Probes anchoring: the effectiveness of thiol-terminated probes LI_1 and LI_2 grafting onto the electrode surface was tested using a 1 μM probes mix. The choice to use the mixture of the two probes at this concentration was not arbitrary. In fact, this condition was required to allow the probes to be efficiently dispersed and to anchor the electrode surface through the thiol-Au complex formation in a SAM configuration. The SAM enabled the probes to be exposed in the right orientation for the sensing interaction to the genetic target[140]. Then, a washing step performed by rinsing the electrode with drops of PBS buffer was used to remove the unbound probes from the surface. From the voltammograms reported in **Figure 2.9a** (red line), it is possible to observe a little decrease in the magnitude of the voltametric peaks (I_{pa}, I_{pc}) for LI probes

and an important increase in the peak-peak separation (ΔE = 0.110 V ± 0.0001V) compared to bare-Au. This can be attributed to the shielding characteristic of the grafted probes layer, which gradually hinders the transport of electrons on the surface of the gold electrode[193]. To obtain further information on the functionalization of the WE, EIS analysis was also employed, **Figure 2.9b.** A clear increase in the total impedance was observed between Au-bare (R_{ct} = 132Ω) and electrode functionalized with probes. In fact, there is an increase in the total impedance; **Figure 2.9b** red line, R_{ct} =1610Ω ± 275.5 Ω. This effect is due to the chemical properties of the probes which prevent for the most part of Faradaic currents from penetrating to the surface (due to the high insulating properties of the thiol)[194]. Indeed, the reaction rate of the iron/ferricyanide couple for this step becomes gradually slower than the previous one.

Passivation: After grafting the probes, we therefore exploited the ability of a passivating molecule (6-mercapto-1-hexanol) to cover the uncovered sites of the functionalized surface with a solution of 10μM in PBS buffer overnight. A washing step, in PBS buffer, was performed to remove the excess of 6-mercapto-1-hexanol from the surface. The choice of using a passivating molecule is important to stabilize the assembled layer of the specific probes LI_1 and LI_2 and thus obtain homogeneously distributed arrays of probes. From the voltammograms reported in **Figure 2.9a** (blue line), it is possible to observe a significant decrease in the magnitude of the voltammetric peaks (I_{pa}, I_{pc}) for the passivating molecule and an important increase in the peak-peak separation (ΔE = 0.356V ± 0.005V) compared to bare-probes. This can be attributed to the highly shielding characteristic of the grafted organic layer, which gradually hinders the transport of electrons on the surface of the gold electrode.

To obtain further information on the functionalization of the WE, also in this case, EIS analysis was also employed, **Figure 2.9.** A sharp increase in the total impedance was observed between Au-probes and electrode functionalized with passivating. In fact, there is an increase in the total impedance; **Figure 2.9b** blue line R_{ct} = 6017Ω ± 542.88 Ω. This effect is due

to the chemical properties of the passivating which prevent almost all Faradaic currents from penetrating to the surface (due to the high insulating properties of the thiol)[195]. Indeed, the reaction rate of the iron/ferricyanide couple for this step becomes gradually slower than the previous one, as shown by the increased peak-to-peak separation (form of reversible voltammograms).

Table 2.2. Charge transfer resistance (R_{ct}), peak-to-peak separation, anodic and cathodic peak ratio (I_{pa}/I_{pc}), estimated for SPGE using CV and EIS in 5 mM $[Fe(CN)_6]^{4-/3-}$, in Pb pH 6.8, during kDNA detection strategy construction. Average values of at least 3 Au electrodes are presented.

kDNA (cps/µL)	R_{ct} (Ω)	ΔE(V)	I_{pa}/I_{pc}
Bare	132 ± 17	0.100 ± 0.01	1.04 ± 0.02
Probes	1610 ± 270	0.110 ± 0.001	1.06 ± 0.01
Thiol	6017 ± 500	0.356 ± 0.005	8.08 ± 1.51
kDNA 10^4	10166 ± 1200	0.393 ± 0.005	3.50 ± 0.10

LI kDNA hybridization: the voltammograms reported in **Figure 2.9a** (orange line), reported a further slight decrease of the current peaks (I_{pa}, I_{pc}) and an increase in peak-peak separation (ΔE = 0.393V ± 0.005V) after the functionalized electrode exposure to the kDNA target, compared to the previous condition with only probes and thiol passivator. This was attributed to the probes-target cooperative hybridization and the genetic material addition to the previously formed surface dielectric, demonstrating the ability of this strategy to directly detect the LI kDNA without further PCR amplifications.

Lastly, further information on the functionalization of the WE was obtained, through the EIS analysis, **Figure 2.9b** (orange line). A clear increase in the total impedance between Au-bare, probe-thiol and electrode functionalized with target DNA. In fact, the EIS analysis shows that the diameter of the semicircles in the Nyquist plots increases with the addition of the *L. infantum* DNA used and there is therefore an sharp increase in the total impedance; R_{ct} =10166Ω ± 1258.3Ω. This effect is due to the chemical properties of DNA that prevent almost all Faradaic currents from penetrating to the surface (due to

the high insulating properties of the thiol). In fact, also in this case the reaction speed of the iron/ferricyanide couple becomes even slower than in the previous one, as demonstrated by the increased peak-peak separation.

The analytical performance of the detection strategy was tested with different LI kDNA concentrations ranging from 0 to 10^4 cps/µL. Then, the electrodes were incubated for 3.5h at 50°C, so that the hybridization process between the strands occurs. **Figure 2.10a**, represents the Nyquist plots recorded after hybridization. The impedance responses comprised simply a semicircle related to the charge transfer process across the constructed biointerface. After hybridization, the total impedance R_{ct} of the electrodes increased in a concentration-dependent behaviour The Nyquist plots were characterized with the equivalent circuit shown, as done previously, in **Figure 2.9b**. The equivalent circuit was fitted to the Nyquist plots and the dependence of the charge transfer resistance values on the kDNA concentration (using three equally prepared electrodes) is shown in Figure 2.7b. The obtained results indicated the higher the DNA concentration bigger the recorded R_{ct} (**Figure 2.10b**).

The reproducibility of the response of the detection strategy was investigated by analysis of four concentrations of kDNA using three equally prepared electrodes for each concentration, and a relative standard deviation for each concentration used was calculated (**Table 2.3**). The goodness of the correct functioning of the method was then obtained by plotting on the x-axis the four types of kDNA concentration versus ΔR_{ct}. ΔR_{ct} was calculated by the following equation (1):

$$\Delta R_{ct} = R_{kDNA} - R_{p-t} (1)$$

Where R_{p-t} is the value of charge transfer resistance value when probe and passivator are immobilized on the electrode surface and R_{kDNA} is the charge transfer resistance value after the cooperative hybridization with kDNA is established. The dependence of ΔR_{ct} values on kDNA concentration is shown in **Figure 2.10c**. In particular, the LOD and LOQ values were 1 and 10 cps/µL respectively with values of 334.6Ω ± 875.5Ω and 555Ω ± 326.07Ω, leading to

hypothesize a possible future application of the developed strategy to real biologic samples.

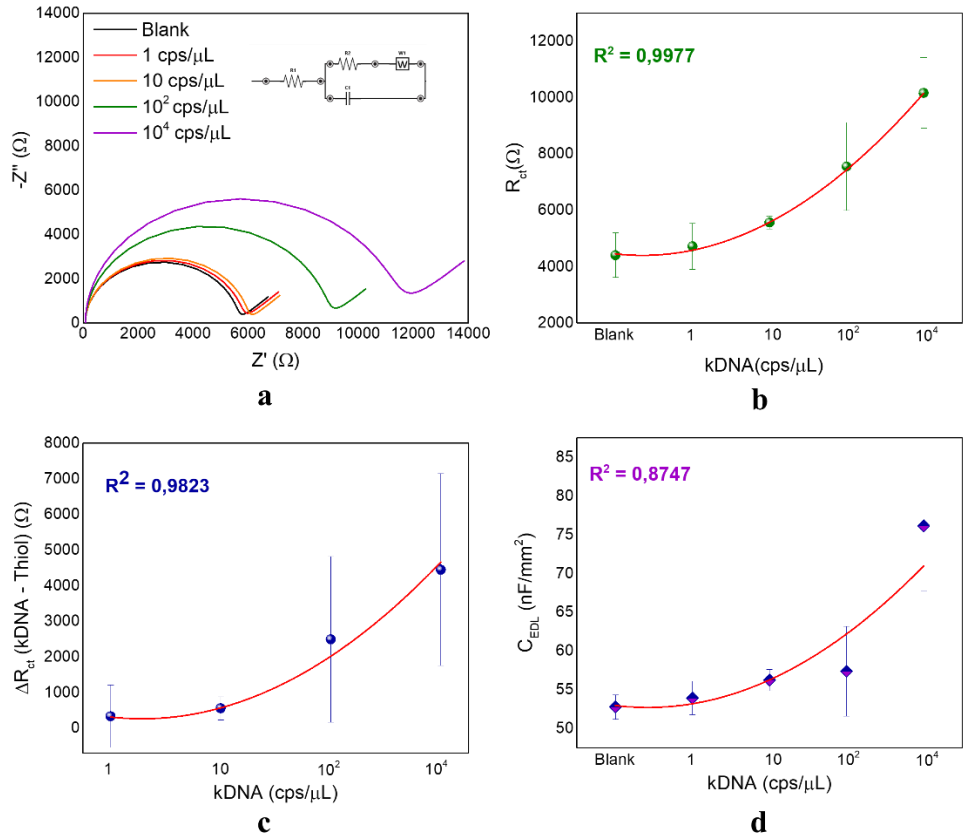

Figure 2.10. Analytical performance of kDNA detection strategy. a) Nyquist's Plot using different kDNA concentration in the range 0–10^4 cps/µL; b) Calibration curve obtained using different kDNA concentration in the range 0–10^4 cps/µL; c) Calibration curve obtained plotting ΔR_{ct} (kDNA – Thiol) vs different kDNA concentrations 1–10^4 cps/µL; d) Calibration curve obtained plotting C_{EDL} vs different kDNA concentrations 0–10^4 cps/µL in 5 mM $[Fe(CN)_6]^{4-/3-}$ in 0.2 M Pb. The error bars in panel b,c,d are the standard deviation calculated on 4 independent electrodes for each tested kDNA concentration and 3 independent electrodes for each zero-dose measurement.

Finally, it was interesting to evaluate the capacitance of the electric double layer (EDL) at the electrolyte-semiconductor interfaces. Indeed, the gold electrode used as WE was "transformed" into a semiconductor material after the various functionalization. Consequently, when a semiconductor material interacts with liquid electrolytes (in our case the iron/ferricyanide couple), an

electric double layer (EDL) is formed, which can have a significantly high charge transport capacity, in times as high as 8.0 × 10^{14} cm^{-2} at the ionic liquid/solid interfaces[196]. The EDL formed at the semiconductor/liquid interfaces is mainly capacitive, due to the presence of a large interfacial capacitance and the high-density charge storage capability.

Table 2.3. Charge transfer resistance (R_{ct}), peak-to-peak separation (ΔE) and Capacitance EDL (C_{EDL}) estimated for different concentrations of *L. infantum* kDNA using CV and EIS in 5 mM $[Fe(CN)_6]^{4-/3-}$, in Pb pH 6.8.

kDNA (cps/µL)	R_{ct} (Ω)	ΔE(V)	C_{EDL}(nF/mm^2)
0	4407 ± 700	0.356 ± 0.005	52.8± 1.5
1	4722 ± 800	0.330 ± 0.010	53.9 ± 2.1
10	5564 ± 230	0.340 ± 0.010	56.2 ± 1.3
10^2	7555 ± 1500	0.350 ± 0.017	57.4 ± 5.8
10^4	10166 ± 1200	0.393 ± 0.005	76.2 ± 8.4

However, the capacitance of the double layer (C_{EDL}) is generally enhanced at liquid-semiconductor interfaces when the interface is used for biosensing as a result of the formation of biomolecular complexes[197], in our case probe-thiol-kDNA. The C_{EDL} actively changes with the concentration of the biomolecular bond, so we expected a linear increase with the concentration of kDNA employed. The different C_{EDL} were evaluated by EIS measurements at the same frequency for all substrates. **Figure 2.10d** shows the dependence of C_{EDL} values on kDNA concentration from 1 cps/uL to 10^4 cps/uL along with the zero-dose measurement (blank), which is considered a baseline measurement. In particular, the calculated C_{EDL} values confirm the previously detected LoD and LoQ in EIS for 1 and 10 cps/µL with the values of 53.92 ± 2.17 nF/mm^2 and 56.24 ± 1.38 nF/mm^2. These results demonstrate that there is a higher charge accumulation at the electrode interface as the kDNA concentration increases, thus demonstrating that more biomolecular bonds are formed[198] due to increased cooperative hybridization.

The selectivity of the detection method was evaluated by impedimetric measurements in the presence of hepatitis B virus (HBV) DNA 10^4 cps/µL.

Hepatitis B virus DNA was chosen because of its similarity to LI DNA in terms of shape and size. In fact the HBV genome DNA is a relaxed-circular DNA (rcDNA) of approximately 3.2 kb in length with a complete minus strand and an incomplete plus strand[199]. The signals ΔR_{ct} obtained (DNA - Thiol) for this unspecific HBV DNA (US) were compared with those of the four concentrations of kDNA previously illustrated. The signals ΔR_{ct} obtained (DNA - Thiol) for these solutions were compared with those for the standard solution in the absence of any interferent. The results reported in **Table 2.4.** indicated high selectivity of the fabricated sensors, in fact the ΔR_{ct} values were not affected by the presence of HBV DNA.

Table 2.4. Difference charge transfer resistance (ΔR_{ct}) DNA-Thiol and peak-to-peak separation (ΔE) estimated for different concentrations of L. Infantum kDNA and US Hepatitis b virus DNA using CV and EIS in 5 mM $[Fe(CN)_6]^{4-/3-}$, in Pb pH 6.8.

kDNA (cps/µL)	$\Delta R_{ct}(\Omega)$	$\Delta E(V)$
1	335 ± 870	0.34 ± 0.01
10	555 ± 320	0.34 ± 0.01
10^2	2325 ± 2300	0.35 ± 0.02
10^4	4449 ± 2700	0.39 ± 0.01

2.2. Development RNA strategy for PCR-free molecular detection of SARS-CoV-2

Since January 2020 the world has been forced to face SARS-CoV-2, beloging to the Coronaviridae family and responsible for the human severe respiratory syndrome of COVID-19[200–202]. From its first report in Wuhan, China, the SC contagion quickly spread worldwide becoming a pandemic, as declared by the World Health Organization (WHO), bringing up more than 600 million infected people and 6.5 million deaths[203,204]. Currently, the most reliable test is based on a molecular analysis of swab sample by reverse-transcriptase polymerase chain reaction (RTPCR), which, according to the guide lines of the WHO and the American Center for Disease Control (ACDC), is considered the unique

standard for COVID-19[205] diagnosis. This molecular technique focuses on the detection and quantification of the SC genome, consisting in a 30 Kb single strand (ss)RNA encoding for: spike protein (S), that is affine towards the angiotensin converting enzyme 2 (ACE 2) receptor exposed by host cell, involved in the infection process; matrix protein (M), responsible for the nutrients transmembrane transport and viral envelope formation; small envelope (E) and nucleocapsid (N) protein, which affect the immune response; non-structural proteins, such as 3-chymotrypsin-like protease and RNA-dependent RNA polymerase[206,207]. So far, although extremely consolidated and highly accurate, the RT-PCR method includes two steps of genome target pre-amplification that make harder the laboratory procedures. In the standard RT-PCR, indeed, the viral RNA of SC must be reverse transcribed into complementary DNA and then amplified through PCR. Moreover, notwithstanding the growing efforts to improve the speed of the molecular analysis and integrate it into PCR-based biochip[208] systems, mostly need for qualified personnel and the use of costly reagents so that they can be used only in a laboratory environment. Therefore, these methods are not suitable for large-scale diagnosis, limiting, de facto, their massive use for screening and control of COVID outbreak.

Other COVID-19 tests were, instead, based on the immunological tests that provided rapid diagnosis, within 20 min, to be used in the frontline testing. However, these methods caused a high rate of false-negative results[209] limiting their reliability.

Therefore, in order to control and mitigate this kind of viral infections avoiding any risk for future pandemic outbreaks it is mandatory to introduce new diagnostic tools for fast, accurate and more accessible viruses identification. In this scenario, the development of PCR-free PoC sensors could certainly make a revolution in the molecular diagnostics allowing the possibility to decentralize and make faster the molecular analsysis[47,175,208,210].

In the present section, the development of a PCR-free biosensing strategy for quantitation of SC ssRNA is reported. As described in the previous section for

LI kDNA sensing, we functionalized the surface of gold substrates by grafting specific thiolated oligonucleotides probes for the SC ssRNA cooperative hybridization.

2.2.1. Experimental

Probes for the PCR-free detection of SC ssRNA genome have been, again, developed by a first study of literature. The investigation evidenced the N gene, encoding the viral nucleocapsid phosphoprotein, as one of the most conserved regions inside the genome and, therefore, widely included as control in commercial kits for the molecular SWAB analysis. A combination of 3 thiol-modified probes (SC_P1, SC_P2 and SC_P3) has been designed for the cooperative hybridization with the 92 bases sequence of N gene, which is reported in the map and detail of **Figure 2.11a** and **2.11b**. The third probe SC_P3, binding the inner part of the recognition sequence, has been added to improve the selectivity of detection and the annealing performances.

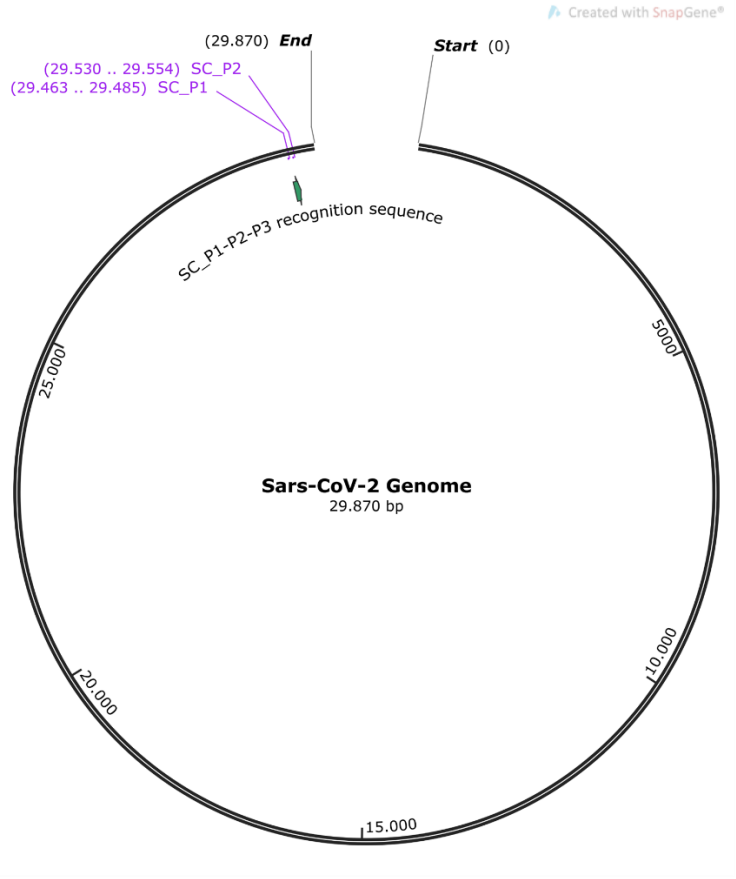

a

b

Figure 2.11. a) Map of the 29 Kb ssRNA of SARS-CoV-2; b) SC_P1, SC_P2 and SC_P3 recognition sequence.

Probes customized with a 5'-thiol-C6 modification (from MetaBion International AG), reported in **Table 2.5**, were used for the gold surfaces functionalization via SAM formation.

Table 2.5. Use case thiol-modified probes.

Probe	Sequence 5'-3'
SC_P1-T	HS-C6-GACGTCTAAACCTACTAAAGAGG
SC_P2-T	HS-C6-CCTTGTGTGGTCTGCATGAGTTTAG
SC_P3-T	HS-C6-TAACGTTGTTAGGTACTCGTCACGACTGAG

The target was a synthetic liophylized SC ssRNA genome (Amplirun) resuspended in DNAse and RNAse free water in a final concentration of 10^4 cps/µL.

The sensing surface properties were first investigated on Au-sputtered silicon substrate, that was functionalized with probes and SC ssRNA using X-ray photoelectron spectroscopy (XPS) and CA analysis. We performed the surface characterization analysis using four replicates for CA and three replicates for XPS of each functionalization step.

Subsequently, EIS and CV analysis were used to electrochemically assayed the PCR-free molecular detection of SC ssRNA, captured through cooperative hybridization. In this case, we performed the electrochemical analysis using four replicates for each functionalization step, four replicates for each tested RNA concentration and three of zero-dose measurement (blank), which is considered a baseline measurement.

2.2.1.1. Gold-sputtered silicon substrate functionalization

Gold-sputtered silicon substrate of 0.55 cm x 1 cm functionalization with SC probes and ssRNA target, schemed in **Figure 2.12,** was performed according to the following chemical protocol reported in section 2.1.1.1 for LI kDNA.

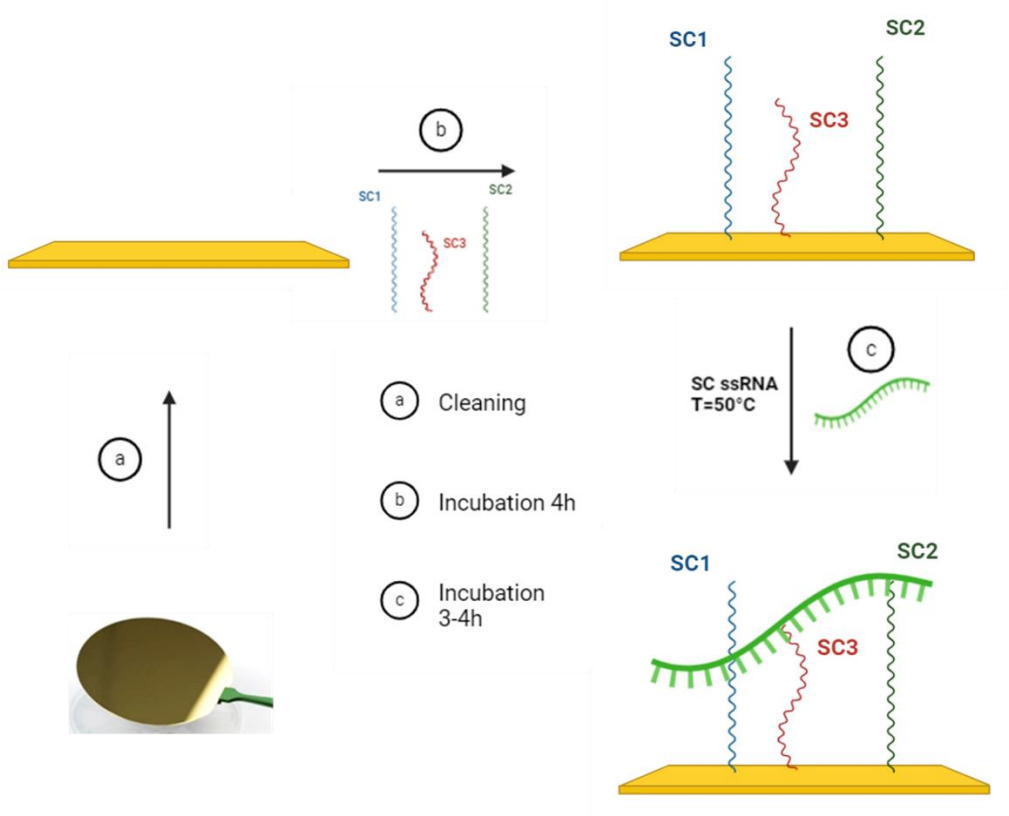

Figure 2.12. Gold substrate preparation, a) Surface cleaning with basic piranha solution; b) Immobilization of specific probes SC_1, SC_2 and SC_3 and c) recognition of SC ssRNA by surface cooperative hybridization.

For the not amplified genetic target hybridization, the syntethic SC ssRNA was diluted to 10^2 copies/µL in PBS at pH 5.5. The final gold interface functionalized with $SC_1/SC_2/SC_3$ probes were dipped in ssRNA solution at 50 °C for 3.5 h. Then, the unbound ssRNA was washed away from surface by PBS buffer.

2.2.1.2. Commercial gold electrode functionalization

The commercial CHI101 gold electrode was modified with the SC probes (**Table 2.5**) and ssRNA according to the functionalization scheme reported in **Figure 2.13** in according to what described previously in section 2.2.1.2. for LI kDNA.

For the not amplified genetic target hybridization, ssRNA was used at different concentrations (10^{-1}, 1, 10, 10^2 and 10^4 copies/µL) in PBS at pH 5.5, prepared by diluting the 10^6 copies/µL stock solution. The final gold interface

functionalized with $SC_1/SC_2/SC_3$ probes were dipped in ssRNA solution at 50 °C for 3.5 h. Then, the unbound ssRNA was washed away from surface by PBS buffer.

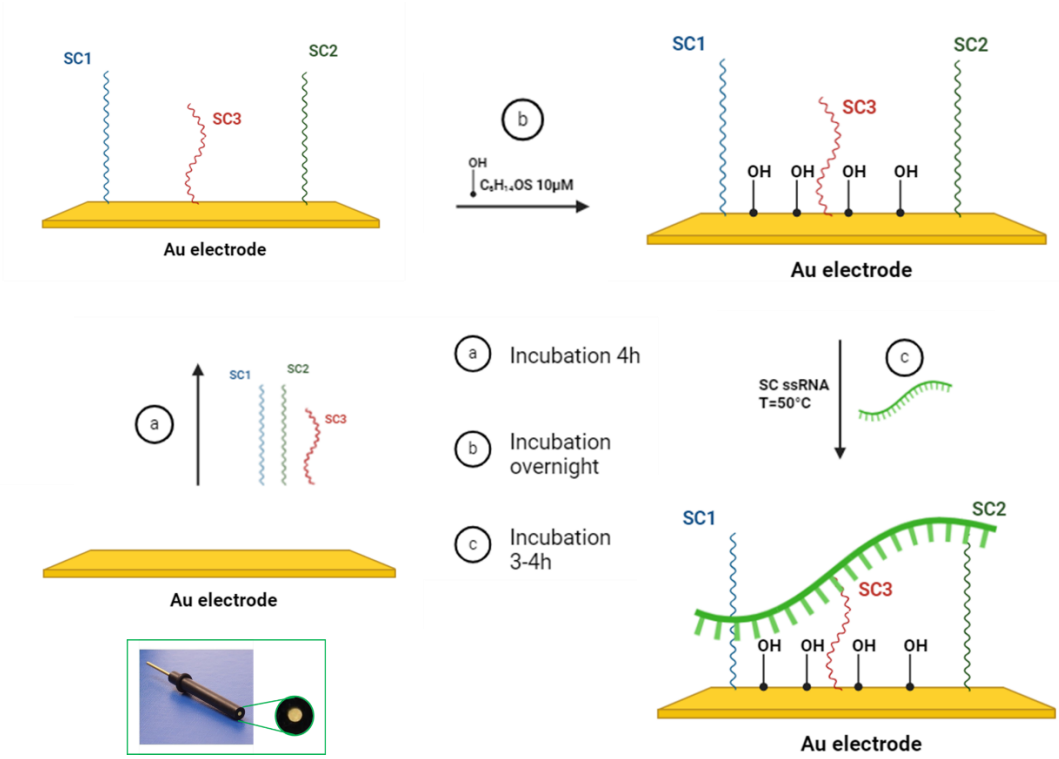

Figure 2.13. Electrode gold surface preparation; a) Immobilization of specific probes SC_1, SC_2 and SC_3 and of b) 6-Mercapto-1-hexanol on the surface of a gold electrode; c) recognition of SC ssRNA by surface cooperative hybridization.

2.2.2. Surface characterization analysis and sensing tests.

As already mentioned in the previous work for LI kDNA, the gold substrates were used in a two-step characterization: 1) *sensing surface chemical-physical characterization*; 2) *PCR-free sensing of SC ssRNA by electrochemical analysis*.

The sensing surface composition was studied by XPS, performed in collaboration with the group of Prof. G. Condorelli of the University of Catania. The spectroscopy was carried out using a PHI 5000 Versa Probe Instrument using a monochromatic Al Kα X-ray source excited with a micro-focused electron beam. All the analyses were performed with a photoelectron take-off

angle of 45° (relative to the sample Surface). The XPS binding energy (B.E.) scale was calibrated on the C_1s peak of adventitious carbon at 285.0 eV.
In parallel, the wettability and isoelectric properties of the functionalized sensing surface were evaluated by CA and SFE analysis. For the measurements, a drop of 1 µL of ultrapure water was spotted on top of the gold substrate and the CA of drop was acquired after 10s. The analysis was performed on a clean gold substrate, used as reference, and substrates functionalized with probes and probes-target interfaces. All contact angle values, measured in four replicas (n = 4). The SFE was done as described before for LI kDNA.

The second task related to the ssRNA PCR-free detection was done electrochemically by CV and EIS analysis. The measurements were performed using the same procedure as that already used for LI kDNA .

2.2.3. Results and discussion

2.2.3.1. Sensing surface chemical-physical characterization

The XPS analysis of the SC-functionalized gold surface was done focusing on the sensing interface chemical composition after each step of surface modification. The analysis of relative atomic concentrations, resumed in **Table 2.9**, showed an increase of carbon, oxygen and nitrogen levels in the Au-SC probes surface due to the organic chemistry of DNA probes that accumulated over the adventitious elements in the Au reference surface. The C1s band was deconvoluted into different components, as reported in **Figure 2.15a** and **2.15b**, most of which became prominent in the Au-SC probes surface as consequence of the C-C, C-O and C-N bonds brought by the aromatic nucleobasis of probes. This data was supported by the N1s signal (**Figure 2.15c**) whose peak appeared only in presence of probes. The increase of the S_2p signal, reported both in **Table 2.9** and **Figure 2.15d**, was instead related to the thiol group of probes that was used for the covalent binding of SAM to the surface, proving the effectiveness of the molecules anchoring to the electrode.

Table 2.9. Atomic concentrations comparison.

Surfaces	C_1s	O_1s	N1s	S_2p	Au_4f
Au	25.59	16.08	1.13	0.28	54.75
Au-probes	39.70	19.2	6.42	0.39	21.42
Au-Probes-Target	42.62	23.27	4.25	1.02	23.81

On the contrary, the Au_4f peak concentration reported in table decreased in the Au-SC probes surface. This was probably due to the good coverage of anchored capture probes that exclude the underneath Au layer from the XPS reading.

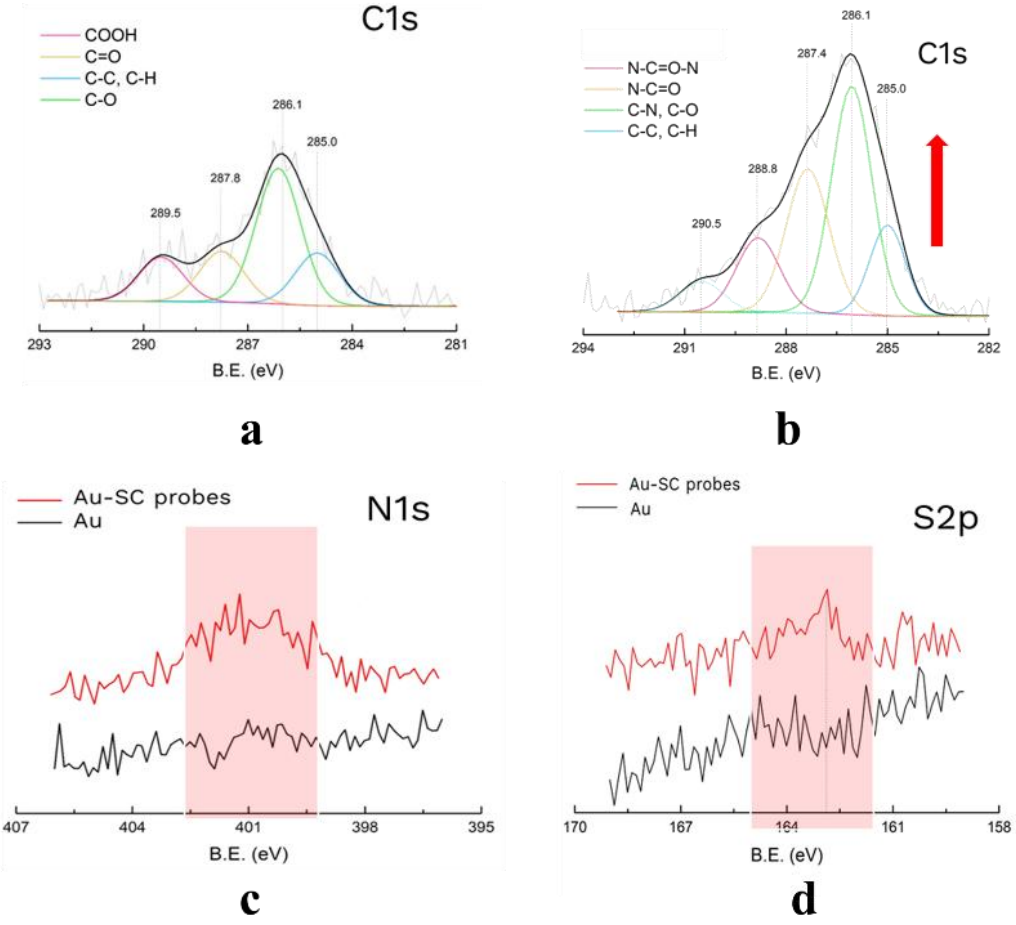

Figure 2.15. Deconvolution of C_1s peak of Au (a) and Au-SC probes (b) surface. XPS analysis of N_1s (c) and S_2p (d) peak

Furthermore, after the addition of Sars-Cov-2 ssRNA, the amount of C1s further increased because of the C-C, C-O and C-N bonds contributed by the aromatic nucleobase of the probes and ssRNA. This finding was supported by the N_1s signal (**Figure 2.16b**) whose smoother peak compared to the N_1s signal (**Figure 2.16a**) can be attributed to the formation of hydrogen bonds between the probes and the genome (cooperative hybridization)[211,212].

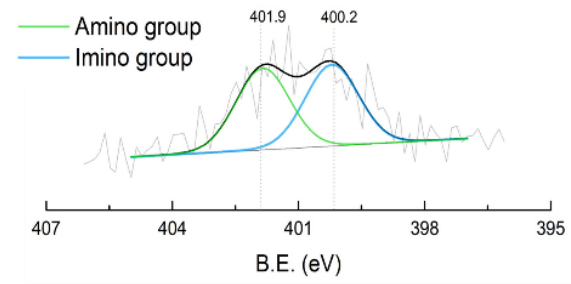

a

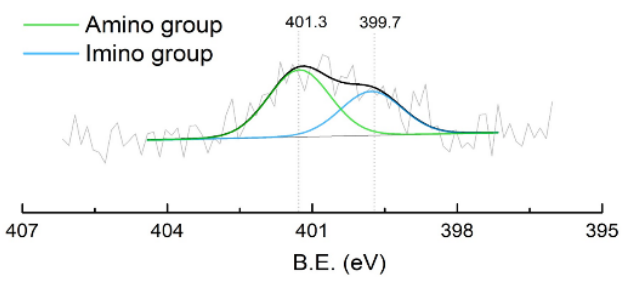

b

Figure 2.16. Deconvolution of N_1s peak of Au-Probes (a) and Au-probes-target (b) surface.

Lastly, CA characterization of RNA-gold functionalised interface has been performed in order to investigate the sensing interface surface properties modification upon the functionalization and the molecular interactions[176–178].

The CA characterization of step-by-step functionalized RNA-gold interface is shown in **Figure 2.17**. The corresponding CA measures are plotted in **Figure 2.17a**. Data highlight a marked increase of wettability after the Au cleaning

step, passing from 80.76° ± 1.03° to 51.93° ± 3.34° of CA, that could be related to the formation of the thin hydroxyl layer on the gold surface. After the grafting of oligonucleotide probes the wettability increased again, as proved by the relevant decrease in CA of ~20° reported in **Figure 2.17a**. The reason of this trend was due to the addition of charges to the gold surface, brought by the hydroxyl, amino and phosphate groups of the oligonucleotide chains that led to a higher number of electrostatic interactions between the water drop and the surface.

As shown in **Figure 2.17a**, CA analysis after the hybridization with 10^2 copies/µL of the RNA target proved that the interface almost maintained the high hydrophilicity and wettability, reporting a value of 23.15° ± 1.43°. This slight decrease of CA value, compared to that measured on interface with probes only, could be due to the molecular recognition.[185] In fact, the binding between oligo and target chains causes an increase in polar groups on the biointerface exposed by both the functional groups of the probes and the ssRNA, that influence the polarity of the surface.

To support our hypotheses, the SFE analysis in OWRK method was performed on DNA-gold interface before and after the RNA hybridization. The results for the interface exposing probes only, described in **Figure 2.17b-SC probes**, reported a high SFE value of 64.48° ± 6.51 mN/m with a predominant polar part at 44.18 mN/m ± 4.9 mN/m, due to the addition of oligonucleotides charges. The analysis after the ssRNA hybridization, in **Figure 2.17b-SC probes-RNA**, showed an SFE value of 67.13 mN/m ± 7 mN/m that proved the surface wettability was kept after the cooperative hybridization. However, a higher value of the polar part at 48.59 mN/m ± 5.5 mN/m was also observed, clearly proving the double helix formation and the charges shielding effect as consequence of probe-target hybridization.

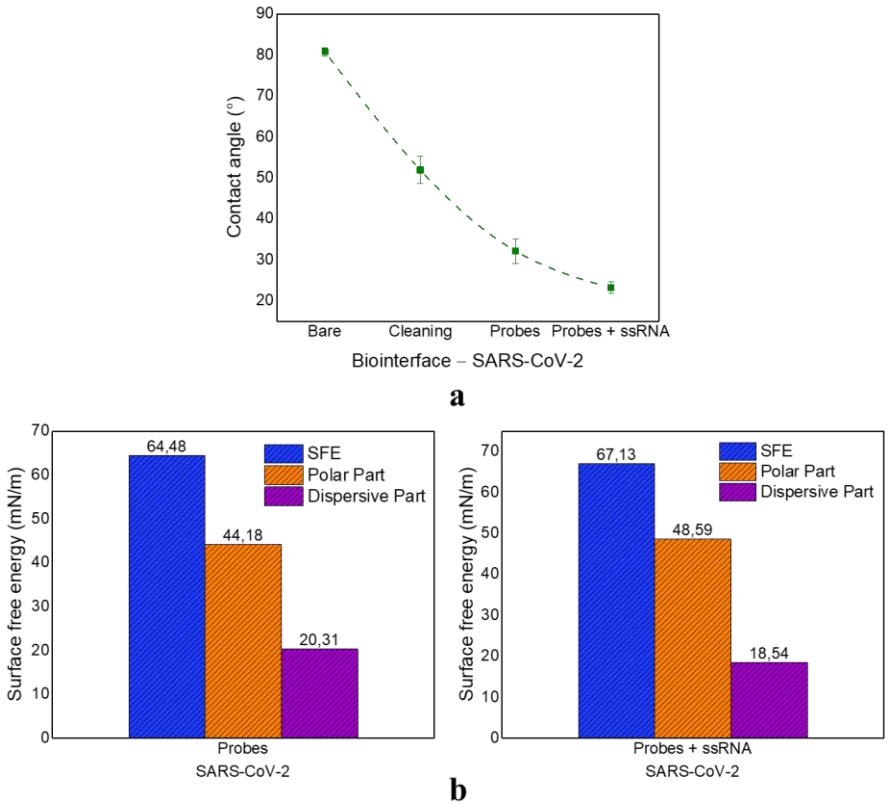

Figure 2.17. a) step-by-step CA characterization of functionalized interface; b) SFE analysis on RNA-gold functionalized interface before (SC probes) and after (SC probes-RNA) the RNA hybridization.

To further investigate the bio-interface properties, we performed a CA study at various pH. The isoelectric properties and PZC of SC probes and SC probes-target (RNA) interfaces have been analysed through CA measurements at various pHs and results are reported in **Figure 2.18**. Actually, in the aqueous environment of the studied RNA-gold interfaces the equilibrium can be easily altered by changing the pH and the surface hydrophilicity[186] since the anchored biomolecules can be both positively and/or negatively charged with respect to their isoelectric properties and the point of zero charge (PZC).[187–189]

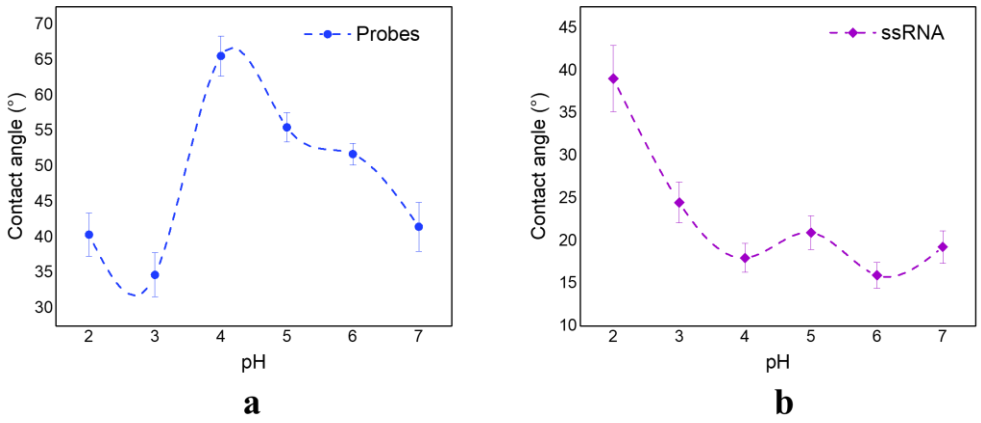

Figure 2.18. CA analysis of SC probes (a) and SC probes-target interface (b) at various pHs.

CA measured on the interface modified with SC probes only, **Figure 2.18a**, reached a maximum of 65.56° ± 2.8° at pH 4, considered as possible PZC value, and decreased at other pHs. This trend could be explained as the consequence of the ionization of RNA amino, hydroxyl and phosphate groups when the pH is away from their PZC causing the increase of interface hydrophilicity and surface wettability.

In the case of interface with SC probes and DNA, **Figure 2.18b**, the average contact angles highlighted a maximum of 39.06° ± 3.9° around pH 2 and, in this case the maximum is obtained at the pH value in which the RNA molecule at that pH tends to denature and alter its.

2.2.3.2. PCR-free sensing of LI kDNA by electrochemical analysis

The electrochemical analysis was used to deeply characterize the behaviour of the electrode/electrolyte interface at each step of the biosensor fabrication. Results of CV and EIS are shown in **Figure 2.19a** and **2.19b**, respectively. In particular, the frequency response from the EIS measurements were fitted to the Randles equivalent circuit (**Figure 2.5**), from which the charge transfer resistance, R_{ct}, was extracted.

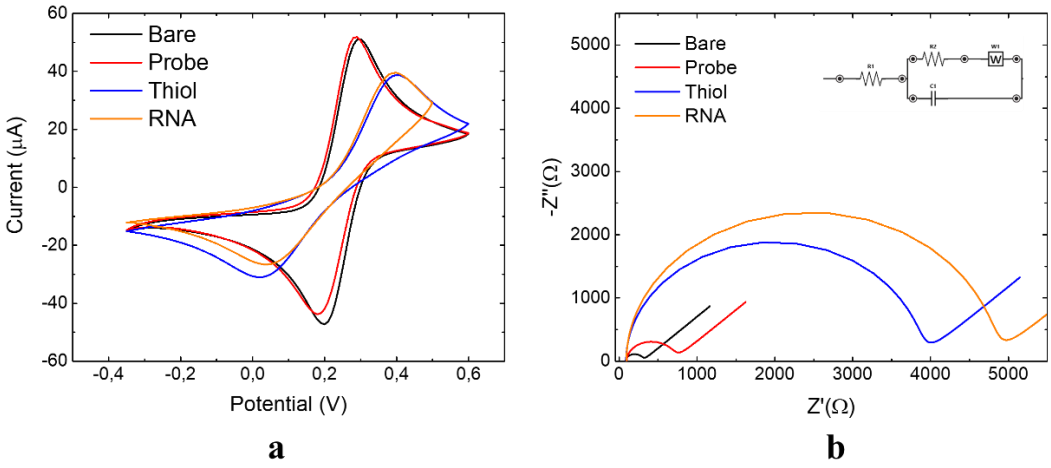

Figure 2.19. Electrochemical characterization of Au electrode interfaces during the multistep biosensor build-up using a Sars-CoV-2 RNA concentration of 10^4 cps/µL. a) Cyclic voltammograms and b) Nyquist's Plot recorded in 5 mM $[Fe(CN)_6]^{3-/4-}$ in 10mM PBS.

The voltammograms depicted in **Figure 2.19a**, reveal the effects of different chemical and biological layers on the electrical conductivity and resistivity of the electrode/electrolyte interface, influencing the performance of the WE. In particular, the cooperative hybridization between probe and ssRNA produces a significant dysregulation in the magnitude of both voltametric peaks, reported respectively as anodic and cathodic current peaks (I_{pa} and I_{pc}). This is due to a different in the diffusivity of the electro-active analyte near the WE interface, resulting from the sequential immobilization on the electrode surface of probes, thiol and the final addition of the SC ssRNA. Similarly, Nyquist plots show an increase in the total impedance of the system (bare-RNA) indicating that greater coverage of the electrode surface leads to a slower electron transfer rate and greater resistance to charge transfer compared to the platform naked. These phenomena are attributable to the coating layer of the electrode surface, which became thicker with the assembly procedure, thus reducing the permeability $[Fe(CN)_6]^{3-/4-}$ through the immobilization of the layers.

The electrochemical characterization of the functionalization and PCR-free detection of ssRNA, whose values are resumed in **Table 2.6**, focused on the following steps.

Bare-Au: for the bare-Au, a typical electrochemically reversible couple voltammogram was obtained. In fact, both species (Fe^{2+} and Fe^{3+}) rapidly exchange electrons with the working electrode and the peak-to-peak separation is lower than 59 mV/e^- (**Figure 2.19a**, black line). In line, the Nyquist plot (**Figure 2.19b**, black line) shows a smaller semicircle domain in comparison with the modified gold surfaces, indicating a small charge transfer resistance (R_{ct}), meaning a small resistance encountered by the electron as it travels between the redox species and electrode surface. Low R_{ct} values (132Ω) indicate a more electrochemically active surface[192].

Probes anchoring: the red line of voltammogram in **Figure 2.19a** showed a little decrease of the voltametric peaks magnitude for SC probes and an important increase in the peak-peak separation (ΔE = 0.110 ± 0.0001V) compared to bare-Au. This was correlated to the shielding characteristic of the grafted probes layer, which gradually hinders the transport of electrons on the surface of the gold electrode[193]. In addition, EIS analysis showed an increase of the total impedance was observed between Au-bare (R_{ct} = 132Ω) and electrode functionalized with probes. In fact, blue line of **Figure 2.19b** reported a R_{ct} of 730Ω ± 72.11 Ω. This effect was due to the chemical properties of the probes which prevent for the most part of Faradaic currents from penetrating to the surface (due to the high insulating properties of the thiol)[194]. Indeed, the reaction rate of the iron/ferricyanide couple for this step becomes gradually slower than the previous one.

Passivation: we therefore exploited the ability of a passivating molecule (6-mercapto-1-hexanol) to cover the uncovered sites of the functionalized surface with a solution of 10μM in PBS buffer overnight. A washing step, in PBS buffer, was performed to remove the excess of 6-mercapto-1-hexanol from the surface. The choice of using a passivating molecule is important to stabilize the assembled layer of the specific probes SC_1, SC_2 and SC_3 and thus obtain homogeneously distributed arrays of probes. From the voltammograms reported in **Figure 2.19a** (blue line), it is possible to observe a significant decrease in the magnitude of the voltametric peaks (I_{pa}, I_{pc}) for the passivating molecule and an important increase in the peak-peak separation (ΔE = 0.300

± 0.02V) compared to bare-probes. This can be attributed to the highly shielding characteristic of the grafted organic layer, which gradually hinders the transport of electrons on the surface of the gold electrode. Also in this case, the EIS analysis supported the characterization reporting a sharp increase of the total impedance, blue line in **Figure 2.19b**, passing from the Au-probes to the Au-probes-thiol functionalized electrode.

Table 2.6. Charge transfer resistance (R_{ct}), peak-to-peak separation, anodic and cathodic peak ratio (I_{pa}/I_{pc}), estimated for SPGE using CV and EIS in 5 mM $[Fe(CN)_6]^{4-/3-}$, in Pb pH 6.8, during genetic-SC-PoC fabrication. Average values of at least 3 Au electrodes are presented.

RNA (cps/µL)	R_{ct} (Ω)	ΔE (V)	I_{pa}/I_{pc} (µA)
Bare	132 ± 17	0.1 ± 0.01	1.05 ± 0.02
Probes	730 ± 70	0.110 ± 0.001	1.08 ± 0.02
Thiol	4409 ± 400	0.300 ± 0.02	1.57 ± 0.10
RNA 10^4	4911 ± 210	0.343 ± 0.001	8.85 ± 0.70

SC RNA hybridization: for the hybridization with the SC RNA, the voltammogram reported in **Figure 2.19a** (orange line) showed a further slight decrease in the magnitude of the peaks for RNA target and therefore an increase in peak-peak separation (ΔE = 0,343 ± 0,001V) compared to the probes and thiol grafted onto the WE surface. This was due to the cooperative hybridization formation and the material genetic addition to the previously formed surface dielectric, demonstrating the ability of this strategy to directly detect Sars-CoV-2 RNA without further amplification[213]. Further information on the functionalization of the WE was obtained via EIS analysis, **Figure 2.19b** (orange line). A clear increase in the total impedance between Au-bare, probe-thiol and electrode functionalized with target RNA. In fact, the EIS analysis shows that the diameter of the semicircles in the Nyquist plots increases with the addition of the Sars-CoV-2 RNA used and there is therefore a sharp increase in the total impedance[214]; R_{ct} = 4911.33Ω ± 210.6Ω. This effect is due to the chemical properties of RNA that prevent almost all Faradaic currents from penetrating to the surface (due to the high insulating properties of the

thiol). In fact, also in this case the reaction speed of the iron/ferricyanide couple becomes even slower than in the previous one, as demonstrated by the increased peak-peak separation.

The analytical performance of ssRNA detection strategy was tested with different SC ssRNA concentrations ranging from 0 to 10^4 cps/uL, **Figure 2.20**. Then again, the electrodes were incubated for 3.5h at 50°C, so that the hybridization process between the strands occurs. **Figure 2.20a**, represents the Nyquist plots recorded after hybridization. The impedance responses comprised simply a semicircle related to the charge transfer process across the constructed biointerface. After hybridization, the total impedance R_{ct} of the electrodes increased in a concentration-dependent behaviour. The Nyquist plots were characterized with the equivalent circuit shown, as done previously, in Figure 2.15b. The equivalent circuit was fitted to the Nyquist plots and the dependence of the charge transfer resistance values on the RNA concentration (using three equally prepared electrodes) is shown in **Figure 2.20b**. The obtained results indicated a tight correlation between RNA concentration and measured R_{ct}. The reproducibility of the response of the method was investigated by testing four concentrations of RNA with three equally prepared electrodes for each concentration, and a relative standard deviation for each concentration used was calculated (**Table 2.7**). The goodness of the correct functioning of the biosensor was then obtained by plotting on the x-axis the four types of RNA concentration versus ΔR_{ct}. ΔR_{ct} was calculated by the following equation (4):

$$\Delta R_{ct} = R_{RNA} - R_{p-t} (4)$$

Where R_{p-t} is the value of charge transfer resistance value when probe and passivator are immobilized on the electrode surface and R_{RNA} is the charge transfer resistance value after the cooperative hybridization with RNA is established.

Table 2.7. Charge transfer resistance (R_{ct}), peak-to-peak separation (ΔE) and Capacitance EDL (C_{EDL}) estimated for different concentrations of Sars-CoV-2 ssRNA using CV and EIS in 5 mM $[Fe(CN)_6]^{4-/3-}$, in Pb pH 6.8.

RNA (cps/μL)	R_{ct} (Ω)	ΔE(V)	C_{EDL}(nF/mm^2)
0	3896 ± 200	0.300 ± 0.02	45.5 ± 4.5
1	4127 ± 400	0.300 ± 0.03	47.8 ± 4.7
10	4367 ± 400	0.295 ± 0.02	48.4 ± 4.8
10^2	4650 ± 400	0.315 ± 0.03	53.2 ± 5.3
10^4	4911 ± 200	0.343 ± 0.001	55.3 ± 0.6

The dependence of ΔR_{ct} values on kDNA concentration is shown in **Figure 2.20c**. In particular, the LoD and LoQ values were 1 and 10 cps/uL respectively with values of 144 ± 414Ω and 90 ± 410Ω, leading to hypothesize a possible application of the developed detection strategy to real biologic samples.

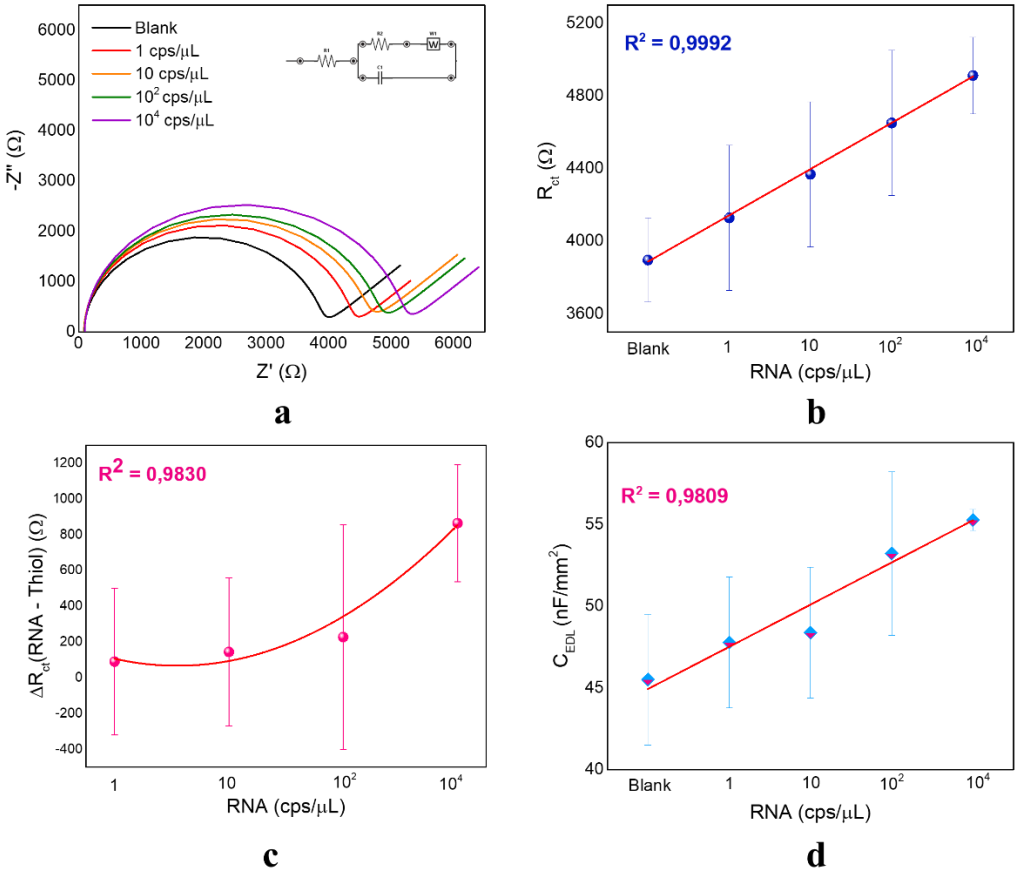

Figure 2.20. Analytical performance of ssRNA detection strategy. a) Nyquist's Plot sing different RNA concentration in the range 0–10^4 cps/µL; b) Calibration curve obtained using different RNA concentration in the range 0–10^4 cps/µL; c) Calibration curve obtained plotting ΔR_{ct} (RNA – Thiol) vs different RNA concentrations 1–10^4 cps/µL; d) Calibration curve obtained plotting C_{EDL} vs different RNA concentrations 0–10^4 cps/µL in 5 mM $[Fe(CN)_6]^{4-/3-}$ in 0.2 M Pb. The error bars in panel b,c,d are the standard deviation calculated on 4 independent electrodes for each tested RNA concentration and 3 independent electrodes for each zero-dose measurement.

Lastly, it was interesting to evaluate the capacitance of the EDL at the electrolyte-semiconductor interfaces. Indeed, also in this case, the gold electrode used as WE was "transformed" into a semiconductor material after the various functionalization. The C_{EDL} were evaluated by EIS measurements at the same frequency for all substrates. **Figure 2.20d** shows the dependence of C_{EDL} values on RNA concentration from 1 cps/µL to 10^4 cps/µL along with the zero-dose measurement (blank), which is considered a baseline

measurement. In particular, the calculated C_{EDL} values confirm the previously detected LoD and LoQ in EIS for 1 and 10 cps/µL with the values of 47.77 ± 4.7 nF/mm^2 and 48.37 ± 4.83 nF/mm^2. These results demonstrate that there is a higher charge accumulation at the electrode interface as the RNA concentration increases, thus demonstrating that more biomolecular bonds are formed[198] due to increased cooperative hybridization.

The selectivity of the new ssRNA detection strategy was evaluated by impedimetric measurements in the presence of dsDNA HBV genome at 10^4 cps/µL. The ΔR_{ct} signals obtained for this unspecific (US) genome were compared with those of the four concentrations of RNA previously illustrated. The signals ΔR_{ct} obtained (RNA - Thiol) for these solutions were compared with those for the standard solution in the absence of any interferent. The results reported in **Table 2.8** indicated high selectivity of the fabricated sensors, in fact the ΔR_{ct} values were not affected by the presence of BJ01 RNA.

Table 2.8. Difference charge transfer resistance (ΔR_{ct}) RNA-Thiol and peak-to-peak separation (ΔE) estimated for different concentrations of Sars-CoV-2 RNA and SARS Coronavirus BJ01 RNA using CV and EIS in 5 mM [Fe(CN)6]4-/3-, in Pb pH 6.8.

RNA (cps/µL)	$\Delta R_{ct}(\Omega)$	ΔE(V)
1	90 ± 400	0.30 ± 0.03
10	144 ± 400	0.29 ± 0.02
10^2	227 ± 600	0.32 ± 0.03
10^4	864 ± 300	0.34 ± 0.01

2.3. Development DNA strategy for PCR-free detection of *Pseudomonas Aeruginosa*

Pseudomonas aeruginosa is a common, opportunistic, Gram-negative bacillus that causes several clinical infections as well as serious infectious disorders[215,216]. PA is a pathogen responsible for severe infections in various body systems, including the respiratory and the urinary tracts, the vascular and the central nervous system. Furthermore, PA is one of the main causes of nosocomial infections[217]. Disorders triggered by PA can occur even at low concentrations, and this bacterium has intrinsic resistance to numerous antimicrobial agents due to its low outer membrane permeability, upregulation of multidrug efflux pump systems[218] and its virulence factor biofilm[219]. These properties make it able to tolerate numerous antibiotics with ease[220]. Thus, it is essential to treat PA infections as soon as they are screened. This led to the need of rapid, accurate, and ultrasensitive PA diagnostic solutions that could make more effective the therapeutic measurements. Conventional approaches involve techniques based on culture, biochemical assays, and microscopy. Presently employed diagnostic techniques to identify PA include culture-dependent colony counting methods like Microbial Source Tracking (MST) and faecal indicator bacteria, as well as immunodetection, PCR, and matrix-assisted laser desorption/ionization time-of-flight mass spectrometry (MALDI-TOF-MS)[221]. Although cell culture platforms are a common diagnostic method for identifying PA infections, they are laborious and time-consuming, require selective enrichment and biochemical screening, and are associated with low sensitivity, selectivity, and the risk of contamination. As a result, there is a need for more rapid, accurate, and sensitive diagnostic methods for identifying PA[222,223]. Alternative techniques are faster, sensitive, and specific than immunological methods, which need a lot of antigens. Studies suggest that Immunoblotting Test (IBT) tests based on immunohistochemistry and gel electrophoresis provide sensitivity for the early detection of PA while being less frequent[224]. Instead, advanced molecular technologies, encompassing various types of PCR, such as Real-time quantitative (q)PCR, Multiplex PCR, RT-PCR,

droplet digital PCR (ddPCR), etc., and the NAs sequencing, have become pivotal diagnostic approaches, gradually superseding conventional cell culture-based and immunological assays[224,225]. However, PCR-based methods need the NAs amplification to reliably detect the bacterium, thus, limiting the technological progress due to the need for dedicated instrumentation, thermal modules and an optical apparatus that cannot be easily integrated into portable systems. For this reason, again, PCR-free biosensors have been extensively used in the health field in recent years due to their rapidity, specificity, sensitivity, and inexpensiveness[226].

In the present section, the development of a biosensing strategy for the PCR-free molecular detection of PA is reported. Also in this case, the surfaces of a gold-sputtered silicon substrate and a commercial gold electrode have been functionalized by grafting specific thiol-modified oligonucleotides probes selective PA dsDNA and this was revealed and quantified by cooperative hybridization.

2.3.1. Experimental

Probes for the selective recognition of the PA dsDNA have been developed through a first study concerning the identification of the most significative genes belonging to the selected target. This revealed a series of candidate genes such as the acyl-homoserine-lactone synthase (lasI), the fucose-binding lectin (lecB) and the RNA polymerase D subunit (rpoD), whose annealing regions are highlighted in violet in the PA genome map reported in **Figure 2.21a**. Among these, it was chosen the housekeeping rpoD gene since highly conserved among all subspecies and strains of P. aeruginosa. For this gene, specific probes named PA_P1 and PA_P2 (green in **Figure 2.21b**) have been identified in the work of Perfumo et al. of 2013[227], and provided an optimal compromise in terms of recognition sequence size, 163 bp, and annealing conditions.

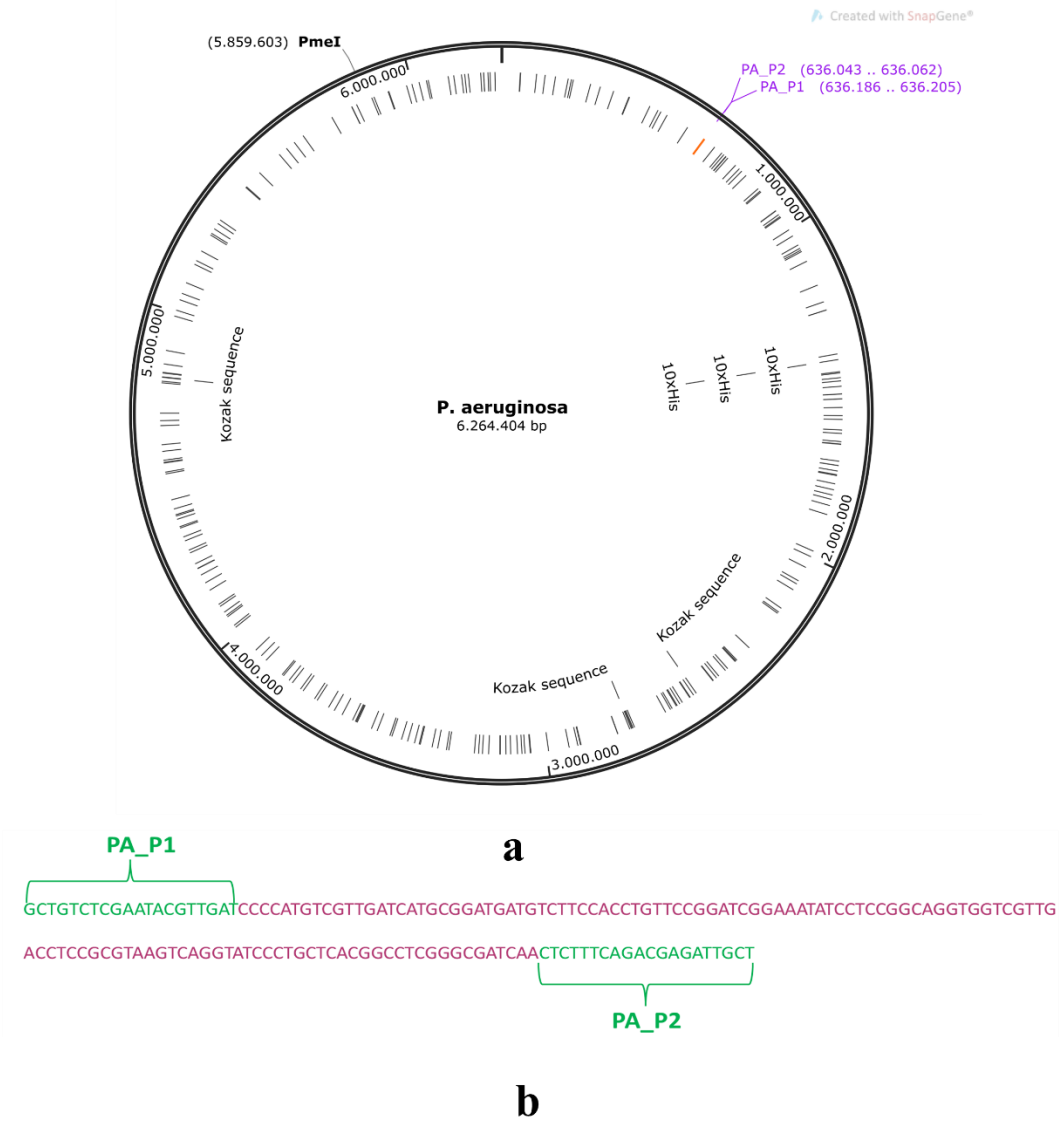

Figure 2.21. a) map of the 6 Mbp dsDNA genome of P. aeruginosa. b) PA_P1 and PA_P2 recognition sequence.

The customized thiol-modified probes (from MetaBion International AG) are described in **Table 2.10.** These were grafted onto the surface of the two use-case substrates, already described in the previous LI and SC applications, for the surface properties characterization via CA and SFE analysis and the PCR-free sensing tests via CV and EIS analysis. Also here, we performed CA analysis using four replicates of each functionalization step and electrochemical analysis using four replicates for each functionalization step,

four replicates for each tested DNA concentration and three of zero-dose measurement (blank).

Table 2.10. Use case thiol-modified probes

Probe	Sequence 5'-3'
PA_P1-T	HS-C6- AGCAATCTCGTCTGAAAGAG
PA_P2-T	HS-C6- GCTGTCTCGAATACGTTGAT

For the target preparation, the dsDNA genome of PA was isolated from a commercial strain (ATCC) with a concentration of 10^6 copies/µL and, then, diluted in DNAse and RNAse-free water to the final working concentration, from 10^4 to 10^{-1} copies/µL.

2.3.1.1. Gold-sputtered silicon substrate functionalization

Gold-sputtered silicon substrate of 0.55 cm x 1 cm functionalization with PA probes and dsDNA target, schemed in **Figure 2.22,** was performed according to the following chemical protocol reported in section 2.1.1.1 and 2.1.2.1. for LI kDNA and SC ssRNA.

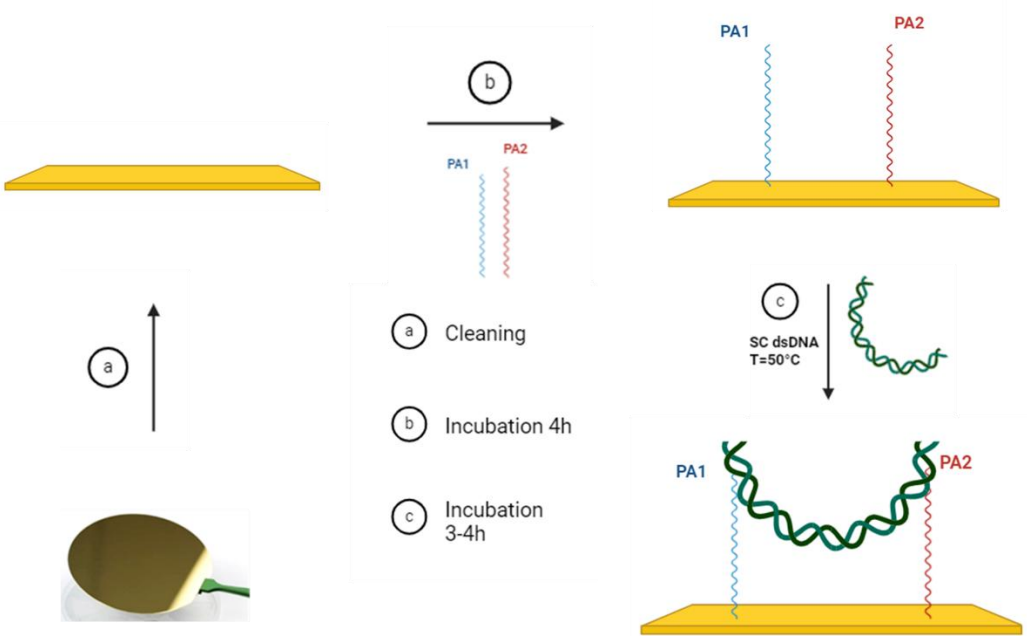

Figure 2.22. Gold substrate preparation, a) Surface cleaning with basic piranha solution; b) Immobilization of specific probes PA_1 and $PA_2$and c) recognition of PA dsDNA by surface cooperative hybridization.

For the not amplified genetic target hybridization, PA dsDNA was diluted to 10^4 copies/µL in PBS at pH 5.5. The gold interface functionalized with PA_1/PA_2 probes was dipped in dsDNA solution at 50 °C for 3.5 h. Then, the unbound dsDNA was washed away from surface by PBS buffer.

2.3.1.2. Commercial gold electrode functionalization

Commercial CHI101 gold electrodes were modified according to the functionalization protocol schemed in **Figure 2.23** in according to what described previously in sections 2.2.1.2. and 2.1.2.1. for LI kDNA and SC ssRNA.

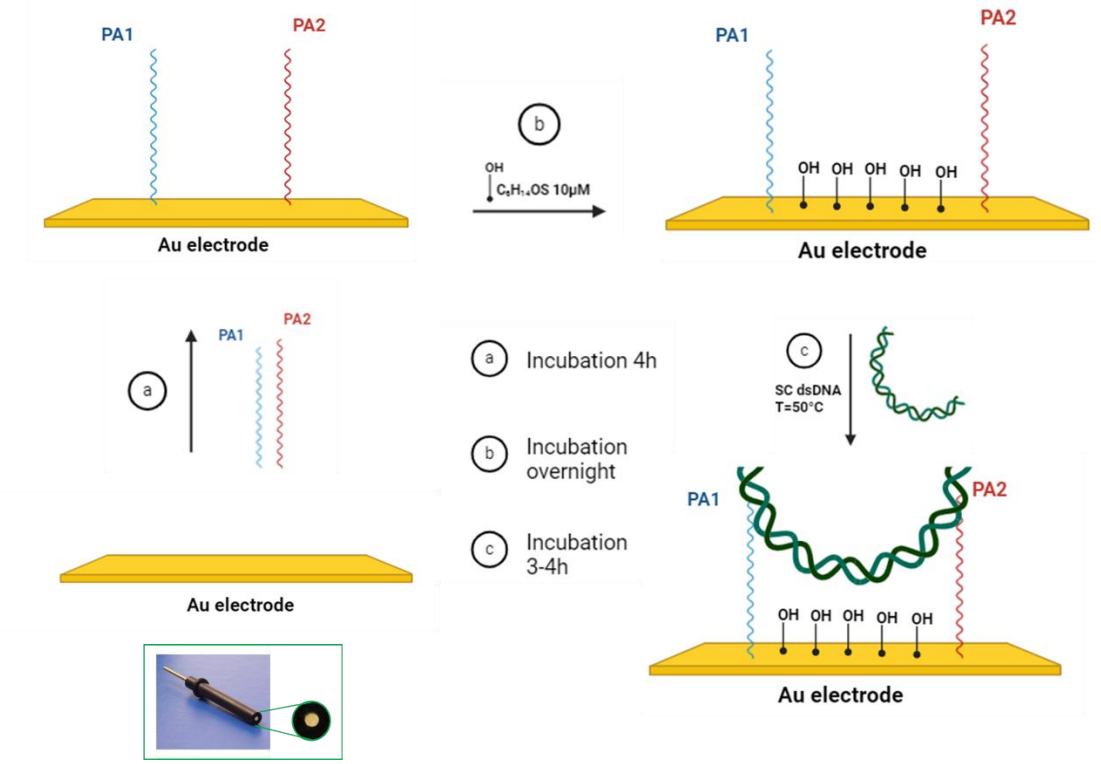

Figure 2.23. Electrode gold surface preparation; a) Immobilization of specific probes PA_1 and PA_2 and of b) 6-Mercapto-1-hexanol on the surface of a gold electrode; c) recognition of PA dsDNA by surface cooperative hybridization.

For the not amplified target hybridization, the extracted PA dsDNA was used at the concentration of 1, 10, 10^2 and 10^4 copies/µL in PBS at pH 5.5. The final gold interface was dipped in PA dsDNA solution at 50 °C for 3.5 h. Then, the unbound dsDNA was washed away from surface by PBS buffer.

2.3.2. Surface characterization analysis and sensing tests

As already mentioned in the previous paragraphs, the surface properties of PA dsDNA interface was characterized in two task: 1) *sensing surface chemical-physical characterization*; 2) *PCR-free sensing of SC dsDNA by electrochemical analysis*.

Also in this case, the wettability and isoelectric properties of the functionalized sensing surface were evaluated by CA and SFE analysis. For the measurements, a drop of 1 µL of ultrapure water was spotted on top of the gold

substrate and the CA of drop was acquired after 10s. The analysis was performed on a clean gold substrate, used as reference, and substrates functionalized with probes and probes-target interfaces. All contact angle values, measured in four replicas (n = 4). The SFE was done as described before for LI kDNA and SC ssRNA.

The second task related to the dsDNA PCR-free detection was done electrochemically by CV and EIS analysis. The measurements were performed using the same procedure as that already used for LI kDNA and SC ssRNA .

2.3.3. Results and discussion

2.3.3.1. Sensing surface chemical-physical characterization

The CA characterization of step-by-step functionalized gold interface is shown in **Figure 2.24**. The corresponding CA measures are plotted in **Figure 2.24a**. Data highlight a marked increase of wettability after the Au cleaning step, passing from 80.76° ± 1.03° to 51.93° ± 3.34° of CA, that could be related to the formation of the thin hydroxyl layer on the gold surface. After the grafting of oligonucleotide probes the wettability increased again, as proved by the relevant decrease in CA of ~8° reported in **Figure 2.24a**. The reason of this trend was due to the addition of charges to the gold surface, brought by the hydroxyl, amino and phosphate groups of the oligonucleotide chains that led to a higher number of electrostatic interactions between the water drop and the surface.

The functionalized interface was, then, treated with 10^4 copies/µL of the DNA target. The cooperative hybridization was performed according to a previous work of PCR-free detection of Hepatitis-B Virus genome.[47] As shown in **Figure 2.24a**, CA analysis after the step of DNA hybridization proved that the interface almost maintained the high hydrophilicity and wettability, reporting a value of 32.3° ± 1°. This slight increase of CA value, compared to that measured on interface with probes only, could be due to the molecular recognition.[185] Indeed, the binding between oligo and target chains causes a partial shielding

of the charges exposed by functional group of single strand probes affecting the interface polarity.

To support our hypotheses, SFE analysis was performed on DNA-gold interface before and after the DNA hybridization. The results for the interface exposing probes only, described in **Figure 2.24b-PA probes**, reported a high SFE value of 59.89° ± 5.9 mN/m with a predominant polar part at 36.85 ± 4.9 mN/m, due to the addition of oligonucleotides charges. The analysis after the DNA hybridization, in **Figure 2.24b-PA probes-DNA**, showed an SFE value of 62.2 ± 6.2 mN/m that proved the surface wettability was kept after the cooperative hybridization. However, a higher value of the polar part at 37.55mN/m ± 3.7mN/m was also observed, clearly proving the double helix formation and the charges shielding effect as consequence of probe-target hybridization.

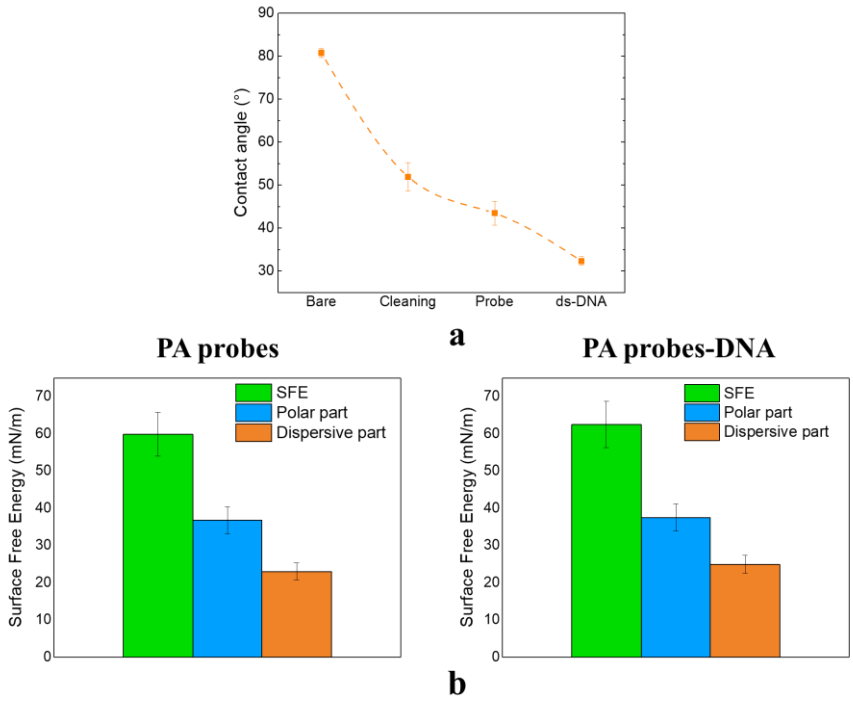

Figure 2.24. a) step-by-step CA characterization of functionalized interface; b) SFE analysis on DNA-gold functionalized interface before (PA probes) and after (PA probes-DNA) the DNA hybridization.

The isoelectric properties and PZC of PA probes and PA probes-dsDNA interfaces have been analyzed through CA measurements at various pHs and results are reported in **Figure 2.25**. Actually, in the aqueous environment of the studied DNA-gold interfaces the equilibrium can be easily altered by changing the pH and the surface hydrophilicity[186] since the anchored biomolecules can be both positively and/or negatively charged with respect to their isoelectric properties and the point of zero charge (PZC).[187–189]

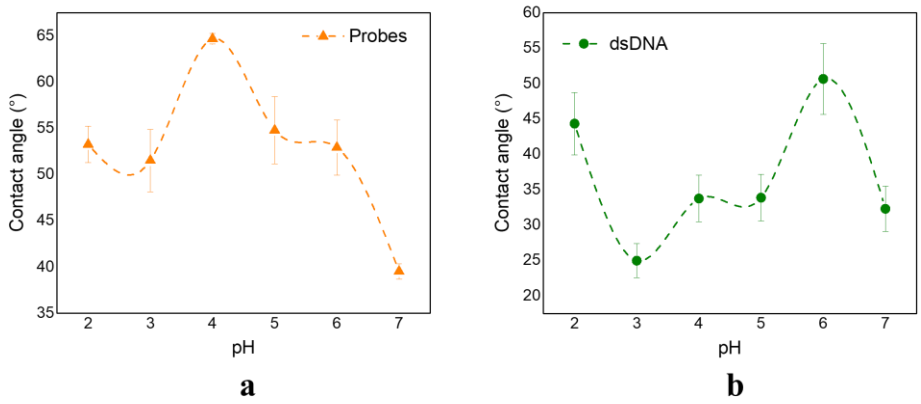

Figure 2.25. CA analysis of PA probes (a) and PA probes-target interface (b) at various pHs.

CA measured on the interface modified with PA probes, **Figure 2.25a**, reached a maximum of 64.69° ± 0.57° at pH 4, considered as possible PZC value, and decreased at other pHs. This trend could be explained as the consequence of the ionization of DNA amino, hydroxyl and phosphate groups when the pH is away from their PZC causing the increase of interface hydrophilicity and surface wettability.

In the case of interface with PA probes and DNA, **Figure 2.25b**, the average contact angles highlighted a maximum of 50.66° ± 5° around pH 6 and, again, decrease at pHs that were different from the PZC, as also observed for kDNA LI. A slight increase, however, was observed also at pH 2, probably, since the DNA molecule at that pH tends to denature and alter its isoelectric profile.

2.3.3.2. PCR-free sensing of LI kDNA by electrochemical analysis

The CV and EIS results are shown in **Figure 2.26a and 2.26b**, respectively. In particular, the frequency response from the EIS measurements were fitted to the Randles equivalent circuit (**Figure 2.5**), from which the charge transfer resistance, R_{ct}, was extracted.

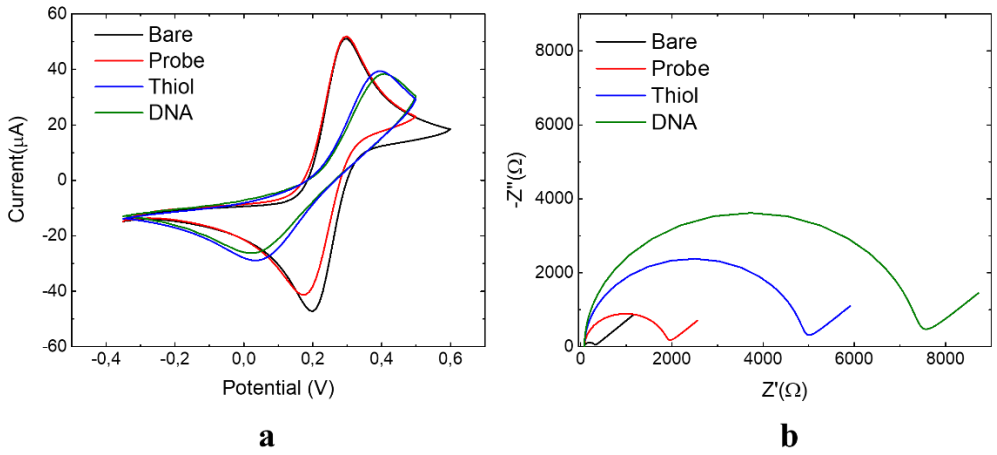

Figure 2.26. Electrochemical characterization of Au electrode interfaces during the multistep biosensor build-up using a *Pseudomonas Aeruginosa* dsDNA concentration of 10^4 cps/μL. a) Cyclic voltammograms and b) Nyquist's Plot recorded in 5 mM $[Fe(CN)_6]^{3-/4-}$ in 10mM PBS.

The voltammograms depicted in **Figure 2.26a**, reveal the effects of different chemical and biological layers on the electrical conductivity and resistivity of the electrode/electrolyte interface, influencing the performance of the WE. In particular, the cooperative hybridization between probe and dsDNA produced a significant decrease in the magnitude of both voltametric peaks, reported respectively as anodic and cathodic current peaks. This was due to a drastic decrease in the diffusivity of the redox probe near the WE interface, resulting from the sequential immobilization on the electrode surface of probe, thiol and the final addition of the PA dsDNA. Similarly, Nyquist plots showed an increase in the total impedance of the system (bare-DNA) indicating that greater coverage of the electrode surface leads to a slower electron transfer rate and

greater resistance to charge transfer compared to the platform naked. These phenomena were attributable to the coating layer of the electrode surface, which became thicker with the assembly procedure, thus reducing the permeability $[Fe(CN)_6]^{3-/4-}$ through the immobilization of the layers.

Steps that have been investigated in the punctual electrochemical characterization of surface modification effects, whose EIS values are resumed in **Table 2.11**, are reported below.

Bare-Au: in this case both species (Fe^{2+} and Fe^{3+}) rapidly exchange electrons with the working electrode and the peak-to-peak separation is lower than 59 mV/e^- (**Figure 2.26a**, black line). In line, the Nyquist plot (**Figure 2.26b**, black line) shows a smaller semicircle domain in comparison with the modified gold surfaces, indicating a small charge transfer resistance (R_{ct}), meaning a small resistance encountered by the electron as it travels between the redox species and electrode surface. Low R_{ct} values (132Ω) indicate a more electrochemically active surface[192].

Probes anchoring: the voltammograms reported in **Figure 2.26a** (red line), showed a little increase in the magnitude of the voltametric peaks and an important increase in the peak-peak separation (ΔE = 0.110 ± 0.0001V) compared to bare-Au. This can be attributed to the shielding characteristic of the grafted probes layer, which gradually hinders the transport of electrons on the surface of the gold electrode[193]. The EIS analysis showed an increase of the total impedance passing from the Au-bare (R_{ct} = 132Ω) to electrode functionalized with probes[228] (**Figure 2.26b** red line). This effect was due to the chemical properties of the probes which prevent for the most part of Faradaic currents from penetrating to the surface (due to the high insulating properties of the thiol)[194]. Indeed, the reaction rate of the iron/ferricyanide couple for this step becomes gradually slower than the previous one.

Passivation: blue line in **Figure 2.26a** showed a significant increase in the magnitude of the voltammetric peaks for the passivating molecule and an important increase in the peak-peak separation (ΔE = 0.303 ± 0.005V) compared to bare-probes. This was attributed to the highly shielding

characteristic of the grafted organic layer, which gradually hindered the transport of electrons on the surface of the gold electrode. Also in this case, the EIS analysis supported the data, reporting an increase of total impedance after the electrode passivation (**Figure 2.26b,** blue line). This effect was due to the chemical properties of the passivating which prevent almost all Faradaic currents from penetrating to the surface (due to the high insulating properties of the thiol)[195]. Indeed, the reaction rate of the iron/ferricyanide couple for this step becomes gradually slower than the previous one, as shown by the increased peak-to-peak separation (form of reversible voltammograms).

Table 2.11. Charge transfer resistance (R_{ct}), peak-to-peak separation, anodic and cathodic peak ratio (I_{pa}/I_{pc}), estimated for CHI101 using CV and EIS in 5 mM $[Fe(CN)_6]^{4-/3-}$, in Pb pH 6.8, during genetic-PA-PoC fabrication. Average values of at least 3 Au electrodes are presented.

DNA (cps/µL)	R_{ct} (Ω)	ΔE (V)	I_{pa}/I_{pc} (µA)
Bare	132 ± 17	0.1 ± 0.01	1.04 ± 0.02
Probes	1341 ± 300	0.110 ± 0.001	1.12 ± 0.01
Thiol	4589 ± 40	0.303 ± 0.005	10.81 ± 0.20
RNA 10^4	7100 ± 700	0.323 ± 0.020	6.12 ± 1.10

PA DNA hybridization: in **Figure 2.26a** (green line) it is possible to observe a further slight increase in the magnitude of the voltametric peaks for dsDNA target and therefore an increase in peak-peak separation (ΔE = 0,323 ± 0,02V) compared to the probes and thiol grafted onto the WE surface. This was related to the cooperative hybridization effect and the material genetic inclusion in the dielectric composition, and demonstrate the ability of this sensing strategy to directly reveal the PA dsDNA without further amplification[213]. The EIS analysis, in **Figure 2.26b** (green line), reported a clear increase of impedance from Au-probe-thiol to dsDNA-hybridized electrode. The diameter of the semicircles in the Nyquist plots increased with the addition of the PA DNA used to a R_{ct} =7100Ω ± 710Ω. This effect was due

to the chemical properties of DNA that prevent almost all Faradaic currents from penetrating to the surface (due to the high insulating properties of the thiol).

The analytical performance of the detection strategy was tested with different PA dsDNA concentrations ranging from 0 to 10^4 cps/µL, as reported in **Figure 2.27**. The Nyquist plots recorded after hybridization shows an increase of the total impedance R_{ct} in a concentration-dependent manner. The reproducibility of the response was investigated testing four concentrations of DNA with three equally prepared electrodes, and a relative standard deviation for each concentration used was calculated (**Table 2.12**). The goodness of the correct functioning of the biosensor was then obtained by plotting on the x-axis the four types of DNA concentration versus ΔR

ct. ΔR_{ct} was calculated by the following equation (5):

$$\Delta R_{ct} = R_{DNA} - R_{p-t} (5)$$

Where R_{p-t} is the value of charge transfer resistance value when probe and passivator are immobilized on the electrode surface and R_{DNA} is the charge transfer resistance value after the cooperative hybridization with DNA is established. The dependence of ΔR_{ct} values on dsDNA concentration is shown in **Figure 2.27c**. In particular, the LOD and LOQ values were 1 and 10 cps/uL respectively with values of 382 ± 614Ω and 556 ± 631Ω, leading to hypothesize a possible application of the developed genosensor to real biologic samples.

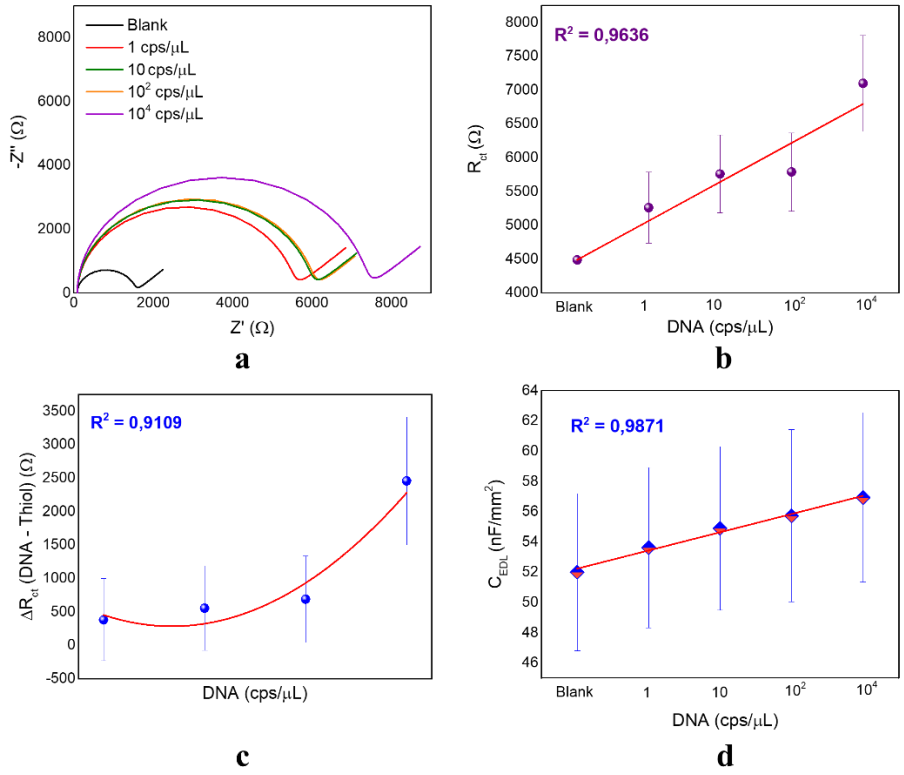

Figure 2.27. Analytical performance of dsDNA detection strategy . a) Nyquist's Plot sing different DNA concentration in the range 0–10^4 cps/µL; b) Calibration curve obtained using different DNA concentration in the range 0–10^4 cps/µL; c) Calibration curve obtained plotting ΔR_{ct} (DNA – Thiol) vs different DNA concentrations 1–10^4 cps/µL; d) Calibration curve obtained plotting C_{EDL} vs different DNA concentrations 0–10^4 cps/µL in 5 mM $[Fe(CN)_6]^{4-/3-}$ in 0.2 M Pb. The error bars in panel b,c,d are the standard deviation calculated on 4 independent electrodes for each tested DNA concentration and 3 independent electrodes for each zero-dose measurement.

The different C_{EDL} were evaluated by EIS measurements at the same frequency for all substrates. **Figure 2.27d** shows the dependence of C_{EDL} values on DNA concentration from 1 cps/uL to 10^4 cps/uL along with the zero dose measurement (blank), which is considered a baseline measurement. In particular, the calculated C_{EDL} values confirm the previously detected LOD and LOQ in EIS for 1 and 10 cps/uL with the values of 53.63 ± 5.3 nF/mm^2 and 54.9 ± 5.4 nF/mm^2. These results demonstrate that there is a higher charge accumulation at the electrode interface as the DNA concentration increases,

thus demonstrating that more biomolecular bonds are formed[198] due to increased cooperative hybridization.

Table 2.12. Charge transfer resistance (R_{ct}), peak-to-peak separation (ΔE) and Capacitance EDL (C_{EDL}) estimated for different concentrations of *Pseudomonas Aeruginosa* dsDNA using CV and EIS in 5 mM $[Fe(CN)_6]^{4-/3-}$, in Pb pH 6.8.

DNA (cps/µL)	R_{ct} (Ω)	ΔE(V)	C_{EDL}(nF/mm²)
0	3896 ± 200	0.29 ± 0.02	52.0 ± 5.2
1	4127 ± 400	0.29 ± 0.03	53.7 ± 5.3
10	4367 ± 400	0.30 ± 0.02	54.9 ± 5.4
10^2	4650 ± 400	0.31 ± 0.03	55.8 ± 5.5
10^4	7100 ± 700	0.32 ± 0.02	56.9 ± 5.6

The selectivity of the fabricated genetic-PA-PoC was evaluated by impedimetric measurements in the presence of HBV dsDNA 10^4 cps/uL. The ΔR_{ct} signals obtained for this unspecific target were compared with those of the four concentrations of DNA previously illustrated. The results reported in **Table 2.13** indicated high selectivity of the fabricated sensors, in fact the ΔR_{ct} values were not affected by the presence of US dsDNA.

Table 2.13. Difference charge transfer resistance (ΔR_{ct}) DNA-Thiol and peak-to-peak separation (ΔE) estimated for different concentrations of Sars-CoV-2 RNA and US Hepatitis b virus DNA using CV and EIS in 5 mM [Fe(CN)6]4-/3-, in Pb pH 6.8.

DNA (cps/µL)	ΔR_{ct}(Ω)	ΔE(V)
1	382 ± 600	0.29 ± 0.03
10	556 ± 600	0.30 ± 0.02
10^2	690 ± 600	0.31 ± 0.03
10^4	2458 ± 900	0.32 ± 0.02

2.4. Probe-phage based biosensors

This part of the research was focused on the design of a biosensor for pathogens detection based on probe phage in PoC format.

Conventional culture-based methods for detection of bacteria in different kinds of sample are time consuming requiring further confirmation by biochemical assay or PCR. As an alternative, several biosensors have been proposed for detection of pathogens in biological samples. Among them magnetic beads have assumed considerable importance due to their greater surface/volume ratio compared to a flat surface. There are a lot of works reporting the use of magnetic particles for identification of viruses and bacteria in food, water, environmental or biological samples[229–231]. However, most of them used antibodies as sensing element that are very sensitive to environmental physicochemical variations such as pH, temperature, presence of organic solvents, as well as to mechanical stresses. Moreover, their large-scale production and purification are expensive, time-consuming and mostly not reusable. M13 phages[232,233], if opportunely engineered, can be very selective toward specific targets and used as a valid substitute for antibodies or peptides overcoming most of their limitations. Indeed, phages are robust, stable and resistant to temperature variations and hard pH conditions. In addition, their propagation on host bacteria cells is cheaper compared to both antibodies and peptides production and they can be used multiple times even after treatment with urea or high temperatures.

In this activity I worked on the design and characterization of a probe phage-based biosensor for the pathogen detection for possible implementation in PoC format.

The steps of the biosensing strategy, as schemed in **Figure 2.28**, were first defined as follows: (a) probe phages anchoring on magnetic beads surface, that should be performed via covalent immobilization of phage capsids; (b) derivatized beads exposure to whole pathogen targets for the phage recognition and capture; (c) beads separation and washing steps, that should

imply effective buffers and temperatures to remove unbound biomolecules and starting sample dendrites; (d) final detection of target capture, achievable via different optical, electrical or electrochemical methods. This detection should be carried out directly on top of the phages-derivatized beads into a plastic ELISA plate.

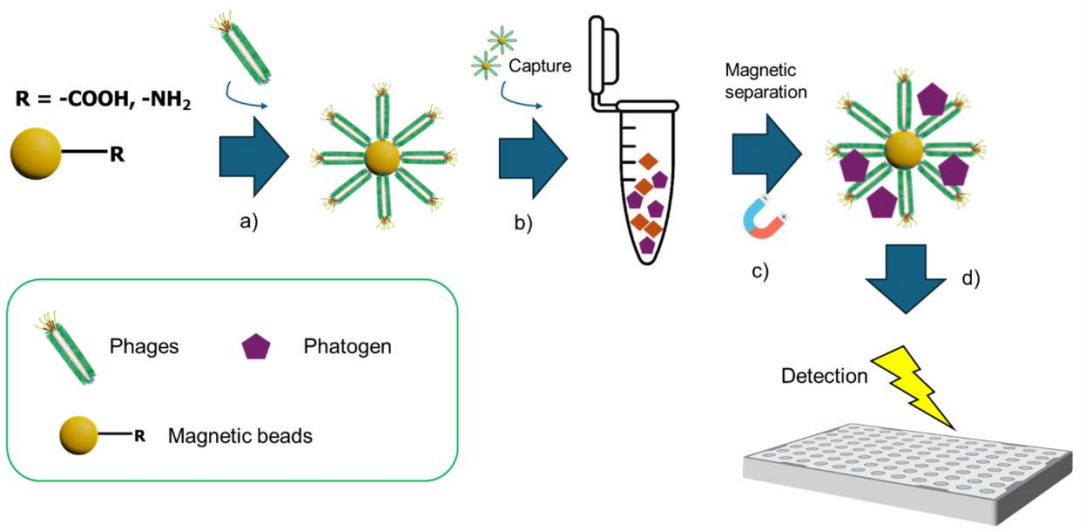

Figure 2.28. General steps of probe phage-based biosensing strategy: (a) M13 phages anchoring on beads; (b) pathogen capture; (c) magnetic beads separation and washing; (d) final detection on ELISA plate.

Subsequently, the rough specifications of a possible architecture of the POC devices were designed, schemed in **Figure 2.29**. This integrates: the inlet of pathogen sample (A); the inlet of probe phages-derivatized beads (B); a microfluidic system composed of 4 chambers for the washing buffers and additional co-reactants inlet (C) and 4 chambers for washing wastes outlet (E), including also a resistor on the back side for the thermal management during washing steps; a capture channel (D) for the beads exposure and capture of pathogen; the outlet of sample dendrites and unbound pathogens (F); the optical/electrical detection chamber (G). To accurately manage fluids movements, specific systems such as micropumps and micromixers can either be embedded inside the microfluidic device.

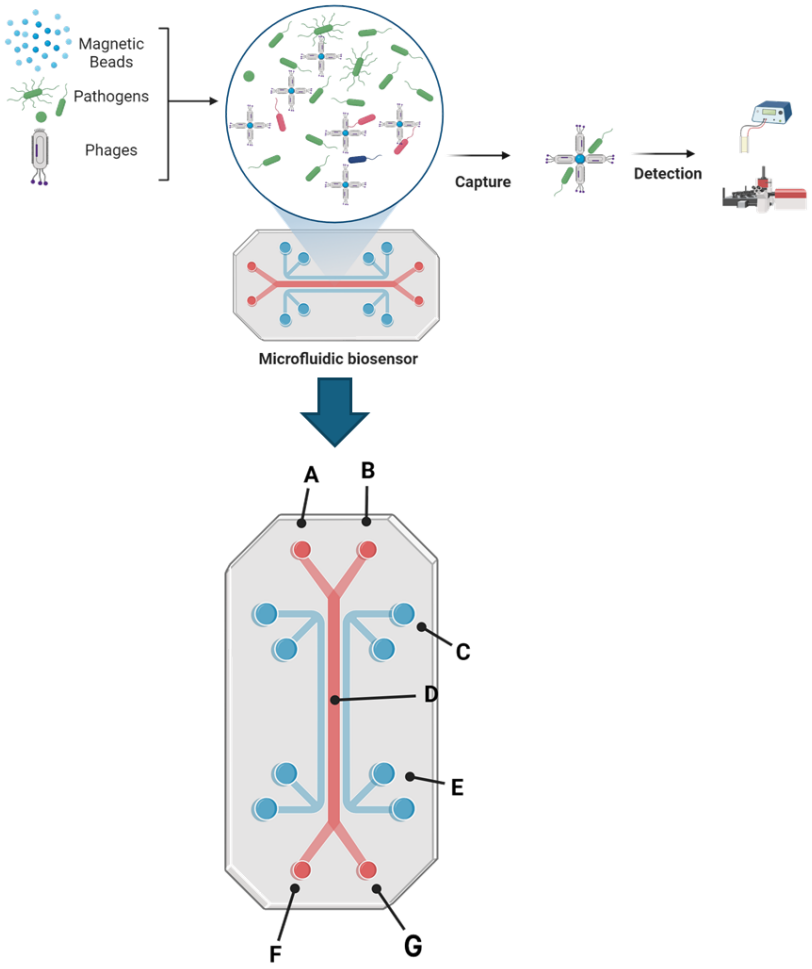

Figure 2.29. Scheme of rough specifications of probe phage-based biosensor: (A) sample inlet; (B) probe phage-beads inlet; (C,E) microfluidics network; (D) capture channel; (F) sample outlet; (G) detection chamber.

In order to develop a possible prototype of a sensor based on phage probes, the following activities were, then, performed: (1) preparation of a probe phage-based sensing interface derivatized inside the plastic well of an ELISA 96-well plate and preliminary optical (colorimetric) characterization of the biosensor interface assembly; (2) characterization via wettability assay of plastic surfaces derivatized with probe phages already decorated with nanomarkers, which could be used in a possible implementation of the detection system.

The first activity (1) was performed by anchoring 200 µL of M13 phages at concentrations from 10^7 to 10^{11} cps/µL inside the wells of an ELISA plate. Then,

wells were washed 3 times with washing buffer (PBS + 0.05% Tween 20). Lastly, 250 µl of monoclonal PVIII-HRP conjugate of the main anti-M13 coat protein (1:7500 diluted in PBS + 0.1% BSA + 0.5% Tween 20) were added. After 1 hour of incubation at 37°C, reactions were developed with 250 µl of 3,3',5,5'-TetraMethylBenzidine (TMB), Horse Radish Peroxidase (HRP) substrate, for 20 minutes in the dark, stopped with H_2SO_4 0.6N and read at 450 nm, **Figure 2.30.**

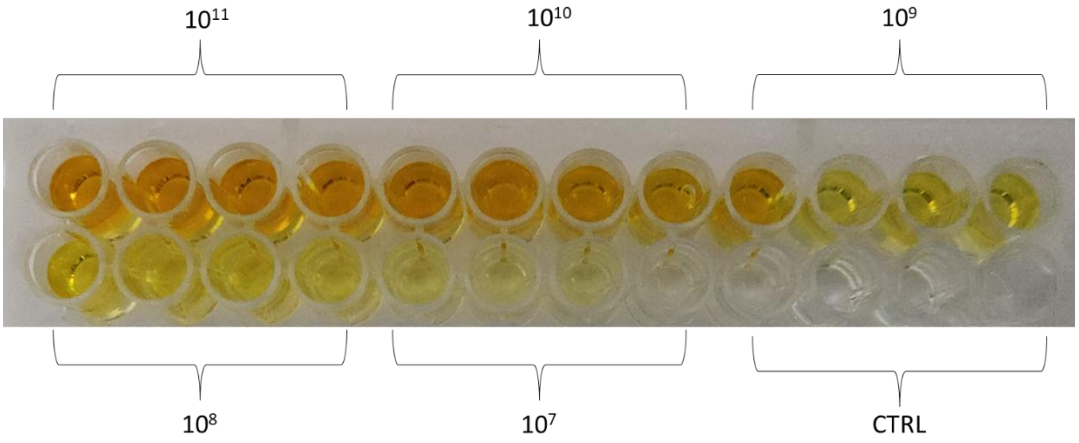

Figure 2.30. ELISA test for preliminary characterization of the probe phages interface assembly. There are four negative control and five positive tests (in yellow) at different concentrations of beads-M13phages from 10^7 to 10^{11} cps/µL.

As shown in **Figure 2.30**, the presence of M13 phages was validated through the colorimetric reaction developed with anti-M13 antibodies. From the results, the coloration is much more intense with the increase in the concentration of anchored phages in the wells, achieving absorbance values of 1.541 ± 0.01 for 10^{11} cps/µL. The data showed a good tendency in discriminating the different concentrations reaching values of 0.165 ± 0.001 for the lowest concentration, thus highlighting the possibility of integrating this strategy with appropriate engineered phages for the capture of pathogens.

Furthermore, the surface properties of assembled probe phage-based interface were assayed by surface wettability characterization (2). The analysis, reported in **Figure 2.31,** showed an increase of the surface wettability after its derivatization with probe phages (**Figure 2.31b)**, as proved by the

reduction in drop curvature compared to the no functionalized surface (**Figure 2.31a**). This was due to the charged of numerous functional groups exposed on the phage capsid, which cause a significant increase of surface polarity together with the wettability.

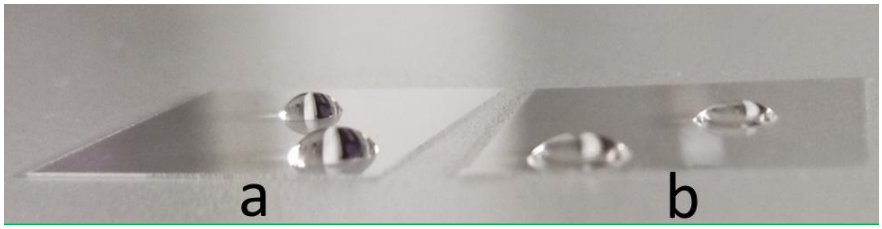

Figure 2.31. Wettability evaluation of a surface before (a) and after (b) probe phages immobilization.

The above data, which were preliminary for the development of a possible biosensor based on phage probes.

2.5. Future perspectives

In this chapter, we discussed the construction of new detection methods for the diagnosis of infectious diseases through the construction of biointerfaces using the cooperative hybridization mechanism. In order to improve the implementation of this technology for PoC applications, future perspectives will be devoted to the integration into portable and easy-to-use devices. In this sense, we considered to integrate biointerfaces into printed circuit sensors, **Figure 2.28a**, which include three screen-printed gold WE, Ag/AgCl RE and Pt CE. This technological advancement will allow to obtain flexible, easy-to-use devices with low-cost production and the possibility of decentralized PoC applications[234–236].

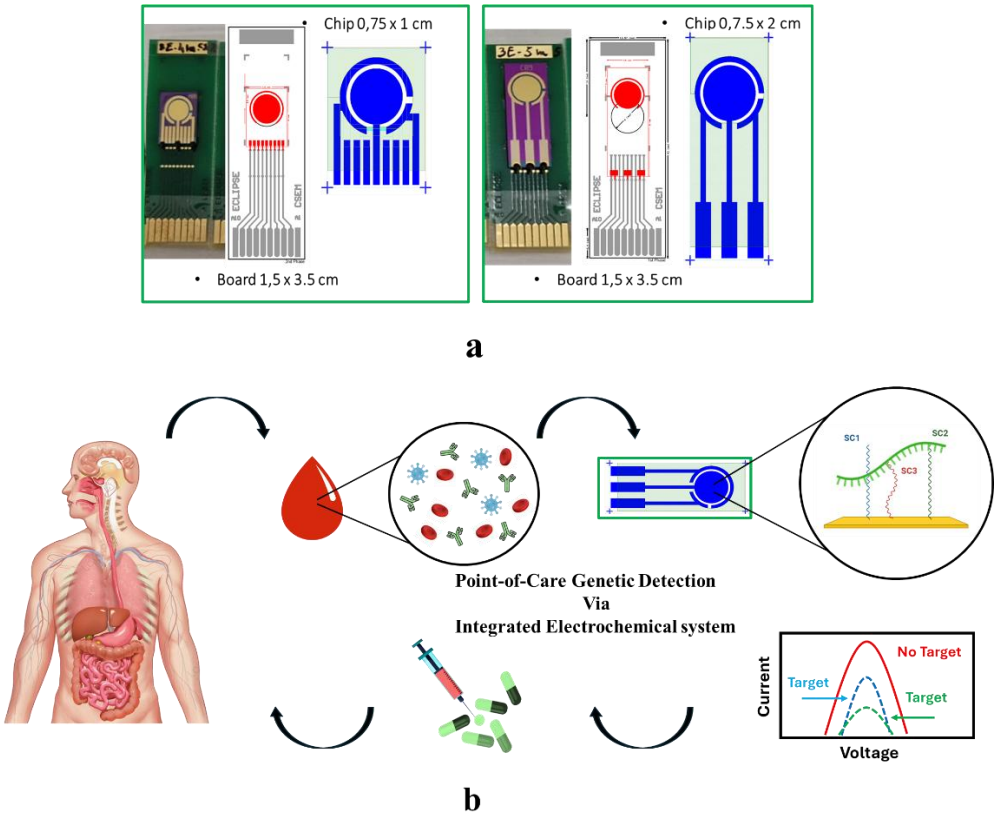

Figure 2.28. Advances in the diagnosis of infectious diseases. (a) New Electrochemical Sensors for PoC Applications, (b) PoC Strategy Through New Integrated Electrochemical Systems

The commercialization and broad applicability of integrated electrochemical biosensors will require coordinated efforts in improving sensing techniques and flexible materials, and in consolidating electronics, wireless electronics, data processing and data mining. Moreover, the integration of these biosensors with IoT (Internet of things) would, also, introduce the possibility to automatically transmit data by wireless network modalities (e.g., cellular data service, Wi-Fi, Bluetooth) for a cloud heath database[237–239] making massive and realt-time the pandemic monitoring and containment.

CHAPTER 3

Biosensing methods for the detection of Alzheimer's disease associated biomarkers

3. State-of-the-art on clinically oriented biosensor for AD

Biosensors have been widely explored in various biomedical applications, mostly focused on the human neurodegenerative diseases[240,241]. Alzheimer's disease (AD), is one of the most severe disorder accounting for 60–70% of total dementia cases worldwide[242,243]. The onset of AD is related to a series of molecular events, consisting in the amyloid-β (Aβ) peptides accumulation inside neurons and the subsequent plaques formation, and the tau protein phosphorylation and loss of function, vascular damage, synapse loss, damaged neuronal cells, etc.[244,245]. So far, two mains approach have been used for the diagnosis and treatment of AD. The first is based on the use of chemotherapy drugs and highly expensive pratiques with invasive sampling procedures of biological fluids (blood or cerebrospinal fluid). The second approach, instead, concerns the biosensing of biomarkers for their early detection and monitoring. In this context, PoC diagnostics[241,246–248,249,250]. has been widely applied in AD diagnostics.[251–253]. Presently, the main development is now directed towards a PoC device that is testable at the time and place of patient care, suitable for self-testing and compliant with PoC guidelines. Recently, several biomarkers have been chosen for the development of biosensors such as amyloid, tau, apolipoprotein E4 (ApoE4) gene, α-synuclein, α-1 antitrypsin, acetylcholine, miRNA, etc.[254,255], most of which are known to accumulate in cerebrospinal fluid and neuroimaging specimens[256].

In this chapter, the design and development of two new sensing strategies for the AD diagnosis in a PoC format are exposed. The first strategy, is an innovative silicon-based sensing technology capable of detecting Aβ auto-antibodies (immunoglobulin G or IgG) as biomarkers in human sera using engineered M13 phages as AD-probe-phage (ADPPs) sensing element. This strategy is based on the diagnostic power of phages[257] and “Aβ-autoantibodies” antibody markers against Alzheimer’s syndrome[258,259].

In fact, a positive association has been observed between the amount of Aβ autoantibodies in the serum of AD patients and the disease status[260,261].

In this perspective, in literature, the feasibility of this approach was demonstrated using two methods. The first, in order to evaluate whether IgG serum levels against engineered M13 phage clone were able to discriminate the immune response between AD patients and healthy subjects[259], this clone was tested in ELISA assay against a pool of five human sera from AD subjects and a pool of five human sera from healthy individuals (CTR). Results obtained showed a mean OD_{450} value of 1.266 against AD sera and a mean of 0.464 against healthy sera (*p*-value < 0.0001, one-way ANOVA test), demonstrating the presence of serum IgG levels toward the displayed peptide that were significantly higher in AD patients.

The second, to quantify the number of phages bound[258], which indirectly reflects the amount of Aβ autoantibodies present in sera, the authors we lysed five different phages and quantified their DNA through PCR in a single-step process performed on a silicon chip. The phagic weight was significantly different as indicated by one-way analysis of variance (ANOVA, $p < 0.0001$ for all five phages) and that phages only bind to this class of immunoglobulins. Furthermore, Post hoc analyses with Bonferroni's correction indicated that two phages clone significantly discriminated between non-AD and severe and between mild-to-moderate and severe ($p < 0.0001$ for all comparisons).

Therefore, the applicative potential of these markers in a rapid PCR-free diagnostic approach has been demonstrated using a detection technology compatible with PoCs.

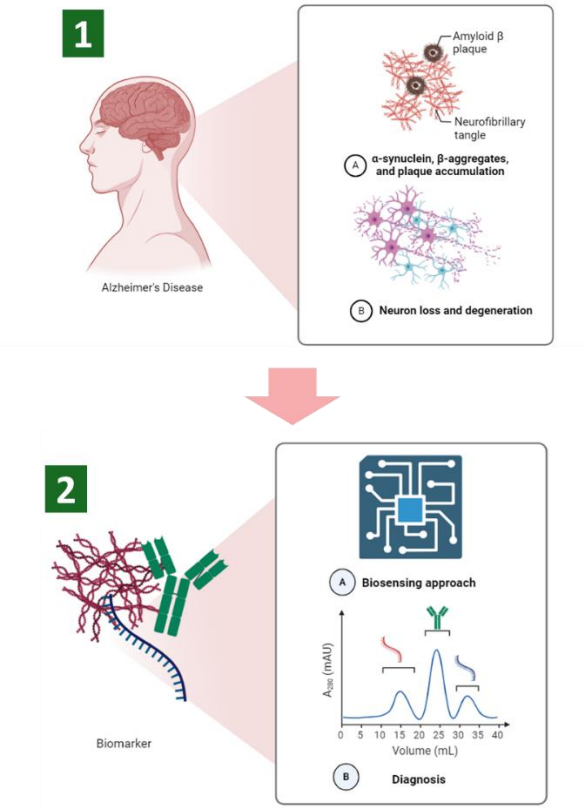

Figure 3.1. Alzheimer's disease physiological effects and approaches for rapid diagnosis. 1. Formation of amyloid plaques and fibrillary tangles (a), loss and degeneration of neurons (b). 2. (a) Biosensing approach for rapid and low-cost screening through AD biomarkers. (b) AD biomarker results after screening.

The second detection strategy is based on the molecular detection of AD associated miRNA as biomarkers via an electrochemical PCR-free sensing. Even in the case of miRNAs, the diagnostic power against AD is already known, as reported by various studies in the literature on miRNA circulating markers of the disease[262–264]. For example, the possibility of diagnosing AD through miRNAs has been used in several detection strategies showing a linear response in the range of tenths of μg mL −1 and a LOD of 20–300 nM[265,266].

Recently, Pereira et al. described a novel PoC for miRNA-34a with good target affinity, reflected on a 100 pM to 1 μM linearity range and a limit of detection (LOD) of 39 pM in buffer and 94 aM in serum[267]. With these premises, for some of these miRNAs the feasibility of a PCR-free approach has been demonstrated using technology compatible with PoCs through preliminary qualitative and quantitative assays.

3.1. Silicon-based sensing for Alzheimer's disease diagnosis by phages probes

Nowadays, research efforts have been focused on the development of alternative non-invasive sensing methods for the AD screening, particularly at an early stage. Among these, the lossy mode resonance (LMR) technology implemented in D-shaped single-mode fibers (reporting high sensitivities and detection limit), the surface plasmon resonance[268,269] (SPR), the localized SPR[270,271], the electrochemical[272,273] and immunological methods have been widely explored. In particular, immunological methods are often applied in diagnostics in rapid tests that are based on the enzyme-linked immunosorbent assay (ELISA). This method exploits the binding affinity and the solid-state interaction between antibodies and antigens through a molecular sandwich as sensing interface. Among the immunological methods using ELISA tests the phage display technology is gaining a growing interest.Nowadays, research efforts have been focused on the development of alternative non-invasive sensing methods for the AD screening, particularly at an early stage. Among these, the lossy mode resonance (LMR) technology implemented in D-shaped single-mode fibers (reporting high sensitivities and detection limit), the surface plasmon resonance[268,269] (SPR), the localized SPR[270,271], the electrochemical[272,273] and immunological methods have been widely explored. In particular, immunological methods are often applied in diagnostics in rapid tests that are based on the enzyme-linked immunosorbent assay (ELISA). This method exploits the binding affinity and the solid-state interaction between antibodies and antigens through a molecular sandwich as sensing interface.

Among the immunological methods using ELISA tests the phage display technology is gaining a growing interest.

Bacteriophages (or phages) are viruses that infect and replicate inside bacteria. Phages, particularly M13 single-stranded ones, display proteins on their capsid (pVIII and pIII)[233,274] that are able to selectively bind and identify a target biomolecule having implications in a series of human syndromesBacteriophages (or phages) are viruses that infect and replicate inside bacteria. Phages, particularly M13 single-stranded ones, display proteins on their capsid (pVIII and pIII)[233,274] that are able to selectively bind and identify a target biomolecule having implications in a series of human syndromes[232 275–278]. Since there are approximately 2700 copies of pVIII per single phage, it is possible to produce highly multivalent libraries[279] composed by phage expressing randomic peptides. The phages of interest are isolated, then, by including the libraries in a biopanning process and exposing them to the specific target[280–283]for the affinity selection. These selected phages, used as probes, demonstrated to have high specificity against their targets, high thermal stability, and are not affected by changes in surrounding compositions[284,285]. The application of phages brings also advantages in rapid diagnosis[286], low cost, and resistant to harsh conditions, including organic solvents and high temperatures, and can discriminate between viable and not bacteria[286,287]. Furthermore, the use of phages instead of enzymes or secondary antibodies as biorecognition probes significantly improves the biosensing performances in terms of stability to thermal and pH variations, reduction of synthesis and purification costs and greater avidity of the binding of the target, solving some of the main problems related to the enzymatic probes typically used in conventional ELISA[259,288,289]. [275–278]. Since there are approximately 2700 copies of pVIII per single phage, it is possible to produce highly multivalent libraries[279] composed by phage expressing randomic peptides. The phages of interest are isolated, then, by including the libraries in a biopanning process and exposing them to the specific target[280–283]for the affinity selection. These selected phages, used as probes, demonstrated to have high specificity against their targets, high thermal stability, and are not

affected by changes in surrounding compositions[284,285]. The application of phages brings also advantages in rapid diagnosis[286], low cost, and resistant to harsh conditions, including organic solvents and high temperatures, and can discriminate between viable and not bacteria[286,287]. Furthermore, the use of phages instead of enzymes or secondary antibodies as biorecognition probes significantly improves the biosensing performances in terms of stability to thermal and pH variations, reduction of synthesis and purification costs and greater avidity of the binding of the target, solving some of the main problems related to the enzymatic probes typically used in conventional ELISA[259,288,289].

The phage display has been applied to the early diagnosis and monitoring of AD[258,259,290]The phage display has been applied to the early diagnosis and monitoring of AD[258,259,290], in which modified filamentous phages (M13, Fd, f1)[291] were used to identify the Aβ peptide involved in the formation of amyloid fibres[292]. However, most of these applications were limited by the integration of plastic material, that affect both stability and reproducibility of the method. The combination with silicon material, on the other hand, is still few explored. Silicon technology would overcome the limitations of plastic-based phage display by introducing many technological advances such as high sensitivity transduction, fluidic movement and electronic reading[293]. Silicon would also bring excellent material properties, in terms of good heat capacity and thermal conductivity, the possibility of nanostructuring, that could to increase the surface–area ratio, and a high level of opto-electronics miniaturization and integration, that would open towards the possibility of new PoC applications and diagnostics decentralization[140,149,208,294,295] .

Within this perspective, we developed a combined innovative silicon-based sensing technology for the AD diagnosis by phages probes, using human sera as testing samples. This work has been published in 2024 to the Advanced Materials Interfaces Journal[296].

3.1.1. Experimental

The technology proposed was based on a biosensing surface that has been appropriately derivatized on top of two silicon substrates: i) a flat silicon slide, used as reference model for characterization; ii) a miniaturized chip, used in first trials of PoC application. The sensing surface was structurally and chemically characterized by atomic force and scanning electron Microscopy (AFM and SEM), X-ray photoelectron spectroscopy (XPS), and contact angle measurements (CA). The molecular recognition of AD Aβ-autoantibodies in human sera by phage probes was ascertained by transduction with enzyme-linked anti-M13 antibodies.

3.1.1.1. Human sera

Sera used were provided by the Neurologic Unit of the University Hospital "Policlinico Vittorio Emanuele" of Catania, Italy, and diagnosticated as AD by the Mini Mental State Examination (MMSE). The study was approved by the Ethics Committee of the "Policlinico Vittorio Emanuele" of Catania. For the testing experiments, 3 sera with MMSE between 12 and 15 (severe AD) of a 75-year-old male patient, containing AD Aβ autoantibodies, and 3 sera with MMSE of ≈29 (healthy) were used. It was diluted 1:50 in a buffer, prepared by mixing 50 mL PBS with 500 mg of 1% non-fat dried milk powder and 50 µL of 0.1% Tween 20.

3.1.1.2. Phage-probe preparation

The ADPP phage probe (named 12CIII1) used for the experiments has been previously selected[258].The ADPP phage probe (named 12CIII1) used for the experiments has been previously selected[258]. To prepare it, 90 µl of exponential culture broth (LB) of the TG1 strain of E. coli (Kan-, Amp-, lacZ-) was infected with 10 µl of ADPP, then incubated at 37 ◦C in static conditions for 15 minutes, followed by stirring for 20 minutes. After incubation, culture was plated onto Luria–Bertani modified with bacteriological agar (Condalab) plates containing 50 µg mL−1 of ampicillin (Merck) and incubated at 37 ◦C in static condition. A colony of transformed E. coli was inoculated into 10mL of LB

containing ampicillin and incubated at 37°C with shaking until an optical density (OD) of 600 nm = 0.2 was reached. Then, isopropylthio-β-galactoside (IPTG, 40 μg mL^{-1}), from Merck, was added to the culture and helper phage M13K07 (109 TU mL^{-1}), incubated at 37 ◦C under static conditions for 30 minutes, and shaken gently for 30 minutes. By centrifugation at 8000xg, the cells were collected and transferred into 500mL of LB medium containing ampicillin and kanamycin (50 μg mL^{-1}), from Merck, and incubated overnight with shaking at 37 ◦C. Subsequently, the infected culture was centrifuged at 8000× g for 20 min at 25 ◦C, the supernatant was then mixed with 25% (v/v) PEG/NaCl solution (Merck), chilled on ice for 4 h and precipitated by centrifugation at 15000× g for 45 min at 4 ◦C. The pellet was resuspended in 10% (v/v) TBS (Merck), mixed again with 25% (v/v) PEG/NaCl, chilled on ice for 4 hours, and the solution was centrifuged as above. Finally, the pellet containing the phages was suspended in 10% (v/v) TBS, filtered through a 0.22 μm pore size membrane (GVS), and stored at 4 ◦C.

3.1.1.3. Sensing surface functionalization based on silicon substrate

A 3 mm × 3 mm flat silicon substrate was chosen as sensing surface for first characterization. The functionalization scheme involved the use of a Teflon beaker as a processing support. First, it was necessary to clean the surface with a basic piranha solution H_2O_2:NH_3:H_2O (1:1:4) at 80 °C for 25 min, which has the characteristic of being a strong oxidant. After rinsing in ultrapure water, a treatment was performed on the surface with an acid solution (HCl:H_2O, 1:7.5) at room temperature for 10 min. Subsequently, the surface was silanized via chemical value deposition (CVD) with GOPS (Glycidyloxypropyl)trimethoxysilane) silane at 125 °C for 4 h. Then, the surface was rinsed with a washing buffer composed of 50 mL of PBS + 25 μL of 0.05% Tween 20 and used for the subsequent functionalization step. Recombinant protein G was anchored to the silanized surface by soaking the silicon substrate overnight at 4 °C with 200 μL of 0.5 μg mL^{-1} protein G solution diluted in PBS. Then the substrate was rinsed three times with PBS.

3.1.1.4. Sensing surface preparation of silicon chip

The second substrate was a miniaturized 1 cm × 2 cm silicon chip composed of six circular wells of 3 mm diameter that have been realized by lithography of a 15.24 cm diameter silicon wafer. On top of the silicon chip a polycarbonate mask was attached creating six microchambers of 25 µL capacity. To avoid fluids leakages during the functionalization and testing treatments, the silicon wells and the plastic mask were aligned and glued via a conductive resin. The sensing surface was treated according to the protocols above described using a volume of 20 µL for each treatment.

3.1.1.5. Testing and surface characterization analysis

Once functionalized, the AD sensing performances of the silicon surfaces were tested by a three-step approach: (1) antibodies binding; (2) ADPP phage recognition; (3) transduction by M13 phage ELISA assay.

(1) The G protein is known to bind the Fc domain of IgG antibodies. The IgG binding step was performed by adding healthy human sera and AD. As a negative control, plain 10 mM PBS was used. First, 200 µL of sera diluted 1:50 and 10 mM PBS (negative control) were added to each Teflon beaker containing the silicon surface and incubated for 1 h at 37 °C with 80 rpm of shaking. For the silicon chip, 20 µL of diluted sera was used. Finally, unbound IgG was removed via three steps of cleaning the wash buffer.

(2) The ADPP phage recognition of anti-Aβ antibodies was a crucial step. To prevent possible non-specific binding by the phage, the exposed silicon points on the surface were blocked. A preliminary passivation of the silicon surface and the chip was performed, incubating the substrate with 200 µL in one case and 20 µL for the chip, of a blocking solution prepared by mixing 5 mL of 0.01 m PBS with 250 mg of milk skimmed powder and 2.5 µL of 0.05% Tween 20 for 2 hours at 37 °C. Once passivation occurred, the recognition of Aβ autoantibodies was performed by spotting 10^{11} copies of ADPP probe diluted in 0.01M PBS for 1 hour at 37°C with 80 rpm of stirring. Any unbound phages were removed by five steps of cleaning the wash buffer.

(3) The transduction was performed by M13 phage ELISA assay using a volume of 200 µL of a 1:750 solution of HRP-conjugated anti-M13 IgG, suspended in dilution buffer, added to both silicon substrates previously treated with steps (1) and (2). These were incubated at 37 °C for 1 h with 80 rpm of stirring. For the silicon chip, 20 µL of HRP-conjugated anti-M13 IgG was used, the chambers were rinsed three times with wash buffer and used for the final immunochemical analysis. The immunological detection was performed by adding 100 µL of 3,3′,5,5′-tetramethylbenzidine (TMB) for the functionalized silicon surfaces and incubated for ≈15 min at room temperature in the dark, while for the silicon, 10 µL of TMB was used. If AD positive samples are present a blue color will appear, due to oxidation of TMB by HRP. The reaction will be stopped by adding 100 µL, and 10 µL for the chip, of H_2SO_4 0.6 N, causing a color change from blue to yellow. The color intensity was then measured by reading the absorbance of the samples at 450nm using a VICTOR 3S V Multilabel Plate Reader spectrophotometer. In the case of the silicon chip, the volume of each well was transferred to a 96-well plate and diluted tenfold by adding 180 µL of PBS, to obtain the correct volume for the absorbance reading; subsequently, the absorbance values were corrected by multiplying by the dilution factor. Statistical analysis was performed via one-way ANOVA test using GraphPad InStat version 3.1.

As mentioned, each step of the sensing surface assembly (GOPS silanization, G protein anchoring, IgG binding and probe phage capture) was studied to evaluate the correct functionalization of the substrates. The topography and surface composition was studied using three different techniques in collaboration with the group of Prof. Condorelli of the University of Catania: a) AFM, performed by a SolverP47 NT-MDT instrument, in semicontact mode, using a scan window of 5 µm × 5 µm and 2 µm × 2 µm. Silicon probes (NT-MDT) with constant force in the range of 0.01–0.5 Nm have been used for the analysis. All the data for each AFM image were evaluated by Gwyddion software; b) SEM, using a ZEISS VP 55 field emission SEM (FESEM) (Oberkochen, Germany); c) XPS, carried out with a with a PHI 5000 Versa Probe Instrument using a monochromatic Al Kα X-ray source excited with a

micro-focused electron beam. All the analyses were performed with a photoelectron take-off angle of 45 (relative to the sample surface). The XPS binding energy (B.E.) scale was calibrated on the C 1s peak of adventitious carbon at 285.0 eV.

Lastly, the wettability of the surface was evaluated by CA analysis. The CA, as a function of the surface wettability after each functionalization step, was assayed in drop casting mode using 1 µL of distilled water and analyzing the drop age at 4 time points (0, 68, 134, and 203 s). In parallel, CA was also measured using a drop of buffers citrate at pH 4.40 and 6.02, buffers carbonate/bicarbonate at pH 9.36 and 10.2, to evaluate the isoelectric point (IP), and the surface charge profile of the biomolecules anchored in step-by-step assembled sensing surface.

3.1.2. Results and discussion

The silicon-based detection strategy was based on the molecular recognition of Aβ-autoantibodies using the ADPP probe expressing the RWPPHFEWHFDD capsid peptide, attracted to the silicon surface by the Aβ autoantibodies and detected by transduction with silicon-bound anti-M13 antibodies. To do this, as shown in **Figure 3.2**, the silicon surface was functionalized with GOPS through a covalent bond between its Si-OCH_3 groups and the -OH groups exposed by the surface (previously formed by activation treatment with piranha solution).

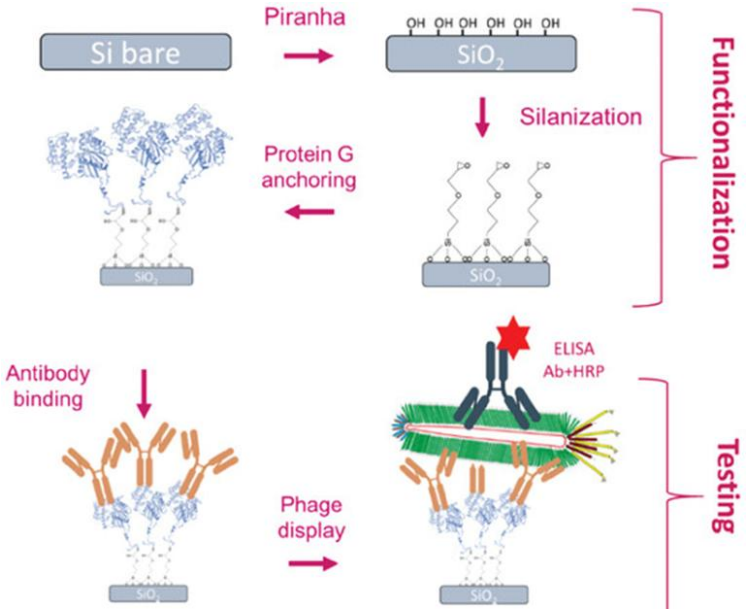

Figure 3.2. Silicon- ADPP detection strategy for Aβ-autoantibodies identification.

A crucial step in this functionalization was the anchoring of the protein G. This streptococcal protein binds the human IgGs 1-4 in the Fc domain with extreme selectivity, thus, avoiding unspecific interactions with other IgM and IgA[297]. Therefore, the formation of the protein G layer is fundamental for the detection strategy since affect the quality of sera IgGs capture and immobilization. In the silicon-based sensing strategy the IgGs orientation should be done in an proper orientation, so that the antigen binding sites (Fab domain) could be correctly exposed for the ADPP interaction[298]. The improvement of the detection efficiency due to the IgGs orientation has been preliminary proved by testing in triplicate an AD serum in ELISA performed on a plastic 96-well plate functionalized with and without the protein G layer. Results, reported in **Figure 3.3,** shown four times enhanced absorbance values of wells functionalized with protein G.

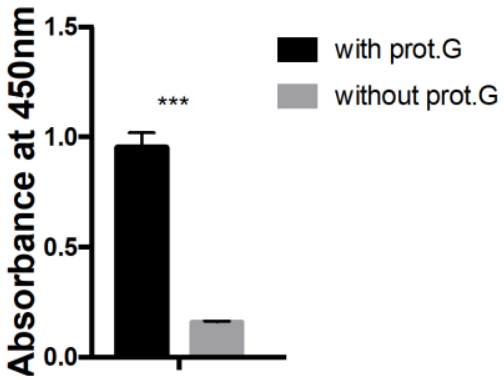

Figure 3.3. ADPP recognition of AD serum on plastic surface with and without protein G functionalization.

After verifying the efficiency of the protein G, it was possible to obtain the specific identification of Aβ-autoantibodies via molecular recognition with an ADPP probe, forming the IgG-ADPP molecular complex ("Functionalization" of **Figure 3.2**). In fact, this phage brings on its pVIII capsid hundreds of copies of a Aβ-mimics peptide that molecularly recognize specific regions of Aβ-autoantibodies, thereby discriminating between healthy and AD sera[258].In fact, this phage brings on its pVIII capsid hundreds of copies of a Aβ-mimics peptide that molecularly recognize specific regions of Aβ-autoantibodies, thereby discriminating between healthy and AD sera[258]. While the Protein G layer immobilize all the IgGs present in the serum, ADPP will bind only the Aβ auto-antibodies, thus proving selectivity to the assay. The IgG-ADPP complex is subsequently transduced with a secondary probe constituted by the enzyme-linked anti-M13 antibodies conjugated with HRP that produce a colorimetric signal ("Testing" of **Figure 3.2**).

The AFM and XPS analyses of step-by-step functionalization was done in order to deeply characterize surface morphology and composition after each modification and to validate the effectiveness of the chemical protocol.

The first step analyzed was the GOPS sample. The AFM image, shown in **Figure 3.4a**, shows a flat surface due to the formation of a homogeneous layer of the silane on the silicon surface. This was further confirmed by the RMS

data, 0.267 nm, and the height distribution profile, in Figure 3.6a, which reveal an average height peak at 0.94 nm while the height profile in Figure 5b shows no structure on the surface , thus providing a homogeneous background.

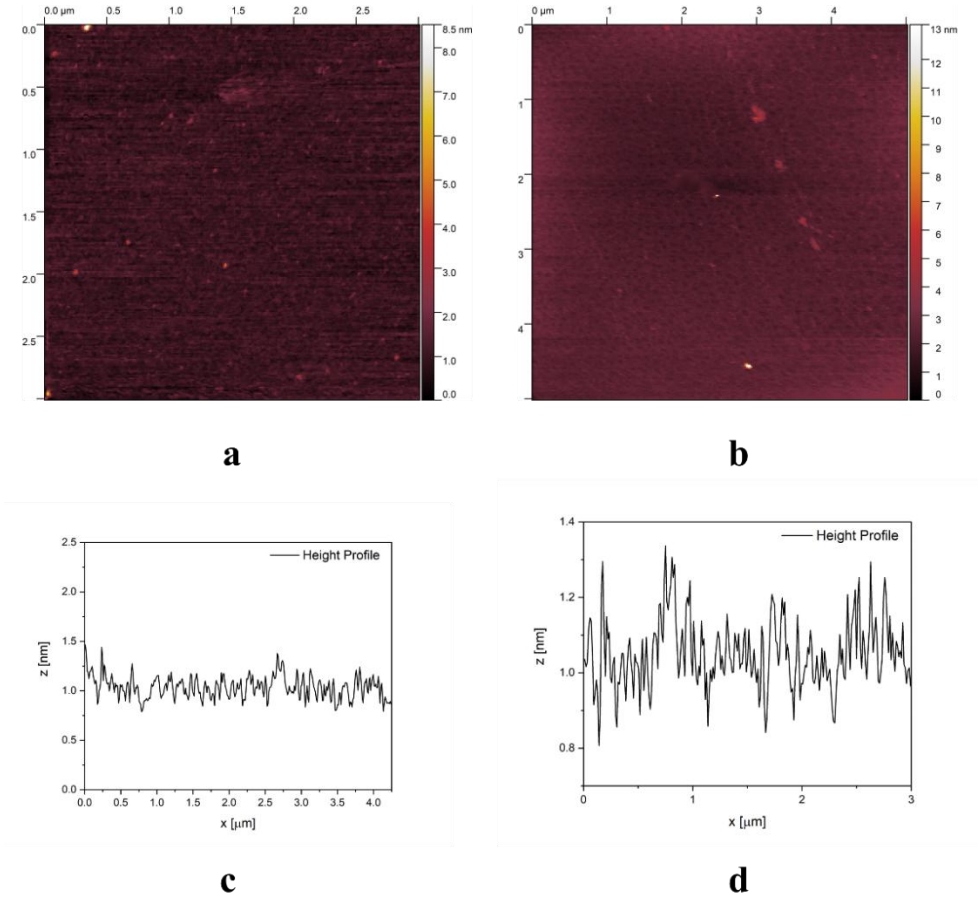

Figure 3.4. AFM analysis of GOPS and GOPS-PG surfaces: a,c) surface topography, and b,d) heights distribution profile.

The next step concerns the AFM analysis of the SiO2 surface functionalized with GOPS after the anchoring of protein G (GOPS-PG). The images showed no noteworthy holes or rough features, **Figure 3.4c**. However, analyzing the RMS data shows an increase in surface roughness of 0.33 nm, 25% more than that of the GOPS sample, which could be attributed to the additional protein G layer anchored to the silane layer.

This hypothesis was further supported by the height distribution profile where the average peak deconvolution, obtained by fitting two Gaussian functions,

reveals the presence of two dispersed objects on the GOPS-PG surface. Indeed, as described in **Figure 3.5b**, Fit Peak 1 (red line) reports an average height of 1.1 nm, which could be related to the GOPS distribution, while Fit Peak 2 (green line) provides an average of 1, 4 nm, attributable to the protein G layer. This surface structuring is also confirmed by the background reported in the height profile shown in **Figure 3.4d**.

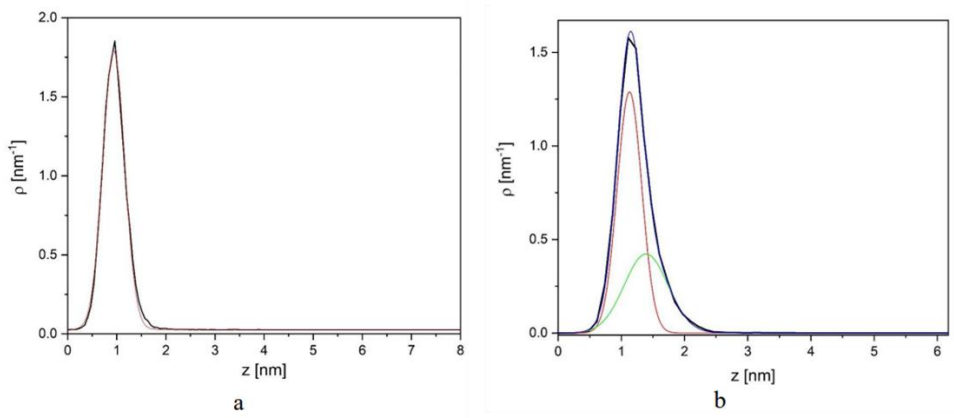

Figure 3.5. a) Height distribution of Figure 3.5a; b) Height distribution of Figure 3.5c.

The success of the proposed assembly up to the GOPS and GOPS-PG steps was confirmed through the XPS analysis reported in **Figure 3.6**. In particular, the C1s band relating to the GOPS can be deconvoluted into three components: the primary component at 285, 0 eV corresponds to the hydrocarbon skeleton of GOPS and adventitious carbon. A second component to be considered at 285.8 eV can be attributed to the oxidized carbon in the ether group, while the third component at 287 eV represents the carbon of the epoxy groups. The shape of the bands changes significantly once the protein G is anchored. In fact, in addition to the typical C1s signal at 285 eV, the spectrum is characterized by the prominent signal of the oxidized carbon at 286.4 eV which derives from the carbon atoms of the carboxyl groups of the protein. Lastly, the N1s peak was found at 399.8 eV and was only detected in the sample containing the protein G, due to its amino acid composition, confirming the covalent binding of the molecule to the GOPS layer.

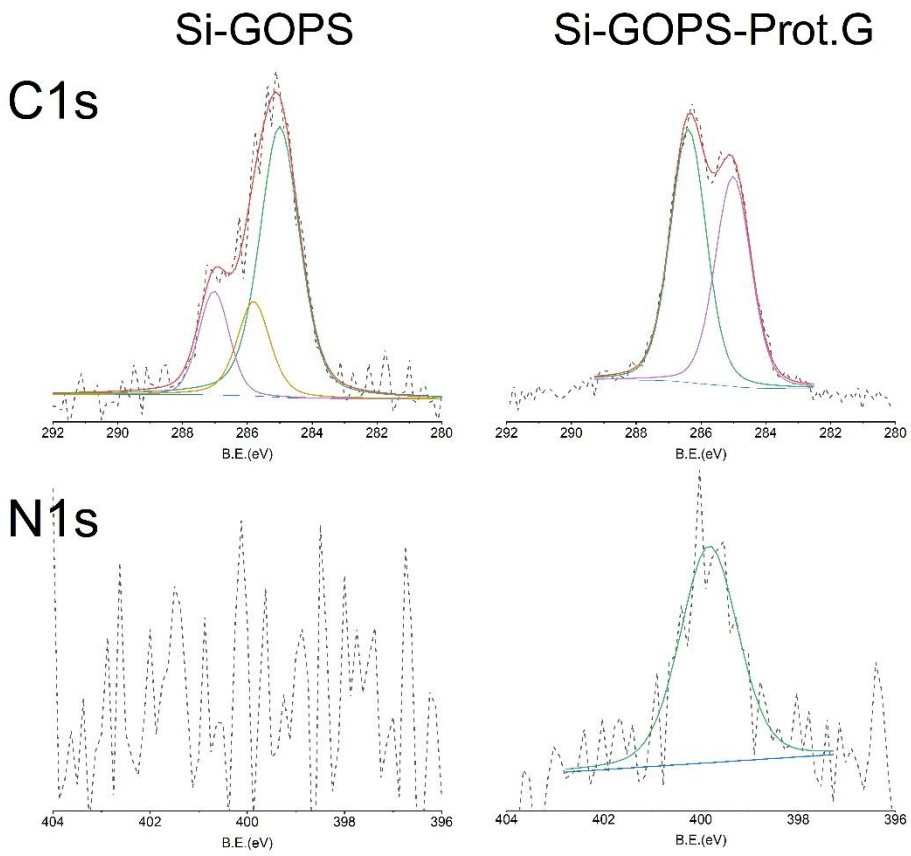

Figure 3.6. XPS analysis of C1s and N1s spectral regions of GOPS and GOPS-PG surface.

As previously described, IgG present in human sera has the ability to effectively bind to the formed protein G layer, exposing antigen binding sites (F_{ab} domain) towards the phage probe. To evaluate and visualize the effectiveness of this binding, an AFM analysis was performed at the GOPS-PG biointerface after the step that included IgG anchoring. The data is shown in **Figure 3.7a–h**. As highlighted by the images, there is topographic variation due to the presence of widely distributed circular features. In the 5 µm × 5 µm and 2 µm × 2 µm AFM images shown in **Figure 3.7a and d** the presence of these large structures correlates with an accumulation of organic material. Looking in detail at the height profile in Figure 4b, referenced to line 1 in Figure 4a, a feature with a height between 2 and 15 nm is shown, where the few larger structures in the range 5–15 nm can be identified as IgG aggregation.

Furthermore, it is interesting to note the configurations of the structures shown in **Figure 3.7b** and **Figure 3.8 a and b** which reveal a distinct conformation with two peaks at the bodies' tips, possibly associated with the characteristic “Y” shape structure commonly observed in IgG.

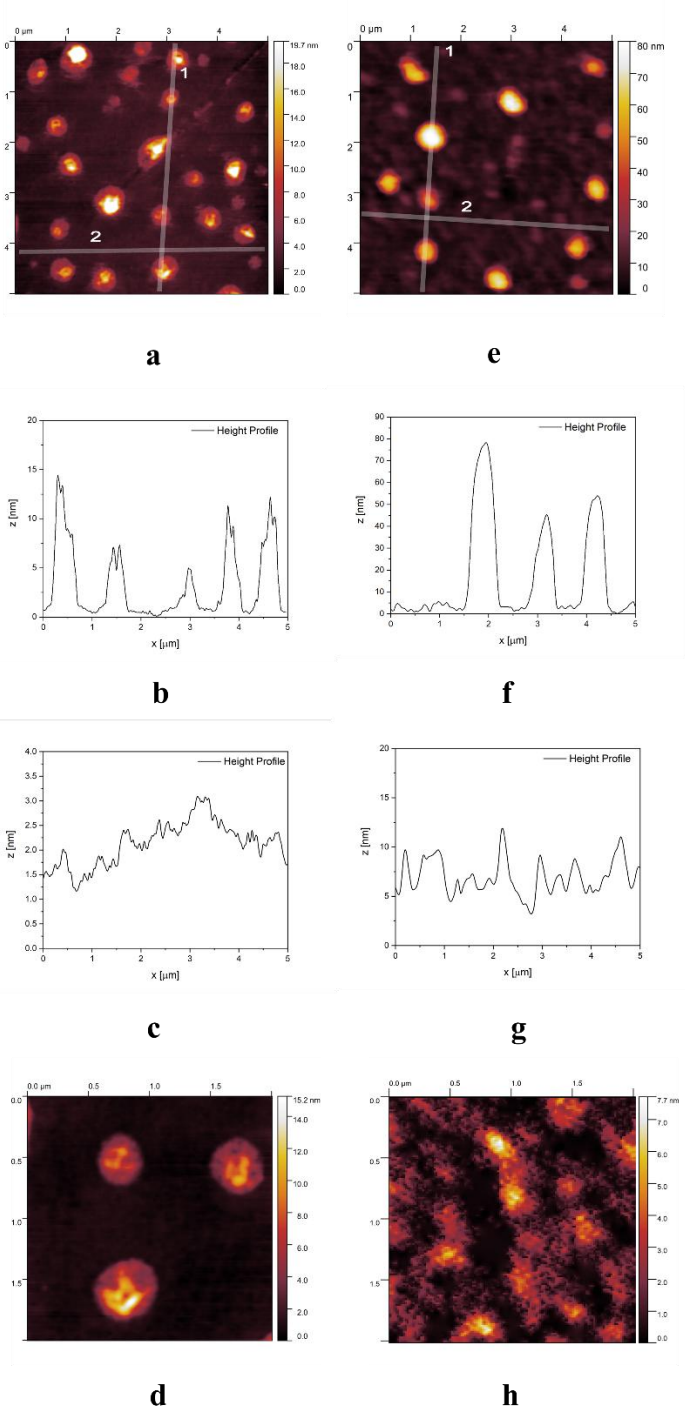

Figure 3.7. AFM analysis of GOPS-PG-IgG and GOPS-PG-IgG-ADPP surfaces. a) AFM topography at 5 μm × 5 μm of GOPS-PG-IgG; b) Heights profile of the line 1 in Figure 8a,c) Heights profile of the line 2 in Figure 4a; d) AFM topography magnification of Figure 8a at 2 μm × 2 μm of GOPS-PG-IgG focused on the antibody; e) AFM topography at 5 μm × 5 μm of GOPS-PG-IgG-ADPP; f) Heights profile of the line 1 in Figure 8d; g) Heights profile of the line 2 in Figure 8d; h) AFM topography magnification of Figure 8d at 2 μm × 2 μm of GOPS-PG-IgG-ADPP focused on the surface after the ADPP adhesion.

A height profile along line 2 in **Figure 3.7a**, obtained without intersecting the prominent features, and the total height distribution are presented in **Figure 3.7c** and **Figure 3.8e** to illustrate the morphology of the background outside the large IgG assemblies. The height distribution indicates how most of the features are in the range 3.8-5.5 nm, which confirms the variations in morphology compared to the GOPS and GOPS-PG samples where almost all the features were in the range 1- 2 nm. These data were consistent with previous literature works, in which an average of heights for antibodies in the range of 3-8 nm are indicated[299,300].

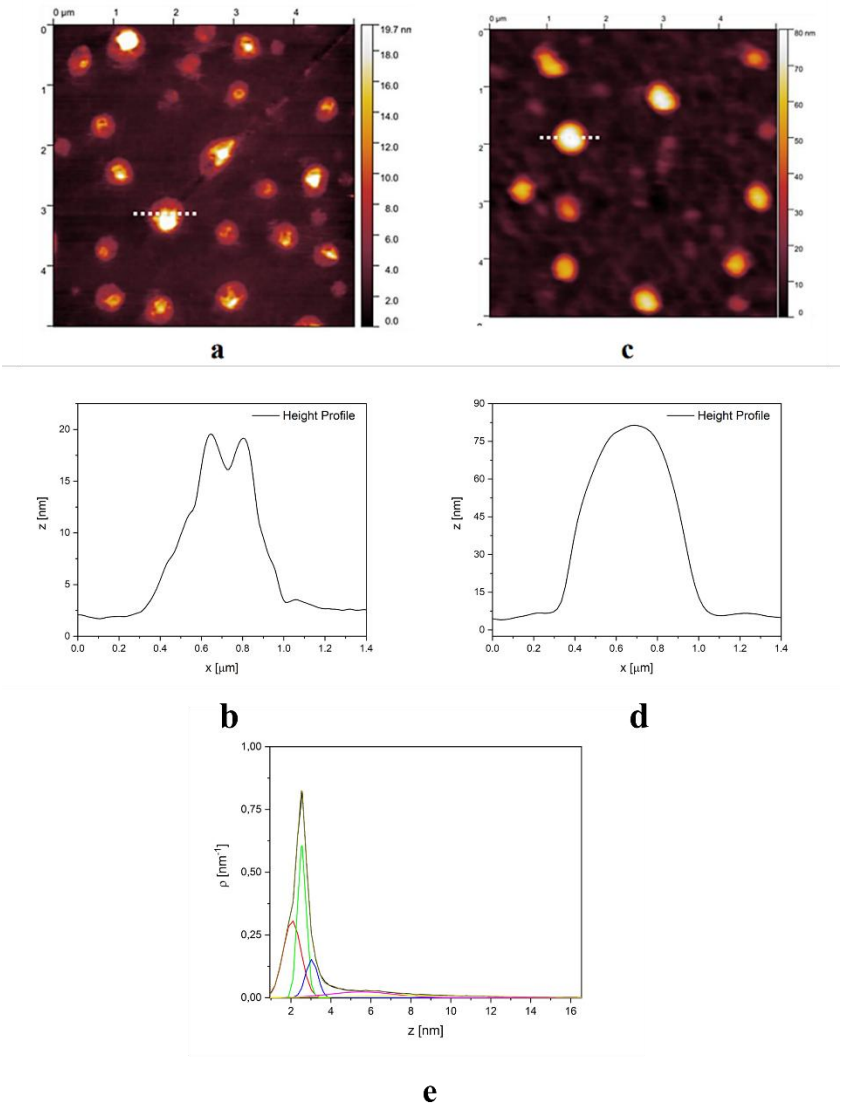

Figure 3.8. a) AFM image of GOPS-PG-IgG; b) height profile of the dotted line in (a); c) AFM image of GOPS-PG-IgG-ADPP; d) height profile of the dotted line in (c); e) Height distribution of figure 4a GOPS-PG-IgG.

The RMS analysis confirmed the topographic evidence by reporting an increased surface roughness of 3.11 nm, compared to the 0.33 nm of the GOPS-PG sample.

The efficiency of the binding between the protein G layer and IgG was further highlighted through SEM inspection. The comparison of GOPS-PG-IgG and GOPS-IgG samples is shown in **Figure 3.9**. In the first sample. **Figure 3.9a**, due to the strong interaction of the Fc domain of IgG with the G protein there is a wide and uniform distribution. A completely different situation was

observed in the second sample, **Figure 3.9b**. In this case the absence of the protein G caused the formation of IgG aggregates as a consequence of unspecific Fab-Fab lateral interactions[301,302] between physiosorbed antibodies. Lastly, through topological and morphological analyses, the link between IgG and ADPP was determined. We inspected the morphology of the GOPS-PG-IgG-Phage biointerface via AFM and SEM analysis. AFM topographic images of this surface, **Figure 3.7e**, show the presence of larger features than those observed in the GOPS-PG-IgG surface, **Figure 3.7a**. The height profiles related to lines 1 and 2 of **Figure 3.7e** are reported in **Figure 3.7f and g** respectively, highlighting the presence of large structures of height ≈50 nm, **Figures 3.8a and b**, and a background outside these structures (line 2) with a morphology that presents a greater height and less roughness compared to the GOPS-PG-IgG samples due to the presence of ADPP.

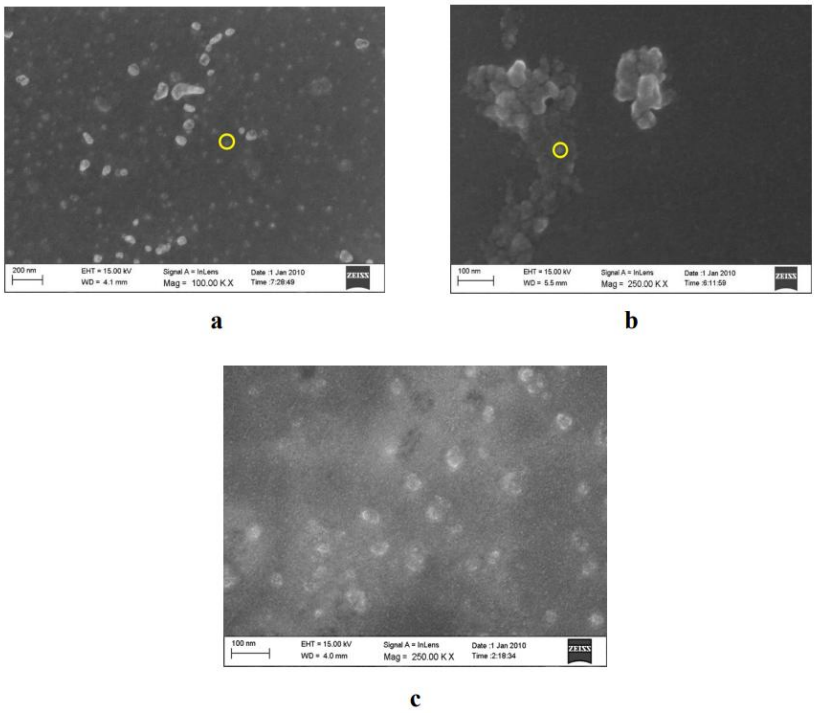

Figure 3.9. SEM analysis of GOPS-PG-IgG (a), GOPS-IgG (b) and GOPS-PG-IgG-ADPP (c) surfaces.

This is consistent with the observed roughness, which changes from 3.11 to 10.9 nm in the absence and presence of ADPP on the surface, respectively. Furthermore, magnification, **Figure 3.7h**, of a 2 μm × 2 μm area without large

structures shows a distribution of objects across the entire IgG surface with a length of ≈0.25 μm and with a height distribution of ≈ 5,8 nm, **Figures 3.10a,b**. These objects were associated with the captured probe phage. The SEM image confirms the presence of the phage with a topographic profile exposing blurry fractal bodies, **Figure 3.9c**.

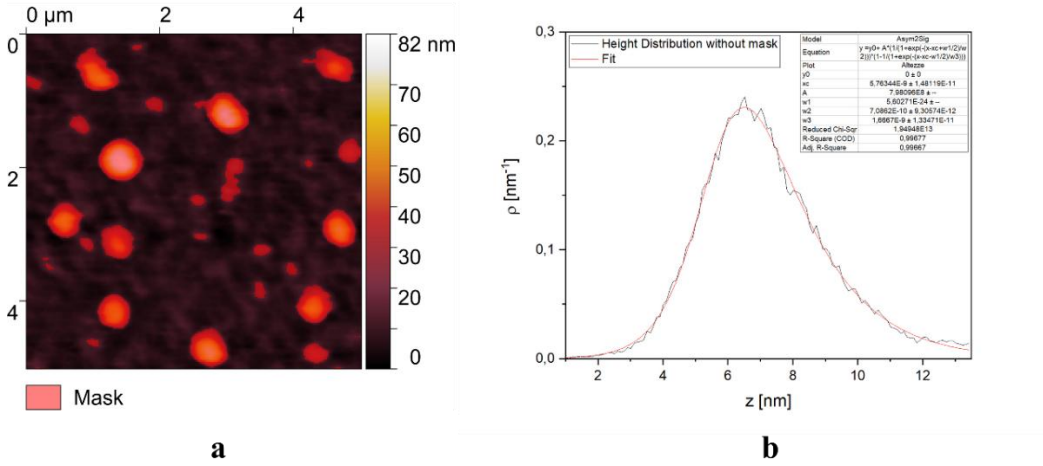

Figure 3.10. a) Masked AFM topographic image of Figure 3.7d; b) Height distribution of Figure 3.7d of the unmasked surface.

CA measurements were carried out in drop casting mode using 1 μL of ultrapure water for each surface functionalization phase to confirm the effectiveness of interface functionalization. The results, recommendations in **Figure 3.11a**, show a CA statement of ≈40° after the silicon surface cleaning step due to the –OH groups making the surface more hydrophilic. With GOPS silanization, however, the CA increased by >70° due to the hydrophobic coating caused by the organic layer. Then, the wettability significantly increased again after each biomolecular assembly process due to the addition of polar protein G, IgG, and phage structures. Furthermore, it was interesting to study the surface charge characteristics of anchored biomolecules through CA analysis at different pHs in the range 4-10. The results reported **in Figure 3.11b**, (the dashed lines have been added just as a guide for a better data visualization) show a qualitative trend of the surface wettability as a function of pH for the various functionalization levels. The silanized surface (black symbol

in **Figure 3.11b**) was inert to pH variations and therefore without changes in wettability, probably due to the non-polar nature of the silane.

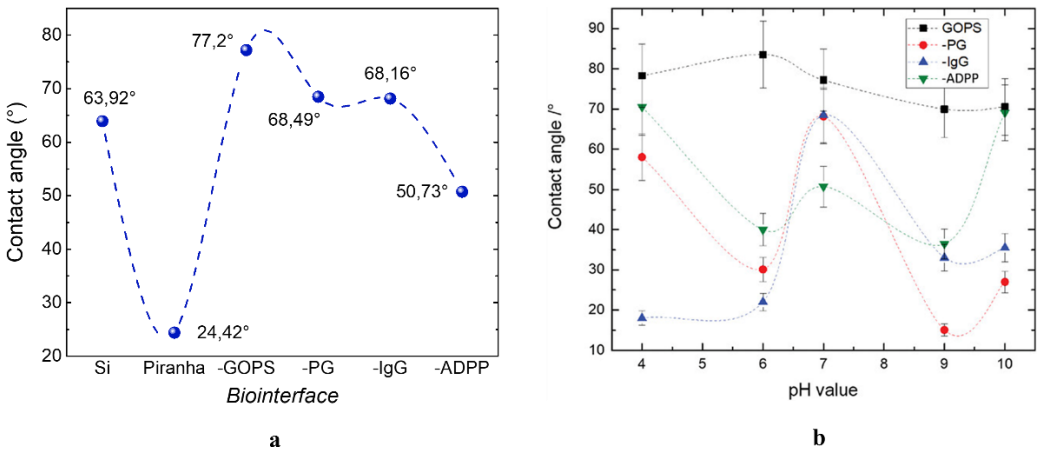

Figure 3.11. a) CA analysis of sensing surface step-by-step assembly; b) CA analysis of GOPS (black line), GOPS-PG (red line), GOPS-PG-IgG (blue line), and GOPS-PG-IgG-ADPP (green line) samples at 4–10 pH range.

On the contrary, both the PG and PG-IgG derivatized surfaces (red and blue symbols, respectively), show a wettability change linked to pH with a first increase of CA at pH 4 for the PG and a second common peak at pH 7 for both PG and IgG molecules. Indeed, the biostructures of protein G and IgG are both composed of zwitterionic amino acids, suggesting an isoelectric point (Ip) of approximately pH 7. Finally, the complete GOPS-PG-IgG-Phage surface (green symbols) gave a different behaviour of wettability, probably, because of the presence of protein capsids and peptides exposed to the pVIII fraction of docked phages. This observed behaviour can be attributed to specific conformational changes of the ADPP structures and charge arrangement due to their molecular interactions in combination with the ionic strength of the buffer used for the analysis.

Lastly, after verifying the correct assembly of the biointerface, to evaluate the validity of the biosensing strategy, we tested three healthy sera and 3 ADs, comparing them with negative controls made with 10 mM PBS. The presence of ADPP in all samples was verified by performing immune recognition with

HRP-conjugated anti-M13 antibodies producing a colour absorbance at 450 nm. The results reported in **Figure 3.12** indicate that the biointerface can detect autoantibodies in both healthy and AD sera. The data show a good tendency in discriminating AD sera from healthy ones (absorbance equal to 0.18 ± 0.06 for healthy sera and 0.85 ± 0.3 for AD sera), also highlighting that our biointerface is suitable for use in an integrated biosensor device.

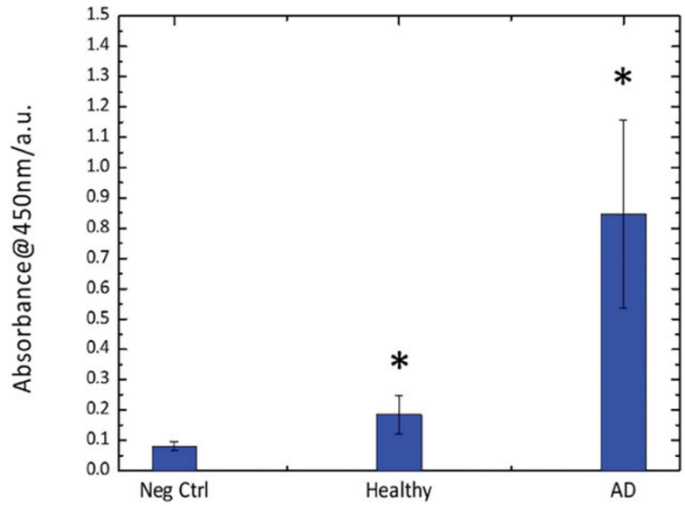

Figure 3.12. ADPP immune recognition of the silicon bio-surface of negative control, healthy, and AD sera. Data were analyzed by one-way ANOVA test ($p < 0.0001$).

To this end, we transferred the biointerface built on flat silicon into a silicon biochip, as a first prototype, to demonstrate the possibility of developing a miniaturized biosensor for a future PoC device for early diagnosis and screening of AD. Therefore, we applied the developed sensing strategy to a silicon chip schematized in **Figure 3.13a**, which was chemically functionalized following the same chemical protocol described in **Figure 3.2**. The chip was composed by 6 reaction chambers in which we performed the detection assay using two replicates of three negative controls and three types of healthy and AD sera. The results are reported in **Figure 3.13b** and showed a statistically significant change in absorbance between the healthy (Abs 450nm = 0.42 ± 0.08) and the AD sera (Abs 450nm = 0.78 ± 0.22).

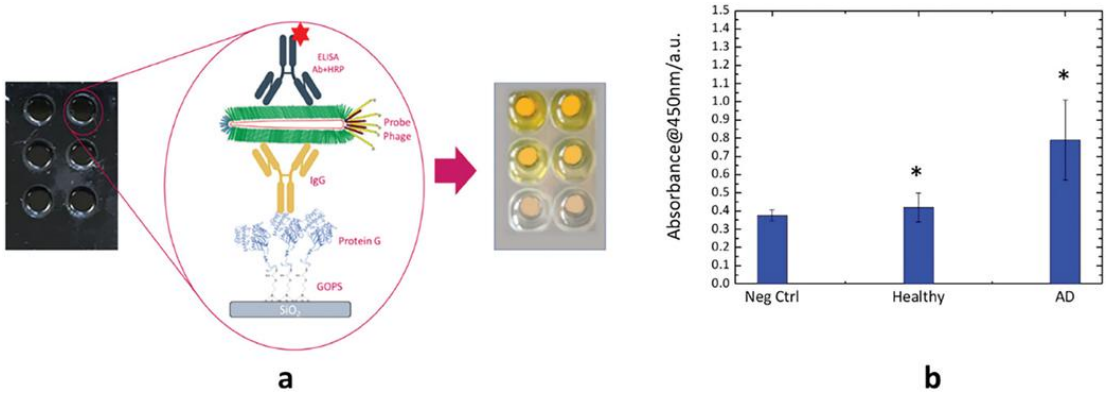

Figure 3.13. a) Silicon biochip; b) immune recognition of negative control, healthy and AD sera. Data were analyzed by one-way ANOVA test (p = 0.0002).

All data from both silicon flat substrate and chip testing were analyzed by one-way ANOVA test, which indicated a significant difference among the samples (negative control, healthy, and AD) group of values ($p < 0.0001$ for the Si flat and $p = 0.0002$ for the chip). Moreover, for both series of testing, post-hoc analysis with Tukey's correction indicated that the negative control group was not statistically significant from the healthy group. In contrast, the AD group was statistically significant from the other two groups ($p<0.001$ for both comparisons). These findings were the consequence of the specific interaction between the anchored Aβ-autoantibodies and the phage mimics peptides, that could lead to a higher number of captured phages, thus, a more intense detection by the secondary anti-M13 antibody conjugated with HRP. These results proved that thanks to the combination with the miniaturized architecture of a silicon chip, the technology opens to the possibility of a very large-scale integration toward a new frontier of decentralized biomedical diagnostics.

3.2. miRNAs electrochemical based sensing as biomarkers for Alzheimer's disease

Another approach for the AD screening, developed in my Ph.D. Thesis, was based on the PCR-free detection of miRNAs as disease biomarkers. MiRNAs are small non-coding oligo RNAs[265,266,303–307] that regulate the mRNA translation[308]. They are involved in several key biological processes, including

apoptosis, proliferation and differentiation[309]. In the nervous system, miRNAs are very important and are associated with neuronal patterning, synaptogenesis, neuronal plasticity and neurodegeneration[310,311]. Typical miRNA detection is performed via Northern blotting, quantitative reverse transcription (RT-qPCR), or microarray profiling, all of which are expensive, complicated, and time-consuming methods[266,312]. They play a prominent role in fine-tuning gene expression[313], which is why miRNAs have been associated with various pathological conditions[314] and have been described as promising biomarkers for various diseases including AD[315]. MiRNAs can be found in various biological fluids associated to the neurological disorder such as plasma, serum and cerebrospinal fluid (CSF)[316], usually in a vesicle-independent/free-floating form, which would facilitate the AD screening also in the perspective of an early diagnosis of diseases[311,317].

The development of biosensing strategies based on the detection of these molecular targets as AD biomarkers is very challenging, since the technologies should point towards faster, simpler and non-invasive screening also at an early stage compared to the conventional diagnostic techniques, thus, making therapies more effective [311]. Furthermore, thanks to their resistance to RNAse degradation and stability at prolonged storages, high temperatures, extreme pH conditions and multiple freeze-thaw cycles[308] and, for some types, the availability in the blood flow, the miRNA analysis would also open to possible integration into PoC devices making the AD screening more accessible.

With the aim of introducing new potential tools for the fast and accurate AD screening, we developed a new electrochemical PCR-free biosensing strategy based on miRNAs that improves AD detection in terms of time, costs and system architecture, also excluding the amplification steps required by the conventional RT-qPCR for miRNA analysis. A first study was performed in order to identify the best miRNAs candidate as potential biomarkers of AD, leading to the selection of miR-34a, miR-125b, miR146a and miR-29b, whose differential expression affects the physiological pathways of the neural cells. Indeed, the upregulation of miR-34a influences the expression of several genes belonging to the p53 protein network, as those involved in the caspase-

3 activation and apoptosis, leading to the enhancement of the p53 mediated neurons death[264]. The overexpression of miR-125b, instead, has been found to induce the Tau protein phosphorylation, promoting the AD progression, and influence the activity of factors involved in the cell cycle regulation (such as synaptic phosphoprotein, lipoxygenase, etc.)[263,318]. Lastly, the upregulation of miR-146a and the downregulation of miR-29a have been correlated to the neuroinflammation onset in AD[319].

The miR-146a was used for the first development and characterization of the sensing surface. To this purpose, CA and SFE measurements studying the surface wettability have been performed on top of a gold-sputtered silicon substrate functionalized by grafting thiol-modified oligonucleotides used as probes for the selective recognition, via direct hybridization in a perfect match, of the miRNA target. Subsequently, we modified the surface of a commercial gold electrode and tested the PCR-free sensing performances, in terms of sensitivity, selectivity and versatility, via CV and EIS analysis. The PCR-free technology has been also integrated on top of an amperometric chip, developed and provided by the Bruno Kessler Foundation (FBK), testing the technology suitability for a PoC format.

3.2.1. Experimental

Table 3.1 reports the thiol-modified probes developed for the recognition of all 4 miRNAs chosen as potential AD biomarkers. At the 5' end of each probe sequence a hexyl pendant (C6) was added as spacer for the right orientation of probes once anchored to the electrode surface, while the thiol group (HS-) allowed the thiol-Au complex and the self-assembled monolayer (SAM) formation. The following probes were reduced by Dithiothreitol (DTT) treatment and purified at a concentration of 1μM via SephadeX G-25 gel filtration in NAP-10 columns (from Cytiva).

Table 3.1. Use case thiol-modified probes

Probe	Sequence 5'-3'
miR-146a_P-T	HS-C6-AACCCATGGAATTCAGTTCTCA
miR-34a_P_T	HS-C6-ACAACCAGCTAAGACACTGCCA
miR-29a_P_T	HS-C6-TAACCGATTTCAGATGGTGCTA
miR-125b_P_T	HS-C6-TCACAAGTTAGGGTCTCAGGGA

The chemical functionalization of the gold surface was fully characterized by CA and SFE analysis using a gold-sputtered silicon sample as substrate.

3.2.1.1. Gold surface functionalization for CA analysis

The gold-sputtered silicon substrate of 0.55 cm x 1 cm was functionalized with miR-146a probes as schemed in **Figure 3.14,** according to the chemical protocol reported in the previous section.

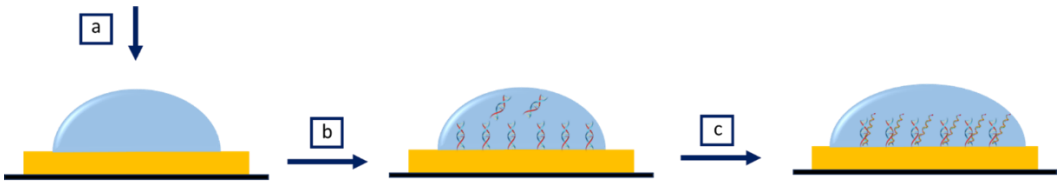

Figure 3.14. Gold substrate preparation: (a) surface cleaning; (b) miRNA-146a probe grafting; (c) miRNA perfect match formation.

For the not amplified genetic target hybridization, the syntethic miRNA_146a was diluted to 1 µM in nuclease-free water. The final gold interface functionalized with miRNA_146a probes were dipped in miRNA target solution at 50 °C for 3.5 h. Then, the unbound miRNA was washed away from surface by water. We performed the surface characterization analysis using four replicates of each functionalization step.

3.2.1.2. Commercial gold electrode functionalization

The substrate used for the sensing tests was a commercial gold electrode from CH Instruments. For the sensitivity and cross-reactivity tests it has been used

the probes and target of miR-146a as follows. The electrode surface was modified by grafting the thiol-terminated oligonucleotide probes (**Table 3.1**) and the synthetic miR-146a, according to the functionalization protocol reported in **Figure 3.15**. The electrode surface has been first cleaned using the following treatment: polishing of the gold surface with alumina slurry and washing by sonication in 50% ethanol solution for 5 min; cyclic voltammetry in 0.5 M H_2SO_4, in the range of −1 V to 1 V for 10 cycles; drying with Ar gas. Then, the electrode was incubated with a mix solution (1:10 ratio) of thiol-modified probe1 µM, suspended in PBS 10 mM at pH = 6.0, and 10 µM of 6-mercapto-1-hexanol ($C_6H_{14}OS$), dissolved in 10 mM PBS at pH = 6.0, at 25°C for 4 h with 60 rpm of stirring. The once functionalized with probe and thiol, the electrode surface was washed with PBS at pH 6.0. For the perfect match formation with miRNA-146a target, the probe-gold assembled interface on the electrode surface was dipped initially in a miRNA solution 1µM, prepared by diluting the stock solution (mimetic models produced by MeTabion) 100µM in ultrapure water, and incubated at 50 °C for 3.5 h. Lastly, a washing step with ultrapure water removed the unbound miRNA. Subsequently, the analytical performance was evaluated with two concentrations of mimetic miRNA-146a (5nM and 500nM), while the cross-reactivity test was evaluated by exposing the sensing surface to an unspecific (US) miRNA of same length of the synthetic target. Electrochemical analyses were performed using three replicates for each functionalization step, miRNA-146a and US concentrations tested.

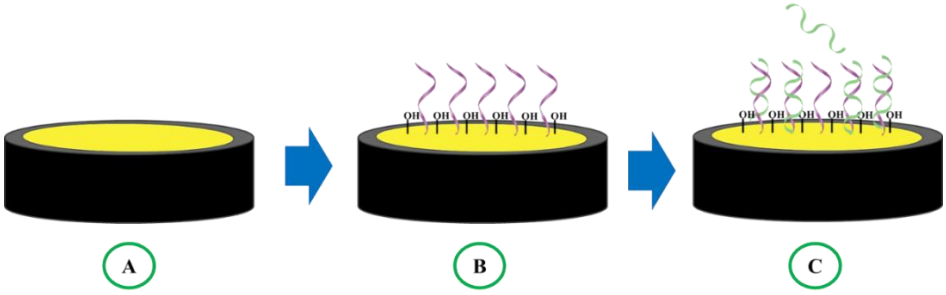

Figure 3.15. Electrode gold surface preparation: (A) surface cleaning; (B) probes grafting; (C) miRNA-146a perfect match formation.

For the versatility test, instead, probes of miR-34a, -29b and -125b were used for the electrode surface functionalization and relative synthetic miRNA target were used at a concentration of 1 µM. In this case, the preliminary analyses performed have a qualitative character that allowed to confirm the feasibility of the protocol used.

3.2.1.3. Electrochemical analysis

Once functionalized with probe-thiol and miRNA target, the gold working electrode was used for the sensing tests by electrochemical analysis. The miRNA-biosensor assembly and sensing performances were both electrochemically characterized by CV and EIS. The measurements were performed by using the portable potentiostat PalmSens4 (Palm Instrument) assisted by PSTrace software. An electrochemical cell was built to connect CHI101 Au electrode used as working electrode (WE), a Pt wire used as counter electrode (CE) and an Ag/AgCl electrode as reference electrode (RE). Instead, the electrochemical sensors 3 mm x 4 mm manufactured by FBK were connected *via* a connector produced in our laboratories. The measurements were carried out in drop casting mode using a solution of 5 mM ferro/ferricyanide (1:1 v/v) in 0.1 M phosphate buffer pH 6.8 as redox probe at room temperature. In the case of EIS measurements, a frequency range between 0.1 Hz and 100 KHz, 10 frequencies per decade, at an open circuit potential, with a voltage amplitude of 0.01 V, were used and the electron transfer process, $[Fe(CN)_6]^{3-} + 1e^- \rightleftarrows [Fe(CN)_6]^{4-}$, has been studied using EIS[173,174]. The experimental data obtained with the two systems described above were fitted using the PSTrace 5.10 software to a common Randles circuit, **Figure 3.16.** This equivalent circuit, which is one of the simplest possible models describing processes at the electrochemical interface, involves of an active electrolyte resistance R_S in series with the parallel combination of the double-layer capacitance constant phase element (CPE). To the above-mentioned components, the charge transfer resistance (R_{ct}) and the Warburg impedance (W) are added. The latter is related to the electron

transfer process and the diffusivity of the redox probe between the solution and the electrode surface, respectively.

Once all the main EIS experimental parameters were optimized, the analytical performances of the electrochemical cell were initially studied by measuring the variation of the signal obtained with different concentrations of miR-146a and, for versatility and cross-reactivity test, 1uM of miR-34a, miR-29b, miR-125b and US miRNA.

The goodness of the correct functioning of the biosensor was then obtained by plotting on the x-axis the four types of treated samples versus ΔR_{ct}. ΔR_{ct} was calculated by the following equation (1):

$$\Delta R_{ct} = R_{miR} - R_{p-t} (1)$$

Where R_{p-t} is the value of charge transfer resistance due to the probe and passivator immobilization on the electrode surface and R_{miR} is the charge transfer resistance measured after the perfect match formation with miR-146a.

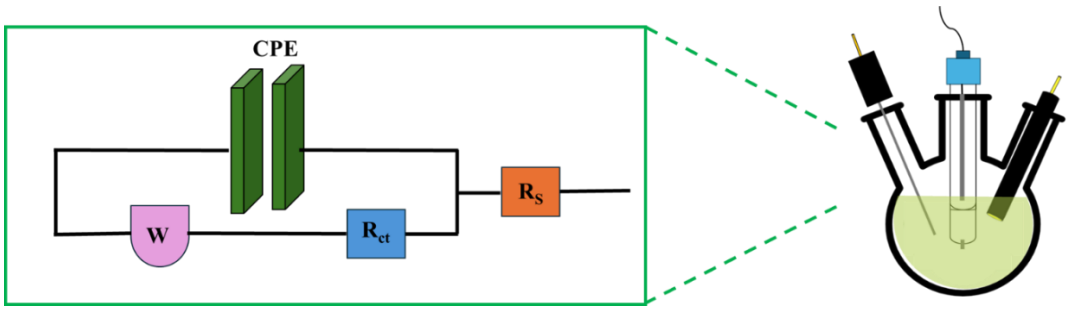

Figure 3.16. Schematic representation of equivalent Randles circuit. Rs: Ohmic resistance; R_{ct}: charge transfer resistance; W: Warburg impedance; CPE: constant phase element.

The CV measurements were performed in the range − 0.35 to + 0.6 V vs reference electrode with a scan rate of 0.1 V/s

3.2.2. Results and discussion

We have first evaluated the surface wettability via CA during the functionalization of the gold sensing biointerface. **Figure 3.17a** shows that the

CA of a bare electrode is approximately 80.76◦ ± 1.03◦, which indicates that the rough surface of the gold surface provides a relatively hydrophobic interface and which is in agreement with values found in literature[320]. The cleaning procedure caused an improvement of the hydrophilicity of interface (51.93◦ ± 3.34◦) suggesting the presence of gold oxide[321].

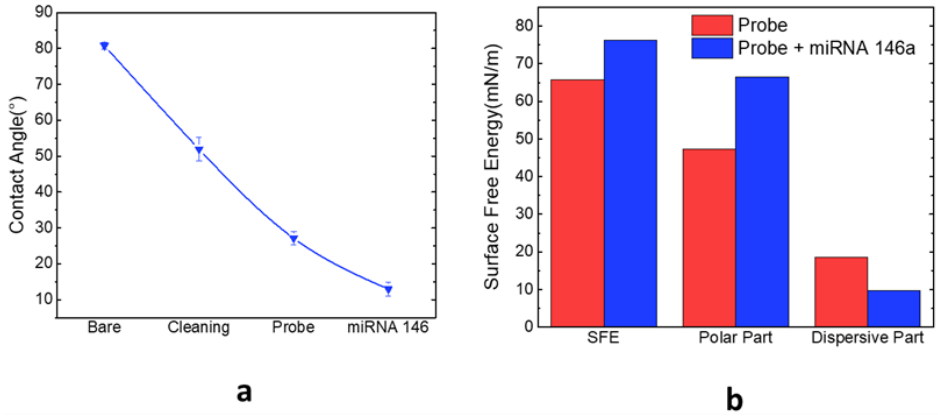

Figure 3.17. (a) CA characterization of gold surface wettability after each functionalization step. (b) SFE comparison between probes (red bar) and probes+miR146a (blue bar) modified surface.

After the anchoring of probe-thiol mix (ratio 1:10), the hydrophilicity increased (27.13◦ ± 1.77◦), due to the large presence of polar groups (the main ones are -OH and PO_4^{3-}) on the surface from the probe[185]and thiol molecule[191]. Lastly, the wettability increased after the immobilization of miRNA-146a, showing the smallest contact angle value (12.95◦ ± 1.94◦), suggesting an increase in polar groups on the surface and the successful fabrication of the miRNA146a biointerface, also confirmed by SFE analysis, **Figure 3.17b**, that reported an increase of polar part of SFE, from 47.30 mN/m to 66.52 mN/m, after the direct hybridization of probes with miR-146a target.

The CV and EIS characterization of the miRNA detection strategy is shown in **Figure 3.18**. CV and EIS were used as complementary tools to correctly

characterize both the electrochemical behaviour of the electrode/electrolyte interface at each step of functionalization and the sensing performances.

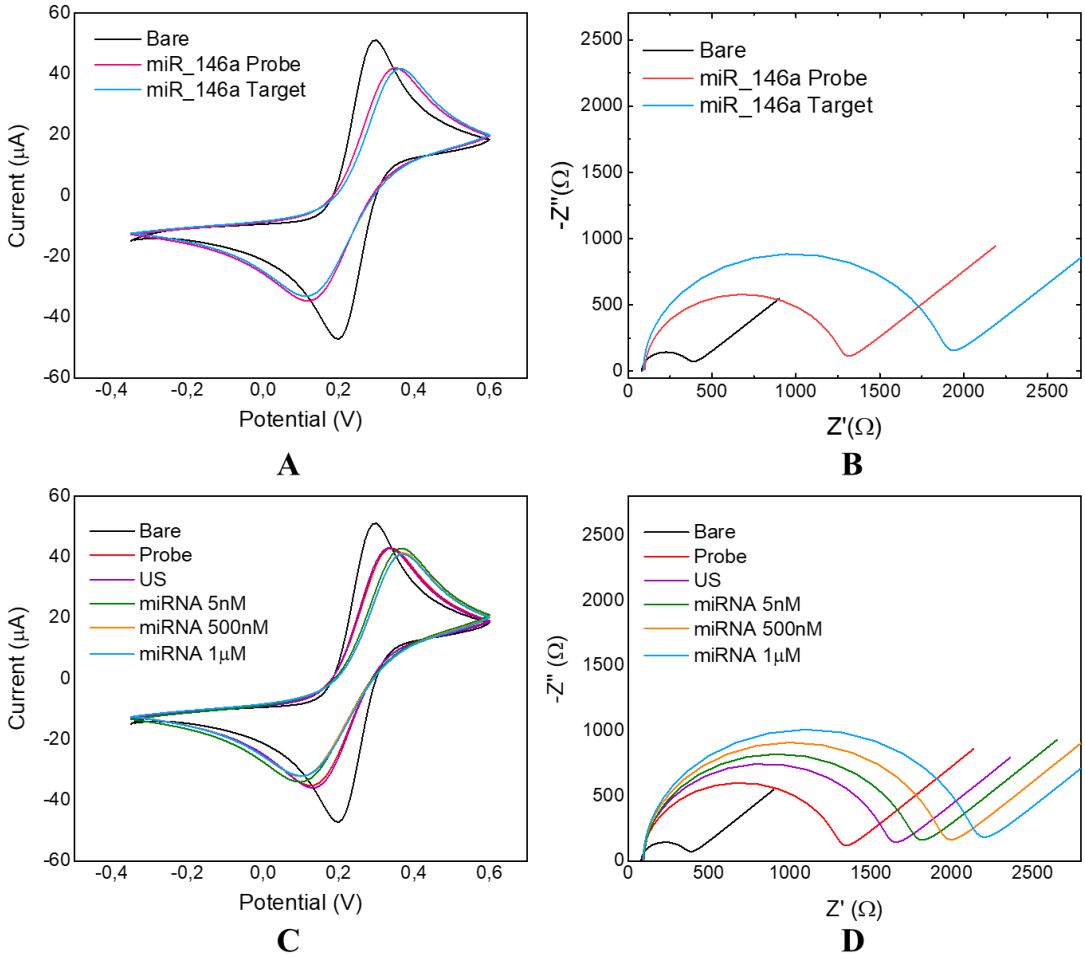

Figure 3.18. Electrochemical characterization of Au electrode interfaces during the multistep biointerface build-up. (A) Cyclic voltammograms and (B) Nyquist's Plot recorded in 5 mM $[Fe(CN)_6]^{4-/3-}$ in 0.2M Pb and analytical performance of miRNA-146a sensor C) Cyclic voltammograms and D) Nyquist's Plot.

The voltammograms reported in **Figure 3.18a** shows the effects of functionalization on conductivity and resistivity of the electrode/electrolyte interface, influencing the performance of the WE. The starting point was bare-Au, where a typical voltammogram of the electrochemically reversible Fe^{2+} and Fe^{3+} couple was obtained as both species rapidly exchange electrons. The peak-to-peak separation was around 90 mV (**Figure 3.18a**, black line). Subsequently, gold chemistry through covalent bond formation was exploited

to functionalize the gold working electrode with thiolate compounds. Then, by combining the thiol-terminated probe, described in **Table 3.1**, and the passivating molecule (6-mercapto-1-hexanol) in a ratio of 1:10, a homogeneously distributed probes array could be obtained. Indeed, the passivating molecule allows to obtain an optimal distance between the oligonucleotide chains for the subsequent formation of the perfect match with miRNA-146a 1μM, respecting the steric hindrance of DNA-miRNA duplex[191]. From the voltammograms reported in **Figure 3.18a** red line, it is possible emerged a significant decrease in the magnitude of the voltammetric peaks for the probe-thiol system, reported respectively as anodic and cathodic current peaks (I_{pa} and I_{pc}), and a significant increase in the peak-to-peak separation (ΔE = 180 mV ± 18 mV) compared to bare-Au, **Table 3.2**. This can be attributed to the highly shielding characteristic of the grafted organic layer, which gradually hinders the electron transport on the surface of the gold electrode[193].

Lastly, we proceeded with the formation of the perfect match between miR-146a and the reference probe. It is evident, **Figure 3.18a** blue line, how the perfect match between probe and miRNA produced a significant decrease in the magnitude of both voltammetric peaks (I_{pa}, I_{pc}), **Table 3.2**. This is due to a further decrease in the diffusivity of the redox probe near the gold electrode interface, resulting from the sequential immobilization on the electrode surface of the probe, the thiol and the final addition of the target miRNA. Furthermore, another validation of the perfect match formation can be observed from the increase in peak-to-peak separation (ΔE = 230 mV ± 23mV), attributable to several oligonucleotides chains addition to the dielectric surface proving the ability of this strategy to directly detect miRNAs without further amplification.

Table 3.2. Anodic and cathodic peak (Ipa and Ipc), peak-to-peak separation ΔE and Charge transfer resistance (R_{ct}), estimated for CHI101 electrode using CV and EIS in 5 mM $[Fe(CN)_6]^{4-/3-}$, in Pb pH 6.8, during miRNA-146a biointerface fabrication.

Sample:	Ipa (μA)	Ipc (μA)	ΔE (mV)	R_{ct} (Ω)
Bare	57.2 ± 0.3	- 54.54 ± 0.01	90 ± 2	150± 14
Probe_Thiol	45.7 ± 0.5	- 37.3 ± 1.3	190 ± 20	1000 ± 100
miR-146a	44.3 ± 1.0	- 33.9 ± 1.3	240 ± 25	1853 ± 100

In line with CV measurements, the Nyquist plots, **Figure 3.18b**, showed an increase in the charge transfer resistance for each step of biointerface functionalization. In detail, for bare-Au a small R_{ct}, 150 Ω, **Figure 3.18b** black line, is present, highlighting how electrons do not encounter resistance while traveling between the redox species and the electrode surface[192]. Subsequently, with the anchoring of the probe and the passivating molecule, a clear increase in the total impedance between bare-Au (R_{ct} = 150 Ω) and the probe-thiol functionalized electrode was observed (**Figure 3.18b**, red line R_{ct} = 1000.46 Ω), **Table 3.2.** This increase is ascribable to the biochemical properties of the probe that acts as a semiconductor. Furthermore, considering also the insulating properties of thiol[194], the reaction rate of the ferro/ferricyanide redox couple becomes slower, as shown by the increased peak-to-peak separation, and consequently almost all faradic currents fail to penetrate the electrode surface. Finally, also in this case further information on the formation of the perfect match with miRNA-146a 1μM was obtained through EIS analysis, **Figure 3.18b** blue line. Indeed, it is worth to note that the diameter of the semicircles in the Nyquist plot increased with the addition of the target miRNA, and consequently there was a clear increase in the total impedance between the thiol-Au probe (1000.46 ± 100 Ω) and the electrode functionalized with miRNA-146a (1660.23 ± 166 Ω). Also in this case, the semiconductor properties of the miRNA prevent all the Faraday currents from crossing the surface, further slowing down the reaction rate of the redox couple. This result demonstrated the feasibility of the proposed method and

therefore the possibility of detecting miRNA-146a electrochemically with commercial electrodes.

To furtherly test the sensitivity of the proposed method, we performed additional functionalization tests at different miRNA concentrations of miR-146a (500nM and 5nM), also including an US miRNA at 1µM, **Figure 3.18c and 3.18d**. The first results have showed an excellent selectivity of our strategy towards the miRNA-146a of our interest, in fact it cropped up a continuously decrease in the voltammetric peaks I_{pa} and I_{pc} and an increase in the peak-to-peak separation for 5nM and 500nM concentrations compared to the Au-probe-thiol system, **Figure 3.18c** and **Table 3.3**. These values are however lower than the 1µM concentration, which confirm the presence of a smaller amount of miRNA-146a on the electrode. Furthermore, the recorded R_{ct} also presented higher values than the Au-probe-thiol system, **Figure 3.18d**, as the concentration varies and consequently also the calculated ΔR_{ct} increases as a function of the concentration of miRNA-146a present in the samples, **Table 3.3**.

Table 3.3. Anodic and cathodic peak (Ipa and Ipc), peak-to-peak separation ΔE, Charge transfer resistance (R_{ct}) and ΔR_{ct} values for CHI101 electrodes obtained for the four samples analyzed using CV and EIS in 5 mM $[Fe(CN)_6]^{4-/3-}$, in Pb pH 6.8, during miRNA-146a biointerface fabrication.

Sample:	Ipa (µA)	Ipc (µA)	ΔE (mV)	R_{ct} (Ω)	ΔR_{ct} (Ω)
US	45.6 ± 4.5	- 36.3 ± 3.6	200 ± 20	1201 ± 120	200 ± 140
5 nM	45.1 ± 4.5	- 35.1 ± - 3.5	210± 21	1355 ± 130	354 ± 140
500nM	44.1 ± 4.4	- 34.5 ± - 3.4	230± 23	1650 ± 160	649 ± 170
1 µM	44.3 ± 4.4	-34.9 ± - 3.4	240 ± 24	1857 ± 180	853 ± 190

Lastly, the CV and EIS results recorded after adding an US miRNA 1 µM highlighted the specificity of our probe towards miRNA-146a and therefore the

robustness of our strategy. It is interesting to observe how the voltammetric peaks values I_{pa} and I_{pc}, the peak-to-peak separation and the recorded R_{ct} are very similar to those of the Au-probe-thiol system, **Figure 3.18c** and **3.18d** purple line. These results confirmed the almost total absence of signal coming from the US as confirmed by the calculated ΔR_{ct}, **Table 3.3**.

The promising results moved us to validate the electrochemical PCR-free method also with the miR-34a (a), miR-29b (b) and miR-125b (c) biomarkers, using the relative probes reported in **Table 3.1**.

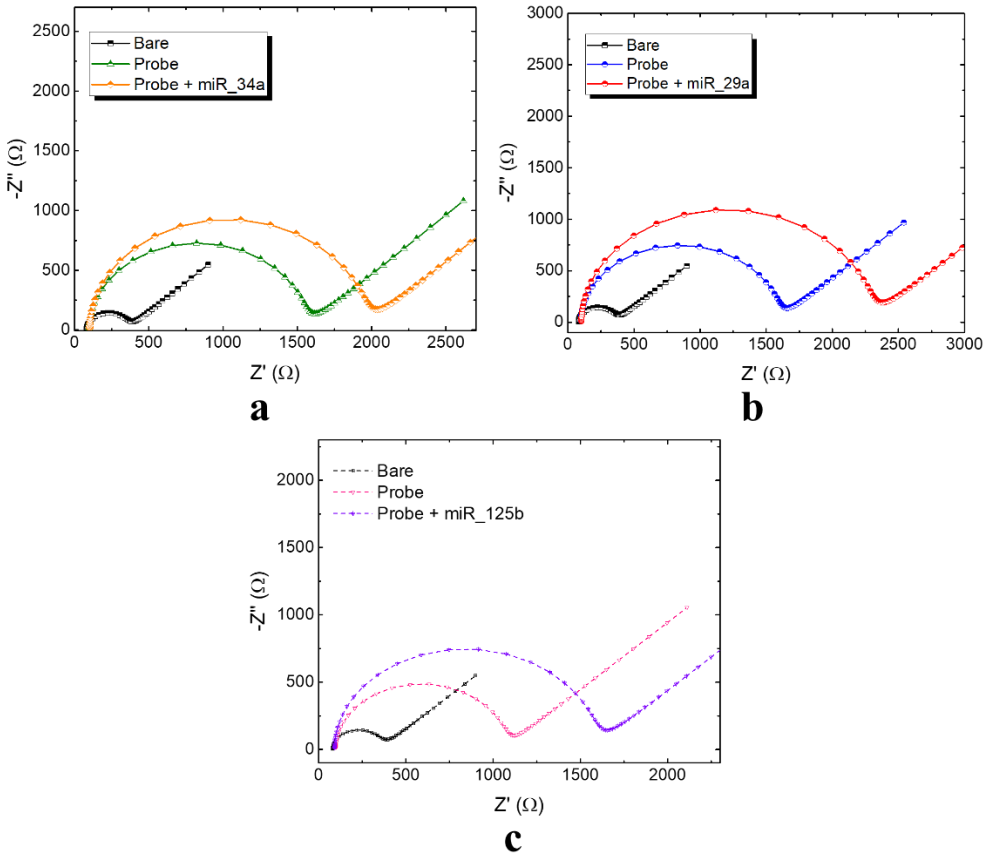

Figure 3.19. EIS analysis for PCR-free of miR-34a (a), miR-29a (b) and miR-125b (c) detection.

As shown in **Figure 3.19**, the measured resistance values confirmed the effectiveness of miRNAs PCR-free detection. Indeed, the 210 Ω resistance of bare surface raised over 1000 Ω after the probes grafting, due to the steric hindrance and first electrostatic repulsions produced between the probes and

the surface, and furtherly increased with an average gap of ~ 560 Ω after the miRNA target hybridization, as consequence of the perfect match formation and the doubled number of strands added to the surface dielectric. This led to a direct detection of miRNAs without any further amplifications by RT-qPCR.

3.2.3. Future perspectives: PCR-free sensing strategy implementation into PoC device

The developed PCR-free technology has tested in its suitability for PoC applications. The miRNA sensing interface has been functionalized on top of a miniaturized amperometric chip fabricated by FBK. The chip, reported in **Figure 3.20a**, was a 3 mm × 4 mm glass substrate patterned with 3 microelectrodes, i.e. a platinum WE and a gold CE and RE. A polycarbonate mask (**Figure 3.20b)**, having a capacity of ~50 µL, was assembled on top of the electrodes area to avoid the fluids leakage during the functionalization and testing processes. A polydimethylsiloxane (PDMS) mask completed the assembly creating the microchamber for sample inlet.

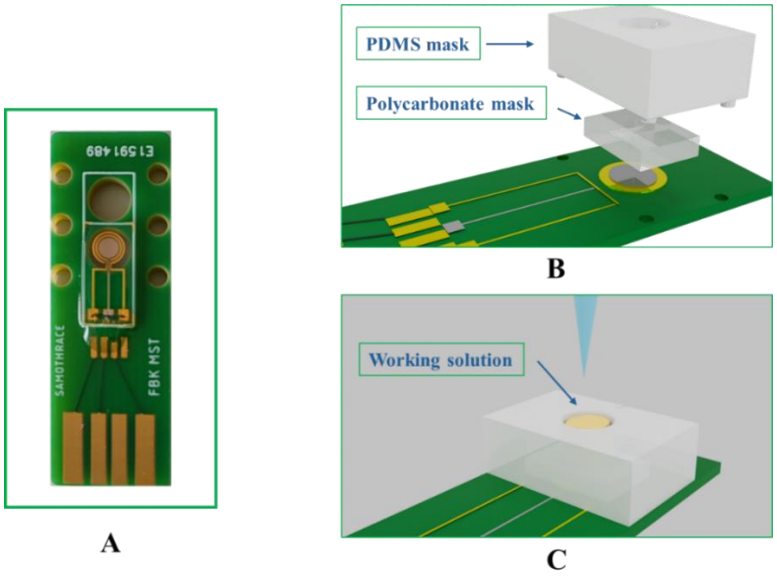

Figure 3.20. Lab-on-chip system: a) Electrochemical miniaturized sensor 3mm x 4mm; b) Lab-on-chip system assembly through PDMS and polycarbonate masks; c) Lab-on-chip system assembled for subsequent functionalization and characterizations.

The chip functionalization was performed in drop-casting mode directly inside the microchamber and incubated in a humid chamber (90% RH), volumes of about 20uL were used, as schemed in Figure 3.20c, according the experimental protocol described for the commercial gold electrode, then the same concentrations, incubation times were used. A CV and EIS analysis was first performed to electrochemically characterize the chip, and we using three different chips for the tests. The results, in **Figure 3.21a** and **b**, showed a stable current response of the electrode to the voltage scan also for different scan rate (from 0.05 Vs^{-1} to 0.3 Vs^{-1}) and a good surface active area[322]. These preliminary data were used to determine (through some manipulations of the Randle-Sevcik equation[323] and considering the large active area of the bare chip of 0.0706 cm^2) the anodic (D_A) and cathodic (D_C) diffusion coefficients (D_O) of ferricyanide using scan rates of 0.1 Vs^{-1}. The results were compared with the Konopka and McDuffie coefficients[324].

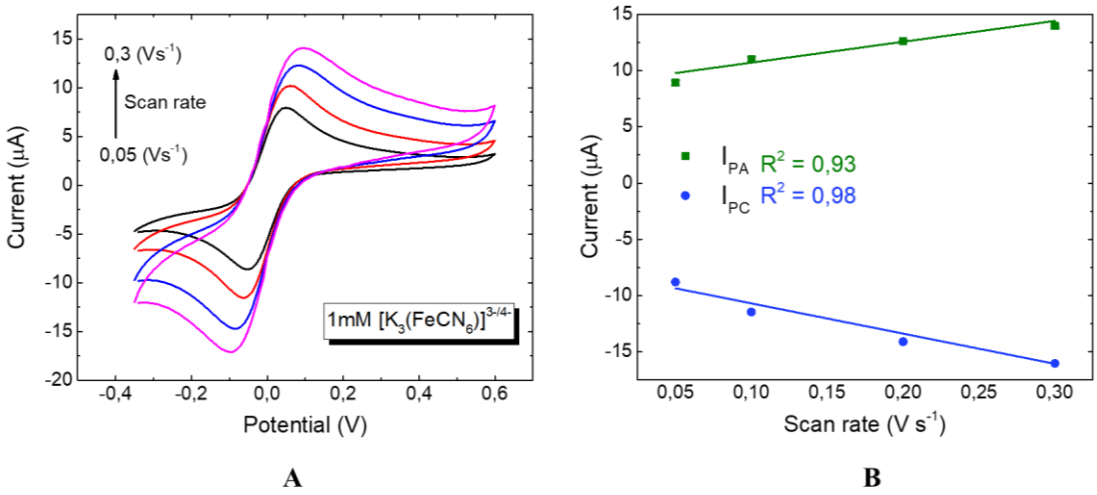

Figure 3.21. Electrochemical characterization of 3 mm x 4 mm amperometric chip. (a) Cyclic voltammograms of bare 3 mm x 4mm at various scan rates in 1 mM $[Fe(CN)_6]^{4-/3-}$ in 0.1M KCl and (b) the linear dependence between Ipa and Ipc, obtained using a 1 mM solution of $[Fe(CN)_6]^{4-/3-}$ in 0.1 M KCl, pH 7.0. The error bars in the panel are the standard deviations calculated across three independent electrodes for each condition tested.

Data reported in **Table 3.4** highlighted the bare electrode having diffusional characteristics consistent with the Konopka and McDuffie coefficients, which could be useful to obtain further information on the functionalization of the sensing surface.

Table 3.4. Diffusion coefficient (D0) estimated for 3x4 mm sensor using CV in 5 mM $[Fe(CN)_6]^{4-/3-}$, in Pb pH 6.8. Average values of at least 3 sensors are presented.

Scan rate (Vs^{-1})	D_A (cm^2/s)	D_C (cm^2/s)	D_O (cm^2/s)
0.1	$(5.21 \pm 0.01)\cdot10^{-6}$	$(4.66 \pm 0.01)\cdot10^{-6}$	$(4.93 \pm 0.01)\cdot10^{-6}$

Subsequent CV and EIS analyses were performed to test the sensing performances of the chip on the miRNA PCR-free detection. In this case, probes and synthetic target of miR-125b were used for the chip WE functionalization, done accordingly to the protocol previously described for the commercial gold electrode. We performed the electrochemical analysis using three replicates for each functionalization step.

The results, reported in **Figure 3.22a** and **b**, showed the variations of current and potential at each functionalization step. For bare Pt WE, **Figure 3.22a** black line, a typical voltammogram was obtained.

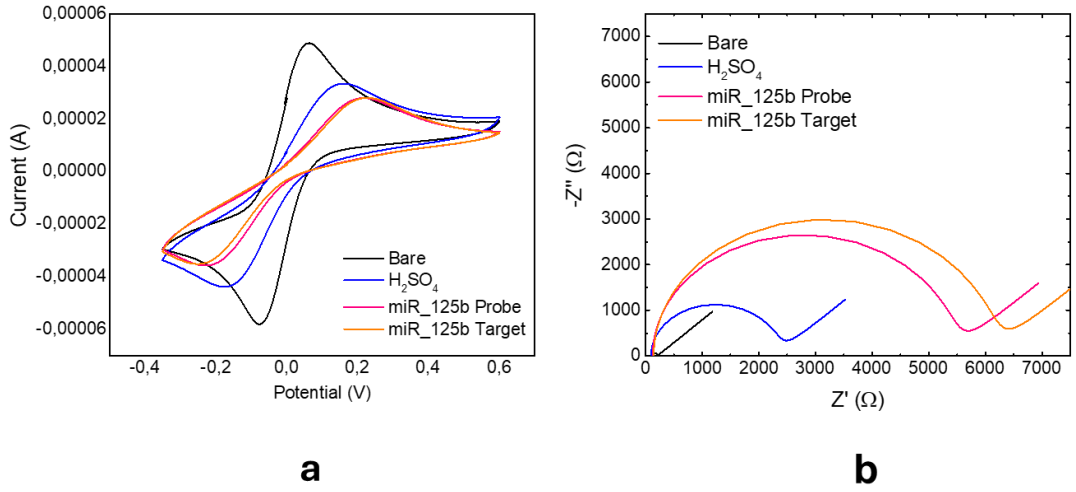

Figure 3.22. (a) Voltammogram and (b) Nyquist's plot of chip step-by-step functionalization characterization.

The treatment with sulfuric acid activated the thiol groups on the surface, consequently, modifying the WE surface electrical properties. Indeed, an increase of both ΔE and R_{ct} values, showed in **Table 3.5**, compared to the bare surface was observed. The calculated electrode active area was significantly reduced to 0.040 ± 0.002 cm^2, indicating a formation of a platinum oxide layer[325] that causes a decrease in electron transfer. The functionalization with probes and passivator **(Figure 3.22a** magenta line), then, created a semiconductor-like layer that caused a further decrease of the anodic peak, compared to the H_2SO_4 cleaned surface. This result proved the presence of an organic layer grafted on the electrode surface, which gradually hindered the electron transport on the surface of the platinum electrode a provoked a further decreased of active area to 0.030 ± 0.001 cm^2. The EIS, **Figure 3.22b**, provided further valuable information on the presence of the probe-passivant with a clear increase of total impedance (R_{ct} = 4656.7 ± 405 Ω, magenta line) compared to the sulfuric acid treatment (R_{ct}= 2379.2 ± 290 Ω, blue line). This trend of impedance was associated to the chemical-physical properties of the probe-thiol-modified WE surface, which prevented almost all the Faradaic currents from penetrating the surface (due to the high insulating properties of the thiol)[194].

Table 3.5. Anodic and cathodic peak (Ipa and Ipc), peak-to-peak separation ΔE, active surface area (A) and Charge transfer resistance (R_{ct}), estimated for 3x4 mm sensors using CV and EIS in 5 mM $[Fe(CN)_6]^{4-/3-}$, in Pb pH 6.8, during miRNA-146a sensor fabrication.

Sample	I_{pa} (μA)	I_{pc} (μA)	ΔE (mV)	A (cm^2)	R_{ct} (Ω)
Bare	68 ± 10	- 65 ± 10	102 ± 5	0.07 ± 0.01	33 ± 2
H_2SO_4	38 ± 2	- 28 ± 2	264 ± 10	0.040 ± 0.002	2379 ± 200
Probe_Thiol	28 ± 1	- 19 ± 1	362 ± 6	0.030 ± 0.001	4657 ± 400
miRNA-125a	28 ± 1	- 16 ± 1	391 ± 2	0.029 ± 0.001	5710 ± 400

Lastly, we tested the perfect match formation between the 500 nM miRNA-125b mimetic and the grafted probes. As shown in **Figure 3.22a**, there is a last slight decrease of the voltammetric peaks magnitude and the electrode active area (A = 0.0296 ± 0.001 cm^2) and an increase in the peak-to-peak separation (ΔE = 391 ± 2 mV) compared to the probe-thiol modified surface. The EIS analysis (**Figure 3.22b** orange line) supported the data. Indeed, it was measured a marked increase of the total impedance, with a ΔR_{ct} of 1022.95 Ω, as a consequence of the probes-miRNA duplex formation and the further the electrical isolation at surface. These results proved the doubled number of oligo strains added to the dielectric surface and the probes- miRNA-125b perfect match formation, thus, demonstrating the suitability of the developed PCR-free sensing method to properly work also integrated into portable chip towards future PoC applications.

CHAPTER 4

Conclusions

4. Conclusions

My Ph.D. thesis has been focused on the development of novel innovative sensing strategies for nucleic acid detection for future PoC biosensor applications. The genetic PoC are systems integrating all steps necessary for the molecular analysis such as sample preparation (extraction and purification of DNA) and detection (i.e. PCR or real time PCR) and they should be able to perform in vitro genetic analysis by unskilled personnel near to the patient, in hospital, in the physician office, clinic or home with rapid answer and low cost.

In the first chapter, types and mechanisms of electrochemical and optical biosensors have been reviewed. It has been explored the way electrochemical biosensors can quantitatively assay biochemical analytes in biological fluids, providing digital data of dynamic physiological processes for research and future healthcare applications. Optical biosensors have made also great strides in detecting a variety of chemical and biological analytes. The performances of these devices will continue to evolve due to the need for low-cost, durable, accurate and sensitive analysis in different biomedical applications. In this scenario, PCR-free approaches emerged since aim to provide an effective molecular diagnostics in a facilitate and decentralized way. These methods are designed to perform the direct detection of genetic material without the constrain to PCR amplification and bulky lab instrumentations, thus, optimizing time, costs, and portability of the analysis. Further development of these biosensors would enable routine health checks at home, thus, detecting abnormalities at an early stage and making therapies more effective. Moreover, the combination with the IoT and a high level of informatization would address the need of a real-time management of screening data and the possibility to wireless share them in a common cloud repository. This would be very useful, for example, in the infections screening to quickly register asymptomatic and symptomatic subjects and to proceed with the patient isolation, containing any risk of future pandemics. This exhaustive study of the PoC and PCR-free technologies state-of-the-art has been published in the *Advanced Healthcare Material* journal in 2023[326].

The second chapter of my Ph.D. thesis focused on the development and characterization of new molecular methodologies for the PCR-free detection of pathogen microorganisms. The sensing strategy has been designed for the high throughput molecular detection of the genetic material of SARS-CoV-2 virus, the *Pseudomonas aeruginosa* bacterium and the *Leishmania infantum* protozoan, all of which are responsible for severe human infectious diseases. A cooperative hybridization mechanism has been performed by a thiol-modified oligonucleotide sensing array functionalized on top of a commercial gold electrode. The deep characterization of developed sensing interface performed by CA, SFE and XPS analysis proved the effectiveness of each step of gold surface functionalization, giving also some hints on the surface charges properties of solid-state NAs complexations. The PCR-free sensing of all genetic targets has been, instead, performed by CV and EIS analysis, which reported analytical performances comparable to the PCR-based gold standard techniques with a LoD of 1 cps/µL and LoQ of 10 cps/µL. One of the main advantages of this sensing method is certainly the possibility to avoid further NAs amplifications keeping a high level of sensitivity and accuracy, together with the future possibility of a system integration into miniaturized chip that would allow the development of portable, adaptable and low-sample consumption biosensors. Another approach for PoC devices devoted to microorganisms detection was based on phage probes leading to possible device architecture to be implemented in miniaturized systems.

The results paved the basis for useful sensing strategies in pandemic scenarios, opening the infections screening to massive and low-resource settings applications in a PoC format. Part of this research activity was published in the *Advanced Materials and Interfaces* journal in 2024[191].

The last section of my Ph.D. thesis was devoted to the development and characterization of two biosensing strategies for the detection of other molecular targets as specific biomarkers of the Alzheimer's disease (AD).

The first type was a silicon-based biosensing technology for the AD diagnosis in human sera, relying on a sensing biointerface for the phage probes (ADPP)-

based detection of Aβ-autoantibodies produced in the advanced stages of AD. The AFM and XPS characterization confirmed the effectiveness of the silicon surface functionalization with GOPS silane and protein G (PG). The SEM and AFM inspections of both GOPS-PG-IgG and GOPS-PG-IgG-ADPP biointerfaces proved the binding of the IgGs and the ADPP to the biointerface, reporting the characteristics Y-shaped and circular fractal bodies. The CA measurements at various pH demonstrated the effectiveness of each step of functionalization together with a dependence of surface wettability upon pH that was attributed to structural arrangement of the anchored biomolecules. The sensing ability of the system, instead, was first validated with a silicon flat substrate by testing both healthy and AD human sera. Results indicate a good discrimination between AD and healthy sera, validating our biointerface for the sensing purpose. Subsequently, the functionalization was applied to a silicon miniaturized chip as first proof of concept for AD diagnosis and screening in a PoC format. Data showed a statistically significative discrimination between healthy and the AD sera and thanks to the combination with the miniaturized architecture of the silicon chip, the proposed strategy would open to a very large-scale integration toward a new frontier of decentralized biomedical diagnostics. The results of this activity were published in the *Advanced Materials and Interfaces* journal in 2023[296].

The second and last activity of the chapter focused on the development of a sensing strategy for the PCR-free detection of AD-associated miRNAs. The sensing strategy, based on the use of specific oligonucleotide probes, was able to detect miR-34a, 125b, 146a, and 29b, as important biomarkers of AD onset, directly on top of a commercial gold electrode via a perfect match with the surface array of probes and without any pre-amplification of the molecular target, thus, making the analysis faster than commercial PCR-based methods. The first CA characterization validate the effectiveness of gold surface chemical functionalization, as proved by the increase of wettability and polarity after probes and miR-146a surface binding and hybridization. The electrochemical analysis with miR-146a, instead, confirmed the high sensitivity of the sensing strategy, revealing down to 5 nM of miRNA copies. Furthermore,

by changing the probes sequences, the technology proved also to be very versatile, revealing also the 34a, 29a and 125b miRNAs, and highly selective, avoiding any false positive detection towards the US miRNA. As future perspective, the strategy was first implemented into an amperometric chip, developed by FBK, composed by three electrodes patterned on a glass substrate. The Pt WE surface of the chip was functionalized according to what done with the commercial electrode and results confirmed the suitability of PCR-free miRNA sensing strategy also for portable devices towards decentralized PoC applications.

References

1. Johnson, D. W., Pieniazek, N. J., Griffin, D. W., Misener, L. & Rose, J. B. Development of a PCR protocol for sensitive detection of Cryptosporidium oocysts in water samples. *Applied and Environmental Microbiology* **61**, 3849–3855 (1995).
2. Green, M. R. & Sambrook, J. *Molecular Cloning: A Laboratory Manual*. (Cold Spring Harbor laboratory press, Cold Spring Harbor, 2012).
3. Khehra, N., Padda, I. S. & Swift, C. J. Polymerase Chain Reaction (PCR). in *StatPearls* (StatPearls Publishing, Treasure Island (FL), 2025).
4. Madej-Kiełbik, L., Gzyra-Jagieła, K., Jóźwik-Pruska, J., Dziuba, R. & Bednarowicz, A. Biopolymer Composites with Sensors for Environmental and Medical Applications. *Materials* **15**, 7493 (2022).
5. Bhalla, N., Jolly, P., Formisano, N. & Estrela, P. Introduction to biosensors. *Essays in Biochemistry* **60**, 1–8 (2016).
6. Sharma, H. & Mutharasan, R. Review of biosensors for foodborne pathogens and toxins. *Sensors and Actuators B: Chemical* **183**, 535–549 (2013).

7. Biosensors | Free Full-Text | Recent Advances in Electrochemical Biosensors: Applications, Challenges, and Future Scope. https://www.mdpi.com/2079-6374/11/9/336.
8. Mehrotra, P. Biosensors and their applications - A review. *J Oral Biol Craniofac Res* **6**, 153–159 (2016).
9. Viswanathan, S., Radecka, H. & Radecki, J. Electrochemical biosensors for food analysis. *Monatsh Chem* **140**, 891–899 (2009).
10. Bossuyt, P. M. M., Reitsma, J. B., Linnet, K. & Moons, K. G. M. Beyond diagnostic accuracy: the clinical utility of diagnostic tests. *Clin Chem* **58**, 1636–1643 (2012).
11. Petralia, S. & Conoci, S. PCR Technologies for Point of Care Testing: Progress and Perspectives. *ACS Sens.* **2**, 876–891 (2017).
12. Rohr, U.-P. *et al.* The Value of In Vitro Diagnostic Testing in Medical Practice: A Status Report. *PLOS ONE* **11**, e0149856 (2016).
13. Diagnostic Landscape: Imaging and In Vitro Technologies. *Next Phase Newsletter* https://blog.lifesciencenation.com/2014/12/11/diagnostic-landscape-imaging-and-in-vitro-technologies/ (2014).
14. Hulanicki, A., Glab, S. & Ingman, F. Chemical sensors: definitions and classification. *Pure and Applied Chemistry* **63**, 1247–1250 (1991).
15. Nagel, B., Dellweg, H. & Gierasch, L. M. Glossary for chemists of terms used in biotechnology (IUPAC Recommendations 1992). *Pure and Applied Chemistry* **64**, 143–168 (1992).
16. Scheller, F. W., Wollenberger, U., Warsinke, A. & Lisdat, F. Research and development in biosensors. *Current Opinion in Biotechnology* **12**, 35–40 (2001).

17. Clark Jr., L. C. & Lyons, C. Electrode Systems for Continuous Monitoring in Cardiovascular Surgery. *Annals of the New York Academy of Sciences* **102**, 29–45 (1962).
18. Newman, J. D. & Turner, A. P. F. Home blood glucose biosensors: a commercial perspective. *Biosensors and Bioelectronics* **20**, 2435–2453 (2005).
19. Vo-Dinh, T. & Cullum, B. Biosensors and biochips: advances in biological and medical diagnostics. *Fresenius J Anal Chem* **366**, 540–551 (2000).
20. Piunno, P. A. E. & Krull, U. J. Trends in the development of nucleic acid biosensors for medical diagnostics. *Anal Bioanal Chem* **381**, 1004–1011 (2005).
21. Marco, M.-P. & Barceló, D. Environmental applications of analytical biosensors. *Meas. Sci. Technol.* **7**, 1547 (1996).
22. Baeumner, A. J. Biosensors for environmental pollutants and food contaminants. *Anal Bioanal Chem* **377**, 434–445 (2003).
23. Belkin, S. Microbial whole-cell sensing systems of environmental pollutants. *Curr Opin Microbiol* **6**, 206–212 (2003).
24. Rodriguez-Mozaz, S., Lopez de Alda, M. J. & Barceló, D. Biosensors as useful tools for environmental analysis and monitoring. *Anal Bioanal Chem* **386**, 1025–1041 (2006).
25. Li, C., Karadeniz, H., Canavar, E. & Erdem, A. Electrochemical sensing of label free DNA hybridization related to breast cancer 1 gene at disposable sensor platforms modified with single walled carbon nanotubes. *Electrochimica Acta* **82**, 137–142 (2012).
26. Maximizing the Signal Gain of Electrochemical-DNA Sensors | Analytical Chemistry. https://pubs.acs.org/doi/full/10.1021/acs.analchem.6b03227.

27. Fan, C., Plaxco, K. W. & Heeger, A. J. Electrochemical interrogation of conformational changes as a reagentless method for the sequence-specific detection of DNA. *Proc Natl Acad Sci U S A* **100**, 9134–9137 (2003).
28. Ferapontova, E. E. DNA Electrochemistry and Electrochemical Sensors for Nucleic Acids. *Annual Review of Analytical Chemistry* **11**, 197–218 (2018).
29. Teengam, P. *et al.* Electrochemical paper-based peptide nucleic acid biosensor for detecting human papillomavirus. *Analytica Chimica Acta* **952**, 32–40 (2017).
30. Disposable Nucleic Acid Biosensors Based on Gold Nanoparticle Probes and Lateral Flow Strip | Analytical Chemistry. https://pubs.acs.org/doi/10.1021/ac8024653.
31. Ellington, A. D. & Szostak, J. W. In vitro selection of RNA molecules that bind specific ligands. *Nature* **346**, 818–822 (1990).
32. Cho, E. J., Lee, J.-W. & Ellington, A. D. Applications of aptamers as sensors. *Annu Rev Anal Chem (Palo Alto Calif)* **2**, 241–264 (2009).
33. Wang, K., Wang, M., Ma, T., Li, W. & Zhang, H. Review on the Selection of Aptamers and Application in Paper-Based Sensors. *Biosensors (Basel)* **13**, 39 (2022).
34. A Protocol for Gold Nanoparticle-Assisted Aptamer Selection for a Small Molecule Porphyrin to Develop DNAzyme | Springer Nature Experiments. https://experiments.springernature.com/articles/10.1007/978-1-0716-2047-2_1.
35. Wu, Y., Zhan, S., Wang, L. & Zhou, P. Selection of a DNA aptamer for cadmium detection based on cationic polymer mediated aggregation of gold nanoparticles. *Analyst* **139**, 1550–1561 (2014).
36. Liu, G. *et al.* Aptamer−Nanoparticle Strip Biosensor for Sensitive Detection of Cancer Cells. *Anal. Chem.* **81**, 10013–10018 (2009).

37. Song, S., Wang, L., Li, J., Fan, C. & Zhao, J. Aptamer-based biosensors. *TrAC Trends in Analytical Chemistry* **27**, 108–117 (2008).
38. Mao, X. *et al*. Aptamer-Nanoparticle Strip Biosensor for Rapid and Sensitive Detection of Cancer Cells. *Anal Chem* **81**, 10013 (2009).
39. Sánchez-Báscones, E., Parra, F. & Lobo-Castañón, M. J. Aptamers against viruses: Selection strategies and bioanalytical applications. *TrAC Trends in Analytical Chemistry* **143**, 116349 (2021).
40. Mehrvar, M. & Abdi, M. Recent developments, characteristics, and potential applications of electrochemical biosensors. *Anal Sci* **20**, 1113–1126 (2004).
41. Palchetti, I. & Mascini, M. Electroanalytical biosensors and their potential for food pathogen and toxin detection. *Anal Bioanal Chem* **391**, 455–471 (2008).
42. Labib, M., Sargent, E. H. & Kelley, S. O. Electrochemical Methods for the Analysis of Clinically Relevant Biomolecules. *Chem. Rev.* **116**, 9001–9090 (2016).
43. Wu, J., Fu, Z., Yan, F. & Ju, H. Biomedical and clinical applications of immunoassays and immunosensors for tumor markers. *TrAC Trends in Analytical Chemistry* **26**, 679–688 (2007).
44. Minteer, S. D. Advances in Electroanalytical Chemistry. *J. Am. Chem. Soc.* **140**, 2701–2703 (2018).
45. Biosensors | Free Full-Text | Biosensors for the Detection of Antibiotics in Poultry Industry—A Review. https://www.mdpi.com/2079-6374/4/4/472.
46. Biosensors and Their Principles | IntechOpen. https://www.intechopen.com/chapters/37345.
47. Nikolaou, P. *et al*. Ultrasensitive PCR-Free detection of whole virus genome by electrochemiluminescence. *Biosensors and Bioelectronics* **209**, 114165 (2022).

48. PCR-Free Innovative Strategies for SARS-CoV-2 Detection - Calorenni - 2023 - Advanced Healthcare Materials - Wiley Online Library. https://onlinelibrary.wiley.com/doi/full/10.1002/adhm.202300512.

49. Xu, Q., Pan, Y., Li, W. & Yang, Z. Amperometric sensors. in *Fundamentals of Sensor Technology: Principles and Novel Designs* 123–145 (2023). doi:10.1016/B978-0-323-88431-0.00007-7.

50. Ju, H., Zhang, X. & Wang, J. Biosensors Based on Nanoporous Materials. in *NanoBiosensing: Principles, Development and Application* (eds. Ju, H., Zhang, X. & Wang, J.) 171–205 (Springer, New York, NY, 2011). doi:10.1007/978-1-4419-9622-0_6.

51. Kim, S.-K. *et al.* Bimetallic Nanocatalysts Immobilized in Nanoporous Hydrogels for Long-Term Robust Continuous Glucose Monitoring of Smart Contact Lens. *Advanced Materials* **34**, 2110536 (2022).

52. Huang, Y., Han, Y., Sun, J., Zhang, Y. & Han, L. Dual nanocatalysts co-decorated three-dimensional, laser-induced graphene hybrid nanomaterials integrated with a smartphone portable electrochemical system for point-of-care non-enzymatic glucose diagnosis. *Materials Today Chemistry* **24**, (2022).

53. Wu, J., Yan, F., Tang, J., Zhai, C. & Ju, H. A Disposable Multianalyte Electrochemical Immunosensor Array for Automated Simultaneous Determination of Tumor Markers. *Clinical Chemistry* **53**, 1495–1502 (2007).

54. Wu, J. *et al.* A disposable electrochemical immunosensor for flow injection immunoassay of carcinoembryonic antigen. *Biosens Bioelectron* **22**, 102–108 (2006).

55. Lubin, A. A. & Plaxco, K. W. Folding-Based Electrochemical Biosensors: The Case for Responsive Nucleic Acid Architectures. *Acc. Chem. Res.* **43**, 496–505 (2010).

56. Zhao, Y., Chen, F., Li, Q., Wang, L. & Fan, C. Isothermal Amplification of Nucleic Acids. *Chem. Rev.* **115**, 12491–12545 (2015).
57. Simmel, F. C., Yurke, B. & Singh, H. R. Principles and Applications of Nucleic Acid Strand Displacement Reactions. *Chem. Rev.* **119**, 6326–6369 (2019).
58. Dai, Y. *et al.* Exploring the Trans-Cleavage Activity of CRISPR-Cas12a (cpf1) for the Development of a Universal Electrochemical Biosensor. *Angewandte Chemie International Edition* **58**, 17399–17405 (2019).
59. Electroanalysis - Christopher Brett, Ana Maria Oliveira Brett - Oxford University Press. https://global.oup.com/academic/product/electroanalysis-9780198548164?lang=en&cc=ba.
60. Karimi-Maleh, H. *et al.* A critical review on the use of potentiometric based biosensors for biomarkers detection. *Biosensors and Bioelectronics* **184**, 113252 (2021).
61. Ding, J., Chen, Y., Wang, X. & Qin, W. Label-Free and Substrate-Free Potentiometric Aptasensing Using Polycation-Sensitive Membrane Electrodes. *Anal. Chem.* **84**, 2055–2061 (2012).
62. Nurlely, Ahmad, M., Yook Heng, L. & Ling Tan, L. Potentiometric enzyme biosensor for rapid determination of formaldehyde based on succinimide-functionalized polyacrylate ion-selective membrane. *Measurement* **175**, 109112 (2021).
63. Potentiometric Detection of DNA Hybridization using Enzyme-Induced Metallization and a Silver Ion Selective Electrode | Analytical Chemistry. https://pubs.acs.org/doi/10.1021/ac9018507.
64. Accessing analytes in biofluids for peripheral biochemical monitoring | Nature Biotechnology. https://www.nature.com/articles/s41587-019-0040-3.

65. Yu, Y., Nyein, H. Y. Y., Gao, W. & Javey, A. Flexible Electrochemical Bioelectronics: The Rise of In Situ Bioanalysis. *Advanced Materials* **32**, 1902083 (2020).
66. Song, Y., Min, J. & Gao, W. Wearable and Implantable Electronics: Moving toward Precision Therapy. *ACS Nano* **13**, 12280–12286 (2019).
67. Chimica analitica strumentale. https://www.edises.it/universitario/chimica-analitica-strumentale-411.html.
68. Yoshinobu, T. & Schöning, M. J. Light-addressable potentiometric sensors for cell monitoring and biosensing. *Current Opinion in Electrochemistry* **28**, 100727 (2021).
69. Casado, N. & Mecerreyes, D. Introduction to Redox Polymers: Classification, Characterization Methods and Main Applications.
70. Katz, E. & Willner, I. Probing Biomolecular Interactions at Conductive and Semiconductive Surfaces by Impedance Spectroscopy: Routes to Impedimetric Immunosensors, DNA-Sensors, and Enzyme Biosensors. *Electroanalysis* **15**, 913–947 (2003).
71. Wang, Y., Ye, Z. & Ying, Y. New Trends in Impedimetric Biosensors for the Detection of Foodborne Pathogenic Bacteria. *Sensors* **12**, 3449–3471 (2012).
72. Zhao, Y.-D. *et al.* DNA-modified electrodes Part 3.: spectroscopic characterization of DNA-modified gold electrodes. *Analytica Chimica Acta* **388**, 93–101 (1999).
73. Ye, S., Tonokura, K. & Koshi, M. Vibron dynamics in RDX, β-HMX and tetryl crystals. *Chemical Physics* **293**, 1–8 (2003).
74. Cortina, M., Esplandiu, M. J., Alegret, S. & del Valle, M. Urea impedimetric biosensor based on polymer degradation onto interdigitated electrodes. *Sensors and Actuators B: Chemical* **118**, 84–89 (2006).
75. Electrochemical Methods: Fundamentals and Applications, 2nd Edition | Wiley. *Wiley.com* https://www.wiley.com/en-

us/Electrochemical+Methods%3A+Fundamentals+and+Applications%2C+2nd+Edition-p-9780471043720.

76. Miao, W. Electrogenerated Chemiluminescence and Its Biorelated Applications. *Chem. Rev.* **108**, 2506–2553 (2008).
77. Liu, Z., Qi, W. & Xu, G. Recent advances in electrochemiluminescence. *Chem. Soc. Rev.* **44**, 3117–3142 (2015).
78. *Electrogenerated Chemiluminescence*. (CRC Press, Boca Raton, 2004). doi:10.1201/9780203027011.
79. Tokel, N. E. & Bard, A. J. Electrogenerated chemiluminescence. IX. Electrochemistry and emission from systems containing tris(2,2'-bipyridine)ruthenium(II) dichloride. *J. Am. Chem. Soc.* **94**, 2862–2863 (1972).
80. Electrogenerated Chemiluminescence: An Oxidative-Reduction Type ECL Reaction Sequence Using Tripropyl Amine - IOPscience. https://iopscience.iop.org/article/10.1149/1.2086171.
81. Blackburn, G. F. *et al.* Electrochemiluminescence detection for development of immunoassays and DNA probe assays for clinical diagnostics. *Clin Chem* **37**, 1534–1539 (1991).
82. Heineman, W. R., Kissinger, P. T. & Wehmeyer, K. R. Editors' Choice—Review—From Polarography to Electrochemical Biosensors: The 100-Year Quest for Selectivity and Sensitivity. *J. Electrochem. Soc.* **168**, 116504 (2021).
83. Qi, H. & Zhang, C. Electrogenerated Chemiluminescence Biosensing. *Anal. Chem.* **92**, 524–534 (2020).
84. Chen, Y. & Ding, Z. Highly sensitive analysis strategies of microRNAs based on electrochemiluminescence. *Current Opinion in Electrochemistry* **32**, 100901 (2022).

85. Kerr, E. *et al.* Amplification-free electrochemiluminescence molecular beacon-based microRNA sensing using a mobile phone for detection. *Sensors and Actuators B: Chemical* **330**, 129261 (2021).
86. Deiss, F. *et al.* Multiplexed Sandwich Immunoassays Using Electrochemiluminescence Imaging Resolved at the Single Bead Level. *J. Am. Chem. Soc.* **131**, 6088–6089 (2009).
87. Borisov, S. M. & Wolfbeis, O. S. Optical Biosensors. *Chem. Rev.* **108**, 423–461 (2008).
88. Karunakaran, C., Rajkumar, R. & Bhargava, K. Chapter 1 - Introduction to Biosensors. in *Biosensors and Bioelectronics* (eds. Karunakaran, C., Bhargava, K. & Benjamin, R.) 1–68 (Elsevier, 2015). doi:10.1016/B978-0-12-803100-1.00001-3.
89. Schäferling, M. Fluorescence-Based Biosensors. in *Encyclopedia of Analytical Chemistry* 1–52 (John Wiley & Sons, Ltd, 2016). doi:10.1002/9780470027318.a0206.pub3.
90. Damborský, P., Švitel, J. & Katrlík, J. Optical biosensors. *Essays in Biochemistry* **60**, 91–100 (2016).
91. Optical Sensors – Fundamentals. in *Chemical Sensors and Biosensors* 404–434 (John Wiley & Sons, Ltd, 2012). doi:10.1002/9781118354162.ch18.
92. Kretschmann, E. Die Bestimmung optischer Konstanten von Metallen durch Anregung von Oberflächenplasmaschwingungen. *Zeitschrift fur Physik* **241**, 313–324 (1971).
93. Liedberg, B., Nylander, C. & Lundström, I. Biosensing with surface plasmon resonance — how it all started. *Biosensors and Bioelectronics* **10**, i–ix (1995).

94. Biosensors | Free Full-Text | Label-Free Biosensors for Laboratory-Based Diagnostics of Infections: Current Achievements and New Trends. https://www.mdpi.com/2079-6374/10/2/11.

95. Wang, L. *et al.* Fluorometric determination of HIV DNA using molybdenum disulfide nanosheets and exonuclease III-assisted amplification. *Microchim Acta* **186**, 286 (2019).

96. Hirata, E. & Kiyokawa, E. Future Perspective of Single-Molecule FRET Biosensors and Intravital FRET Microscopy. *Biophysical Journal* **111**, 1103–1111 (2016).

97. Maas, M. B., Maybery, G. H. C., Perold, W. J., Neveling, D. P. & Dicks, L. M. T. Borosilicate Glass Fiber-Optic Biosensor for the Detection of Escherichia coli. *Curr Microbiol* **75**, 150–155 (2018).

98. Li, Y., Fan, Y., Zhang, L., Ma, S. & Zheng, J. Molecular recognition of functionalized polydiacetylene and its biosensor. in *International Conference on Sensors and Control Techniques (ICSC 2000)* vol. 4077 242–245 (SPIE, 2000).

99. Bekmurzayeva, A. *et al.* Label-free fiber-optic spherical tip biosensor to enable picomolar-level detection of CD44 protein. *Sci Rep* **11**, 19583 (2021).

100. Peng, C. *et al.* Optical Waveguide Refractive Index Sensor for Biochemical Sensing. *Applied Sciences* **13**, 3829 (2023).

101. Estevez, M. C., Alvarez, M. & Lechuga, L. M. Integrated optical devices for lab-on-a-chip biosensing applications. *Laser and Photonics Reviews* **6**, 463–487 (2012).

102. Kumar, M., Kumar, A. & Dwivedi, R. Ultra high sensitive integrated optical waveguide refractive index sensor based on multimode interference. *Sensors and Actuators B: Chemical* **222**, 556–561 (2016).

103. Choo, S. J. *et al.* An integrated Mach-Zehnder interferometric biosensor with a silicon oxynitride waveguide by plasma-enhanced chemical vapor deposition. *Current Applied Physics* **14**, 954–959 (2014).

104. Bahadır, E. B. & Sezgintürk, M. K. Electrochemical biosensors for hormone analyses. *Biosensors and Bioelectronics* **68**, 62–71 (2015).

105. Martínez-Máñez, R. & Sancenón, F. Fluorogenic and Chromogenic Chemosensors and Reagents for Anions. *Chem. Rev.* **103**, 4419–4476 (2003).

106. Guo, Y. *et al.* Label-free ratiometric DNA detection using two kinds of interaction-responsive emission dyes. *Biosensors and Bioelectronics* **87**, 320–324 (2017).

107. Sharma, A. *et al.* Designed Strategies for Fluorescence-Based Biosensors for the Detection of Mycotoxins. *Toxins* **10**, 197 (2018).

108. Gale, P. A. Anion receptor chemistry: highlights from 2008 and 2009. *Chem. Soc. Rev.* **39**, 3746–3771 (2010).

109. Liu, J., Cao, Z. & Lu, Y. Functional Nucleic Acid Sensors. *Chem. Rev.* **109**, 1948–1998 (2009).

110. Wu, D. *et al.* Recent progress in the development of organic dye based near-infrared fluorescence probes for metal ions. *Coordination Chemistry Reviews* **354**, 74–97 (2018).

111. Chen, P. *et al.* Multimode MicroRNA Sensing via Multiple Enzyme-Free Signal Amplification and Cation-Exchange Reaction. *ACS Appl. Mater. Interfaces* **11**, 36476–36484 (2019).

112. Gnaim, S. & Shabat, D. Activity-Based Optical Sensing Enabled by Self-Immolative Scaffolds: Monitoring of Release Events by Fluorescence or Chemiluminescence Output. *Acc. Chem. Res.* **52**, 2806–2817 (2019).

113. Wu, Z. *et al.* G-triplex based molecular beacon with duplex-specific nuclease amplification for the specific detection of microRNA. *Analyst* **144**, 5201–5206 (2019).

114. Miao, P., Wang, B., Meng, F., Yin, J. & Tang, Y. Ultrasensitive Detection of MicroRNA through Rolling Circle Amplification on a DNA Tetrahedron Decorated Electrode. *Bioconjugate Chem.* **26**, 602–607 (2015).

115. Zhang, Z. *et al.* Rolling Circle Amplification-Based Polyvalent Molecular Beacon Probe-Assisted Signal Amplification Strategies for Sensitive Detection of B16 Cells. *ACS Biomater. Sci. Eng.* **6**, 3114–3121 (2020).

116. Zhang, Y. *et al.* Detection of DNA 3'-phosphatase activity based on exonuclease III-assisted cascade recycling amplification reaction. *Talanta* **204**, 499–506 (2019).

117. Zhao, H. *et al.* Exonuclease III-assisted signal amplification strategy for sensitive fluorescence detection of polynucleotide kinase based on poly(thymine)-templated copper nanoparticles. *Analyst* **144**, 6689–6697 (2019).

118. Zhou, H. *et al.* A simple G-quadruplex molecular beacon-based biosensor for highly selective detection of microRNA. *Biosensors and Bioelectronics* **87**, 552–557 (2017).

119. Osman, A. M., Zomer, G., Laane, C. & Hilhorst, R. Comparative studies of the chemiluminescent horseradish peroxidase-catalysed peroxidation of acridan (GZ-11) and luminol reactions: Effect of pH and scavengers of reactive oxygen species on the light intensity of these systems. *Luminescence* **15**, 189–197 (2000).

120. Niwa, K. *et al.* Quantum yields and kinetics of the firefly bioluminescence reaction of beetle luciferases. *Photochemistry and Photobiology* **86**, 1046–1049 (2010).

121. Lundin, A. Optimization of the Firefly Luciferase Reaction for Analytical Purposes. in *Bioluminescence: Fundamentals and Applications in Biotechnology - Volume 2* (eds. Thouand, G. & Marks, R.) 31–62 (Springer, Berlin, Heidelberg, 2014). doi:10.1007/978-3-662-43619-6_2.

122. Das, S., Devireddy, R. & Gartia, M. R. Surface Plasmon Resonance (SPR) Sensor for Cancer Biomarker Detection. *Biosensors* **13**, 396 (2023).

123. Thakur, M. S. & Ragavan, K. V. Biosensors in food processing. *J Food Sci Technol* **50**, 625–641 (2013).

124. Kretschmann, E. & Raether, H. Notizen: Radiative Decay of Non Radiative Surface Plasmons Excited by Light. *Zeitschrift für Naturforschung A* **23**, 2135–2136 (1968).

125. Bai, H., Wang, R., Hargis, B., Lu, H. & Li, Y. A SPR Aptasensor for Detection of Avian Influenza Virus H5N1. *Sensors* **12**, 12506–12518 (2012).

126. Detection of Avian Influenza-DNA Hybridization Using Wavelength-scanning Surface Plasmon Resonance Biosensor -Journal of the Optical Society of Korea | Korea Science. http://koreascience.or.kr/article/JAKO200926835800069.page.

127. Palau, W., Masante, C., Ventura, M. & Primo, C. D. Direct evidence for RNA–RNA interactions at the 3' end of the Hepatitis C virus genome using surface plasmon resonance. *RNA* **19**, 982–991 (2013).

128. Meagher, R. J., Hatch, A. V., Renzi, R. F. & Singh, A. K. An integrated microfluidic platform for sensitive and rapid detection of biological toxins. *Lab Chip* **8**, 2046–2053 (2008).

129. Gubala, V., Harris, L. F., Ricco, A. J., Tan, M. X. & Williams, D. E. Point of Care Diagnostics: Status and Future. *Anal. Chem.* **84**, 487–515 (2012).

130. Patel, S., Nanda, R., Sahoo, S. & Mohapatra, E. Biosensors in Health Care: The Milestones Achieved in Their Development towards Lab-on-Chip-Analysis. *Biochemistry Research International* **2016**, 3130469 (2016).

131. Ahrberg, C. D., Manz, A. & Chung, B. G. Polymerase chain reaction in microfluidic devices. *Lab Chip* **16**, 3866–3884 (2016).

132. Li, Y. *et al.* Nanoporous Glass Integrated in Volumetric Bar-Chart Chip for Point-of-Care Diagnostics of Non-Small Cell Lung Cancer. *ACS Nano* **10**, 1640–1647 (2016).

133. Alhajj, M., Zubair, M. & Farhana, A. Enzyme Linked Immunosorbent Assay. in *StatPearls* (StatPearls Publishing, Treasure Island (FL), 2024).

134. Baryeh, K., Takalkar, S., Lund, M. & Liu, G. 1 - Introduction to medical biosensors for point of care applications. in *Medical Biosensors for Point of Care (POC) Applications* (ed. Narayan, R. J.) 3–25 (Woodhead Publishing, 2017). doi:10.1016/B978-0-08-100072-4.00001-0.

135. Frontiers | Label-free electrochemical immunosensor as a reliable point-of-care device for the detection of Interleukin-6 in serum samples from patients with psoriasis. https://www.frontiersin.org/journals/chemistry/articles/10.3389/fchem.2023.1251360/full.

136. Valencia, P. M., Farokhzad, O. C., Karnik, R. & Langer, R. Microfluidic technologies for accelerating the clinical translation of nanoparticles. *Nature Nanotech* **7**, 623–629 (2012).

137. Cappi, G. *et al.* Label-Free Detection of Tobramycin in Serum by Transmission-Localized Surface Plasmon Resonance. *Anal. Chem.* **87**, 5278–5285 (2015).

138. Sciuto, E. L. *et al.* Nucleic Acids Analytical Methods for Viral Infection Diagnosis: State-of-the-Art and Future Perspectives. *Biomolecules* **11**, 1585 (2021).

139. Zhao, J. *et al.* Multiplexed, rapid detection of H5N1 using a PCR-free nanoparticle-based genomic microarray assay. *BMC Biotechnol* **10**, 74 (2010).

140. Petralia, S. *et al.* An innovative chemical strategy for PCR-free genetic detection of pathogens by an integrated electrochemical biosensor. *Analyst* **142**, 2090–2093 (2017).

141. Real-Time PCR in Clinical Microbiology: Applications for Routine Laboratory Testing | Clinical Microbiology Reviews. https://journals.asm.org/doi/full/10.1128/cmr.19.1.165-256.2006.

142. Cheong, J. *et al.* Fast detection of SARS-CoV-2 RNA via the integration of plasmonic thermocycling and fluorescence detection in a portable device. *Nat Biomed Eng* **4**, 1159–1167 (2020).

143. Fan, Z. *et al.* Entropy-driven amplified electrochemiluminescence biosensor for RdRp gene of SARS-CoV-2 detection with self-assembled DNA tetrahedron scaffolds. *Biosensors and Bioelectronics* **178**, 113015 (2021).

144. Nunez-Bajo, E. *et al.* Disposable silicon-based all-in-one micro-qPCR for rapid on-site detection of pathogens. *Nat Commun* **11**, 6176 (2020).

145. Wang, C. *et al.* Point-of-care diagnostics for infectious diseases: From methods to devices. *Nano Today* **37**, 101092 (2021).

146. Arduini, F. *et al.* Electrochemical biosensors based on nanomodified screen-printed electrodes: Recent applications in clinical analysis. *TrAC Trends in Analytical Chemistry* **79**, 114–126 (2016).

147. Chan, H. N., Tan, M. J. A. & Wu, H. Point-of-care testing: Applications of 3D printing. *Lab on a Chip* **17**, 2713–2739 (2017).

148. Wen, Y., Zhuang, C., Jiang, X., Zhao, J. & Jiang, X. Searching superhard cubic phases in ternary B-C-N phase diagram using first-principles calculations. *Diamond and Related Materials* **27–28**, 14–18 (2012).

149. Leonardi, A. A. *et al.* Ultrasensitive Label- and PCR-Free Genome Detection Based on Cooperative Hybridization of Silicon Nanowires Optical Biosensors. *ACS Sens.* **3**, 1690–1697 (2018).

150. Chen, M., Ning, Z., Chen, K., Zhang, Y. & Shen, Y. Recent Advances of Electrochemiluminescent System in Bioassay. *J. Anal. Test.* **4**, 57–75 (2020).

151. Zhang, D. Y. Cooperative Hybridization of Oligonucleotides. *J. Am. Chem. Soc.* **133**, 1077–1086 (2011).

152. Ansari, A. A., Singh, R., Sumana, G. & Malhotra, B. D. Sol–gel derived nano-structured zinc oxide film for sexually transmitted disease sensor. *Analyst* **134**, 997–1002 (2009).

153. Myint, C. K. *et al.* Polymorphisms of cytochrome b gene in Leishmania parasites and their relation to types of cutaneous leishmaniasis lesions in Pakistan. *The Journal of Dermatology* **35**, 76–85 (2008).

154. Rioux, J. A. *et al.* Taxonomy of Leishmania. Use of isoenzymes. Suggestions for a new classification. *Ann Parasitol Hum Comp* **65**, 111–125 (1990).

155. Kumari, S. *et al.* Photodynamic vaccination of hamsters with inducible suicidal mutants of Leishmania amazonensis elicits immunity against visceral leishmaniasis. *European Journal of Immunology* **39**, 178–191 (2009).

156. Murray, H. W., Berman, J. D., Davies, C. R. & Saravia, N. G. Advances in leishmaniasis. *Lancet* **366**, 1561–1577 (2005).

157. Human Interleukin-32γ Plays a Protective Role in an Experimental Model of Visceral Leishmaniasis in Mice | Infection and Immunity. https://journals.asm.org/doi/full/10.1128/iai.00796-17.

158. Frontiers | Biomarkers Associated With Leishmania infantum Exposure, Infection, and Disease in Dogs. https://www.frontiersin.org/journals/cellular-and-infection-microbiology/articles/10.3389/fcimb.2018.00302/full.

159. Spear, R. C. Review of "Mathematical Models for Neglected Tropical Diseases: Essential Tools for Control and Elimination, Part B" Edited by Maria-Gloria Basáñez and Roy M. Anderson. *Parasites Vectors* **10**, 38 (2017).

160. Chappuis, F. *et al*. Visceral leishmaniasis: what are the needs for diagnosis, treatment and control? *Nat Rev Microbiol* **5**, 873–882 (2007).

161. Sundar, S. & Rai, M. Laboratory Diagnosis of Visceral Leishmaniasis. *Clinical and Vaccine Immunology* **9**, 951–958 (2002).

162. Lainson, R. Espécies neotropicais de Leishmania: uma breve revisão histórica sobre sua descoberta, ecologia e taxonomia. *Revista Pan-Amazônica de Saúde* **1**, 13–32 (2010).

163. Malmir, S. *et al*. Antibacterial properties of a bacterial cellulose CQD-TiO2 nanocomposite. *Carbohydrate Polymers* **234**, 115835 (2020).

164. Strelkova, M. V., Pacheco, R. S., Bulat, S. A. & Rakitskaya, T. A. Comparison of Some Molecular-genetic Techniques for Identification of Leishmania Circulating in Natural Foci of Zoonotic Cutaneous Leishmaniasis in the Central Asia Region. *Mem. Inst. Oswaldo Cruz* **92**, 109–114 (1997).

165. Carson, C. *et al*. Comparison of Leishmania OligoC-TesT PCR with Conventional and Real-Time PCR for Diagnosis of Canine Leishmania Infection. *J Clin Microbiol* **48**, 3325–3330 (2010).

166. Pourmadadi, M. *et al.* A glassy carbon electrode modified with reduced graphene oxide and gold nanoparticles for electrochemical aptasensing of lipopolysaccharides from Escherichia coli bacteria. *Mikrochim Acta* **186**, 787 (2019).

167. Nazari-Vanani, R., Heli, H. & Sattarahmady, N. An impedimetric genosensor for *Leishmania infantum* based on electrodeposited cadmium sulfide nanosheets. *Talanta* **217**, 121080 (2020).

168. Mohan, S., Srivastava, P., Maheshwari, S. N., Sundar, S. & Prakash, R. Nano-structured nickel oxide based DNA biosensor for detection of visceral leishmaniasis (Kala-azar). *Analyst* **136**, 2845–2851 (2011).

169. Mary, C., Faraut, F., Lascombe, L. & Dumon, H. Quantification of Leishmania infantum DNA by a Real-Time PCR Assay with High Sensitivity. *Journal of Clinical Microbiology* **42**, 5249–5255 (2004).

170. Camacho, E. *et al.* Leishmania Mitochondrial Genomes: Maxicircle Structure and Heterogeneity of Minicircles. *Genes (Basel)* **10**, 758 (2019).

171. Owens, D. K. & Wendt, R. C. Estimation of the surface free energy of polymers. *Journal of Applied Polymer Science* **13**, 1741–1747 (1969).

172. Fowkes, F. M. ATTRACTIVE FORCES AT INTERFACES. *Ind. Eng. Chem.* **56**, 40–52 (1964).

173. Randviir, E. P. A cross examination of electron transfer rate constants for carbon screen-printed electrodes using Electrochemical Impedance Spectroscopy and cyclic voltammetry. *Electrochimica Acta* **286**, 179–186 (2018).

174. Nicholson, R. S. & Shain, Irving. Theory of Stationary Electrode Polarography. Single Scan and Cyclic Methods Applied to Reversible, Irreversible, and Kinetic Systems. *Anal. Chem.* **36**, 706–723 (1964).

175. Petralia, S. & Conoci, S. PCR Technologies for Point of Care Testing: Progress and Perspectives. *ACS Sens.* **2**, 876–891 (2017).

176. Salathiel, R. A. Oil Recovery by Surface Film Drainage In Mixed-Wettability Rocks. *Journal of Petroleum Technology* **25**, 1216–1224 (1973).

177. Tanaka, T., Lee, J. & Scheller, P. R. Chapter 1.5 - Interfacial Free Energy and Wettability. in *Treatise on Process Metallurgy* (ed. Seetharaman, S.) 61–77 (Elsevier, Boston, 2014). doi:10.1016/B978-0-08-096984-8.00025-2.

178. Zhou, Y.-N., Li, J.-J. & Luo, Z.-H. Toward efficient water/oil separation material: Effect of copolymer composition on pH-responsive wettability and separation performance. *AIChE Journal* **62**, 1758–1771 (2016).

179. Gu, H. *et al.* Investigation on contact angle measurement methods and wettability transition of porous surfaces. *Surface and Coatings Technology* **292**, 72–77 (2016).

180. van Oss, C. J. Chapter Two - The Apolar and Polar Properties of Liquid Water and Other Condensed-Phase Materials. in *Interface Science and Technology* (ed. van Oss, C. J.) vol. 16 13–30 (Elsevier, 2008).

181. Tsai, H.-Y. *et al.* Surface Wettability and Electrical Resistance Analysis of Droplets on Indium-Tin-Oxide Glass Fabricated Using an Ultraviolet Laser System. *Micromachines (Basel)* **12**, 44 (2021).

182. Ismail, M. F., Islam, M. A., Khorshidi, B. & Sadrzadeh, M. Prediction of surface charge properties on the basis of contact angle titration models. *Materials Chemistry and Physics* **258**, 123933 (2021).

183. Jin, M., Thomsen, F., Skrivanek, T. & Willers, T. Why Test Inks Cannot Tell the Whole Truth about Surface Free Energy of Solids. in *Advances in Contact Angle,*

Wettability and Adhesion 419–438 (John Wiley & Sons, Ltd, 2015). doi:10.1002/9781119117018.ch17.

184. Petralia, S., Forte, G., Zimbone, M. & Conoci, S. The cooperative interaction of triplex forming oligonucleotides on DNA-triplex formation at electrode surface: Molecular dynamics studies and experimental evidences. *Colloids and Surfaces B: Biointerfaces* **187**, (2020).

185. Bergese, P., Oliviero, G., Colombo, I. & Depero, L. E. Molecular Recognition by Contact Angle: Proof of Concept with DNA Hybridization. *Langmuir* **25**, 4271–4273 (2009).

186. Xia, F., Zhu, Y., Feng, L. & Jiang, L. Smart responsive surfaces switching reversibly between super-hydrophobicity and super-hydrophilicity. *Soft Matter* **5**, 275–281 (2009).

187. Virga, E., Spruijt, E., de Vos, W. M. & Biesheuvel, P. M. Wettability of Amphoteric Surfaces: The Effect of pH and Ionic Strength on Surface Ionization and Wetting. *Langmuir* **34**, 15174–15180 (2018).

188. The Dynamic Surface Tension of Water | The Journal of Physical Chemistry Letters. https://pubs.acs.org/doi/10.1021/acs.jpclett.7b00267.

189. Kosmulski, M. pH-dependent surface charging and points of zero charge. IV. Update and new approach. *Journal of Colloid and Interface Science* **337**, 439–448 (2009).

190. Spatially resolved electrochemiluminescence through a chemical lens - Chemical Science (RSC Publishing). https://pubs.rsc.org/en/content/articlelanding/2020/sc/d0sc04210b.

191. Calorenni, P. *et al.* Advanced DNA–Gold Biointerface for PCR-Free Molecular Detection of Leishmania infantum. *Advanced Materials Interfaces* **n/a**, 2400642.

192. Macdonald, J. R. *et al*. *Impedance Spectroscopy: Theory, Experiment, and Applications, Third Edition*. 424–458 (John Wiley & Sons, 2018).

193. Malvano, F., Albanese, D., Pilloton, R., Di Matteo, M. & Crescitelli, A. A New Label-Free Impedimetric Affinity Sensor Based on Cholinesterases for Detection of Organophosphorous and Carbamic Pesticides in Food Samples: Impedimetric Versus Amperometric Detection. *Food and Bioprocess Technology* **10**, 1834–1843 (2017).

194. Insulating Properties of Self-Assembled Monolayers Monitored by Impedance Spectroscopy | Langmuir. https://pubs.acs.org/doi/full/10.1021/la991328c.

195. Ovchinnikova, S. & Aleksandrova, T. Influence of the nature of the alkanethiol terminal group on the electrochemical stability and blocking ability of self-assembled nanofilms on Au electrode. *MATEC Web Conf.* **340**, 01013 (2021).

196. Yuan, H. *et al*. High-Density Carrier Accumulation in ZnO Field-Effect Transistors Gated by Electric Double Layers of Ionic Liquids. *Advanced Functional Materials* **19**, 1046–1053 (2009).

197. Panneer Selvam, A. & Prasad, S. Nanosensor Electrical Immunoassay for Quantitative Detection of NT-pro Brain Natriuretic Peptide. *Future Cardiology* **9**, 137–147 (2013).

198. Munje, R. D., Muthukumar, S., Panneer Selvam, A. & Prasad, S. Flexible nanoporous tunable electrical double layer biosensors for sweat diagnostics. *Sci Rep* **5**, 14586 (2015).

199. Tsukuda, S. & Watashi, K. Hepatitis B virus biology and life cycle. *Antiviral Research* **182**, 104925 (2020).

200. Gorbalenya, A. E. *et al.* The species Severe acute respiratory syndrome-related coronavirus: classifying 2019-nCoV and naming it SARS-CoV-2. *Nat Microbiol* **5**, 536–544 (2020).

201. Wu, F. *et al.* A new coronavirus associated with human respiratory disease in China. *Nature* **579**, 265–269 (2020).

202. Zhou, P. *et al.* A pneumonia outbreak associated with a new coronavirus of probable bat origin. *Nature* **579**, 270–273 (2020).

203. Fakhruddin, B. (SHM), Blanchard, K. & Ragupathy, D. Are we there yet? The transition from response to recovery for the COVID-19 pandemic. *Progress in Disaster Science* **7**, 100102 (2020).

204. Coronavirus Disease (COVID-19) Situation Reports. https://www.who.int/emergencies/diseases/novel-coronavirus-2019/situation-reports.

205. Tahamtan, A. & Ardebili, A. Real-time RT-PCR in COVID-19 detection: issues affecting the results. *Expert Review of Molecular Diagnostics* **20**, 453–454 (2020).

206. Jiang, X., Rayner, S. & Luo, M.-H. Does SARS-CoV-2 has a longer incubation period than SARS and MERS? *Journal of Medical Virology* **92**, 476–478 (2020).

207. Rockx, B. *et al.* Comparative pathogenesis of COVID-19, MERS, and SARS in a nonhuman primate model. *Science* **368**, 1012–1015 (2020).

208. Rizzo, M. G. *et al.* Rapid detection of bacterial pathogens in blood through engineered phages-beads and integrated Real-Time PCR into MicroChip. *Sensors and Actuators B: Chemical* **329**, 129227 (2021).

209. Cassaniti, I. *et al.* Performance of VivaDiag COVID-19 IgM/IgG Rapid Test is inadequate for diagnosis of COVID-19 in acute patients referring to emergency room department. *Journal of Medical Virology* **92**, 1724–1727 (2020).

210. Cao, B. *et al.* Development of magnetic sensor technologies for point-of-care testing: Fundamentals, methodologies and applications. *Sensors and Actuators A: Physical* **312**, 112130 (2020).

211. Wöhnert, J. *et al.* Direct identification of NH···N hydrogen bonds in non-canonical base pairs of RNA by NMR spectroscopy. (2017).

212. Kerber, S. J. *et al.* The nature of hydrogen in x-ray photoelectron spectroscopy: General patterns from hydroxides to hydrogen bonding. *Journal of Vacuum Science & Technology A* **14**, 1314–1320 (1996).

213. Kumar, M. S. *et al.* Electrochemical sensing of SARS-CoV-2 amplicons with PCB electrodes. *Sensors and Actuators B: Chemical* **343**, 130169 (2021).

214. Mujica, M. L. *et al.* Impedimetric and amperometric genosensors for the highly sensitive quantification of SARS-CoV-2 nucleic acid using an avidin-functionalized multi-walled carbon nanotubes biocapture platform. *Biosensors and Bioelectronics: X* **12**, 100222 (2022).

215. İnce, F. M., Özcan, N. & Akpolat, N. Pseudomonas aeruginosa; Virulence Factors and Host Defense Mechanisms. *IAMR* **15**, 48–62 (2023).

216. Alatraktchi, F. A., Svendsen, W. E. & Molin, S. Electrochemical Detection of Pyocyanin as a Biomarker for Pseudomonas aeruginosa: A Focused Review. *Sensors* **20**, 5218 (2020).

217. Hall, S. *et al.* Cellular Effects of Pyocyanin, a Secreted Virulence Factor of Pseudomonas aeruginosa. *Toxins* **8**, 236 (2016).

218. Tran, C. S. *et al.* Host Cell Polarity Proteins Participate in Innate Immunity to Pseudomonas aeruginosa Infection. *Cell Host & Microbe* **15**, 636–643 (2014).

219. Mapes, A. C., Trautner, B. W., Liao, K. S. & Ramig, R. F. Development of expanded host range phage active on biofilms of multi-drug resistant Pseudomonas aeruginosa. *Bacteriophage* **6**, e1096995 (2016).

220. Das, T. Pseudomonas aeruginosa Secreted Biomolecules and Their Diverse Functions in Biofilm Formation and Virulence. in *Pseudomonas aeruginosa - Biofilm Formation, Infections and Treatments* (IntechOpen, 2021). doi:10.5772/intechopen.96866.

221. Rajapaksha, P. *et al.* A review of methods for the detection of pathogenic microorganisms. *Analyst* **144**, 396–411 (2019).

222. Goluch, E. D. Microbial Identification Using Electrochemical Detection of Metabolites. *Trends in Biotechnology* **35**, 1125–1128 (2017).

223. Moradali, M. F., Ghods, S. & Rehm, B. H. A. Pseudomonas aeruginosa Lifestyle: A Paradigm for Adaptation, Survival, and Persistence. *Front. Cell. Infect. Microbiol.* **7**, (2017).

224. Selim, S., El Kholy, I., Hagagy, N., El Alfay, S. & Aziz, M. A. Rapid identification of Pseudomonas aeruginosa by pulsed-field gel electrophoresis. *Biotechnology & Biotechnological Equipment* **29**, 152–156 (2015).

225. Schneider, S. *et al.* Main Metabolites of Pseudomonas aeruginosa: A Study of Electrochemical Properties. *Sensors* **22**, 4694 (2022).

226. Electrochemical detection of Pseudomonas in wound exudate samples from patients with chronic wounds - Sismaet - 2016 - Wound Repair and Regeneration - Wiley Online Library. https://onlinelibrary.wiley.com/doi/full/10.1111/wrr.12414?casa_token=iKC8awV0V4UAAAAA%3AmDuhTTrGRIxYfNj-gFS8r8nNUPzOvedn6Emvr8uVwqPYZtVRzxS6kRC8D-fT1VoY5SP49UgVXSt4YIw.

227. Rhamnolipids are conserved biosurfactants molecules: implications for their biotechnological potential | Applied Microbiology and Biotechnology. https://link.springer.com/article/10.1007/s00253-013-4876-z.

228. Roushani, M., Sarabaegi, M. & Pourahmad, F. Impedimetric aptasensor for Pseudomonas aeruginosa by using a glassy carbon electrode modified with silver nanoparticles. *Microchim Acta* **186**, 725 (2019).

229. Giménez-Lirola, L. G. *et al.* Simultaneous Detection of Antibodies against Apx Toxins ApxI, ApxII, ApxIII, and ApxIV in Pigs with Known and Unknown Actinobacillus pleuropneumoniae Exposure Using a Multiplexing Liquid Array Platform. *Clin Vaccine Immunol* **21**, 85–95 (2014).

230. Sen, A., Harvey, T. & Clausen, J. A microsystem for extraction, capture and detection of E-coli O157:H7. *Biomed Microdevices* **13**, 705–715 (2011).

231. Aydin, M. *et al.* Rapid and Sensitive Detection of *Escherichia coli* O157:H7 in Milk and Ground Beef Using Magnetic Bead–Based Immunoassay Coupled with Tyramide Signal Amplification. *Journal of Food Protection* **77**, 100–105 (2014).

232. The Overview of Phage display. *CUSABIO* https://www.cusabio.com/c-20680.html.

233. Cwirla, S. E., Peters, E. A., Barrett, R. W. & Dower, W. J. Peptides on phage: a vast library of peptides for identifying ligands. *Proc Natl Acad Sci U S A* **87**, 6378–6382 (1990).

234. Integrated Electrochemical Microsystems for Genetic Detection of Pathogens at the Point of Care | Accounts of Chemical Research. https://pubs.acs.org/doi/10.1021/ar500456w.

235. Zhang, J., Lan, T. & Lu, Y. Translating *in vitro* diagnostics from centralized laboratories to point-of-care locations using commercially-available handheld meters. *TrAC Trends in Analytical Chemistry* **124**, 115782 (2020).

236. Loncaric, C., Tang, Y., Ho, C., Parameswaran, M. A. & Yu, H.-Z. A USB-based electrochemical biosensor prototype for point-of-care diagnosis. *Sensors and Actuators B: Chemical* **161**, 908–913 (2012).

237. Arumugam, S., Colburn, D. A. M. & Sia, S. K. Biosensors for Personal Mobile Health: A System Architecture Perspective. *Advanced Materials Technologies* **5**, 1900720 (2020).

238. Cui, Y. Wireless Biological Electronic Sensors. *Sensors* **17**, 2289 (2017).

239. Choudhuri, A., Chatterjee, J. M. & Garg, S. Chapter 6 - Internet of Things in Healthcare: A Brief Overview. in *Internet of Things in Biomedical Engineering* (eds. Balas, V. E., Son, L. H., Jha, S., Khari, M. & Kumar, R.) 131–160 (Academic Press, 2019). doi:10.1016/B978-0-12-817356-5.00008-5.

240. Ganesh, H. V. S., Chow, A. M. & Kerman, K. Recent advances in biosensors for neurodegenerative disease detection. *TrAC Trends in Analytical Chemistry* **79**, 363–370 (2016).

241. Kaushik, A., Jayant, R. D., Tiwari, S., Vashist, A. & Nair, M. Nano-biosensors to detect beta-amyloid for Alzheimer's disease management. *Biosensors and Bioelectronics* **80**, 273–287 (2016).

242. Brookmeyer, R., Johnson, E., Ziegler-Graham, K. & Arrighi, H. M. Forecasting the global burden of Alzheimer's disease. *Alzheimers Dement* **3**, 186–191 (2007).

243. Nichols, E. *et al.* Global, regional, and national burden of Alzheimer's disease and other dementias, 1990–2016: a systematic analysis for the Global Burden of Disease Study 2016. *The Lancet Neurology* **18**, 88–106 (2019).

244. Ramin, M., Li, Y., Chang, W.-T., Shaw, H. & Rao, Y. The peacefulness gene promotes aggression in Drosophila. *Mol Brain* **12**, 1 (2019).

245. Serrano-Pozo, A., Frosch, M. P., Masliah, E. & Hyman, B. T. Neuropathological Alterations in Alzheimer Disease. *Cold Spring Harb Perspect Med* **1**, a006189 (2011).

246. Tokel, O., Inci, F. & Demirci, U. Advances in Plasmonic Technologies for Point of Care Applications. *Chem. Rev.* **114**, 5728–5752 (2014).

247. Kim, H., Lee, J. U., Song, S., Kim, S. & Sim, S. J. A shape-code nanoplasmonic biosensor for multiplex detection of Alzheimer's disease biomarkers. *Biosensors and Bioelectronics* **101**, 96–102 (2018).

248. Toyos-Rodríguez, C., García-Alonso, F. J. & de la Escosura-Muñiz, A. Electrochemical Biosensors Based on Nanomaterials for Early Detection of Alzheimer's Disease. *Sensors* **20**, 4748 (2020).

249. Humpel, C. Identifying and validating biomarkers for Alzheimer's disease. *Trends in Biotechnology* **29**, 26–32 (2011).

250. O'Bryant, S. E. *et al.* Guidelines for the standardization of preanalytic variables for blood-based biomarker studies in Alzheimer's disease research. *Alzheimer's & Dementia* **11**, 549–560 (2015).

251. Kim, Y. H. *et al.* Amyloid beta in nasal secretions may be a potential biomarker of Alzheimer's disease. *Sci Rep* **9**, 4966 (2019).

252. Comparative analyses of plasma amyloid-β levels in heterogeneous and monomerized states by interdigitated microelectrode sensor system | Science Advances. https://www.science.org/doi/full/10.1126/sciadv.aav1388?rfr_dat=cr_pub++0pubmed&url_ver=Z39.88-2003&rfr_id=ori%3Arid%3Acrossref.org.

253. Yoo, S.-J. *et al.* Longitudinal profiling of oligomeric Aβ in human nasal discharge reflecting cognitive decline in probable Alzheimer's disease. *Sci Rep* **10**, 11234 (2020).

254. Cerebrospinal fluid and plasma biomarkers in Alzheimer disease | Nature Reviews Neurology. https://www.nature.com/articles/nrneurol.2010.4.

255. Barthélemy, N. R. *et al.* A soluble phosphorylated tau signature links tau, amyloid and the evolution of stages of dominantly inherited Alzheimer's disease. *Nat Med* **26**, 398–407 (2020).

256. Thal, L. J. *et al.* The role of biomarkers in clinical trials for Alzheimer disease. *Alzheimer Dis Assoc Disord* **20**, 6–15 (2006).

257. SISTEMI BIOTECNOLOGICI INNOVATIVI PER LA RILEVAZIONE DI ANALITI CELLULARI O MOLECOLARI. https://www.knowledge-share.eu/it/brevetti/sistemi-biotecnologici-innovativi-per-la-rilevazione-di-analiti-cellulari-o-molecolari/.

258. Rizzo, M. G. *et al.* A Novel Serum-Based Diagnosis of Alzheimer's Disease Using an Advanced Phage-Based Biochip. *Advanced Science* **10**, 2301650 (2023).

259. De Plano, L. M. *et al.* Innovative IgG Biomarkers Based on Phage Display Microbial Amyloid Mimotope for State and Stage Diagnosis in Alzheimer's Disease. *ACS Chem. Neurosci.* **11**, 1013–1026 (2020).

260. Gustaw, K. A. *et al.* Antigen–antibody dissociation in Alzheimer disease: a novel approach to diagnosis. *Journal of Neurochemistry* **106**, 1350–1356 (2008).

261. Gustaw-Rothenberg, K. A. *et al.* Dissociated amyloid-β antibody levels as a serum biomarker for the progression of Alzheimer's disease: A population-based study. *Experimental Gerontology* **45**, 47–52 (2010).

262. Tan, L. *et al.* Circulating miR-125b as a biomarker of Alzheimer's disease. *Journal of the Neurological Sciences* **336**, 52–56 (2014).

263. Liu, S. *et al.* MicroRNAs in Alzheimer's disease: Potential diagnostic markers and therapeutic targets. *Biomed Pharmacother* **148**, 112681 (2022).

264. Bazrgar, M., Khodabakhsh, P., Prudencio, M., Mohagheghi, F. & Ahmadiani, A. The role of microRNA-34 family in Alzheimer's disease: A potential molecular link between neurodegeneration and metabolic disorders. *Pharmacol Res* **172**, 105805 (2021).

265. Kesici, E., Eksin, E. & Erdem, A. An Impedimetric Biosensor Based on Ionic Liquid-Modified Graphite Electrodes Developed for microRNA-34a Detection. *Sensors* **18**, 2868 (2018).

266. Congur, G., Eksin, E. & Erdem, A. Impedimetric Detection of microRNA at Graphene Oxide Modified Sensors. *Electrochimica Acta* **172**, 20–27 (2015).

267. Pereira, R. L., Oliveira, D., Pêgo, A. P., Santos, S. D. & Moreira, F. T. C. Electrochemical miRNA-34a-based biosensor for the diagnosis of Alzheimer's disease. *Bioelectrochemistry* **154**, 108553 (2023).

268. Chiavaioli, F. *et al.* Ultrahigh Sensitive Detection of Tau Protein as Alzheimer's Biomarker via Microfluidics and Nanofunctionalized Optical Fiber Sensors. *Advanced Photonics Research* **3**, 2200044 (2022).

269. Liu, L., Xia, N. & Wang, J. Potential applications of SPR in early diagnosis and progression of Alzheimer's disease. *RSC Adv.* **2**, 2200 (2012).

270. A Localized Surface Plasmon Resonance Biosensor: First Steps toward an Assay for Alzheimer's Disease | Nano Letters. https://pubs.acs.org/doi/10.1021/nl049670j?src=getftr.

271. Vestergaard, M., Kerman, K., Kim, D.-K., Hiep, H. M. & Tamiya, E. Detection of Alzheimer's tau protein using localised surface plasmon resonance-based immunochip. *Talanta* **74**, 1038–1042 (2008).

272. Vestergaard, M. *et al.* A Rapid Label-Free Electrochemical Detection and Kinetic Study of Alzheimer's Amyloid Beta Aggregation. *J. Am. Chem. Soc.* **127**, 11892–11893 (2005).

273. Vestergaard, M., Kerman, K. & Tamiya, E. An overview of label-free electrochemical protein sensors. *Sensors* **7**, 3442–3458 (2007).

274. Scott, J. K. & Smith, G. P. Searching for Peptide Ligands with an Epitope Library. *Science* **249**, 386–390 (1990).

275. Weng, X. *et al.* Screening serum biomarker of knee osteoarthritis using a phage display technique. *Clinical Biochemistry* **45**, 303–308 (2012).

276. Talwar, H. *et al.* Detection of Cystic Fibrosis Serological Biomarkers Using a T7 Phage Display Library. *Sci Rep* **7**, 17745 (2017).

277. Screening serum biomarkers for early primary hepatocellular carcinoma using a phage display technique - Zhang - 2011 - Journal of Clinical Laboratory Analysis - Wiley Online Library. https://onlinelibrary.wiley.com/doi/10.1002/jcla.20491.

278. Elayadi, A. N. *et al.* A Peptide Selected by Biopanning Identifies the Integrin αvβ6 as a Prognostic Biomarker for Nonsmall Cell Lung Cancer. *Cancer Research* **67**, 5889–5895 (2007).

279. Felici, F., Castagnoli, L., Musacchio, A., Jappelli, R. & Cesareni, G. Selection of antibody ligands from a large library of oligopeptides expressed on a multivalent exposition vector. *Journal of Molecular Biology* **222**, 301–310 (1991).

280. McGuire, M. J., Li, S. & Brown, K. C. Biopanning of Phage Displayed Peptide Libraries for the Isolation of Cell-Specific Ligands. in *Biosensors and Biodetection: Methods and Protocols: Electrochemical and Mechanical Detectors, Lateral Flow and Ligands for Biosensors* (eds. Rasooly, A. & Herold, K. E.) 291–321 (Humana Press, Totowa, NJ, 2009). doi:10.1007/978-1-60327-569-9_18.

281. Guliy, O. I., Evstigneeva, S. S. & Dykman, L. A. Recombinant antibodies by phage display for bioanalytical applications. *Biosensors and Bioelectronics* **222**, 114909 (2023).

282. Pande, J., Szewczyk, M. M. & Grover, A. K. Phage display: Concept, innovations, applications and future. *Biotechnology Advances* **28**, 849–858 (2010).

283. Chang, C. *et al.* Engineered M13 phage as a novel therapeutic bionanomaterial for clinical applications: From tissue regeneration to cancer therapy. *Materials Today Bio* **20**, 100612 (2023).

284. Aliakbar Ahovan, Z., Hashemi, A., De Plano, L. M., Gholipourmalekabadi, M. & Seifalian, A. Bacteriophage Based Biosensors: Trends, Outcomes and Challenges. *Nanomaterials* **10**, 501 (2020).

285. El-Shibiny, A., El-Sahhar, S. & Adel, M. Phage applications for improving food safety and infection control in Egypt. *Journal of Applied Microbiology* **123**, 556–567 (2017).

286. Altintas, Z., Pocock, J., Thompson, K.-A. & Tothill, I. E. Comparative investigations for adenovirus recognition and quantification: Plastic or natural antibodies? *Biosensors and Bioelectronics* **74**, 996–1004 (2015).

287. Janczuk, M., Niedziółka-Jönsson, J. & Szot-Karpińska, K. Bacteriophages in electrochemistry: A review. *Journal of Electroanalytical Chemistry* **779**, 207–219 (2016).

288. Qi, H., Lu, H., Qiu, H.-J., Petrenko, V. & Liu, A. Phagemid Vectors for Phage Display: Properties, Characteristics and Construction. *Journal of Molecular Biology* **417**, 129–143 (2012).

289. Smith, G. P. & Petrenko, V. A. Phage Display. *Chem. Rev.* **97**, 391–410 (1997).

290. GUGLIELMINO, S. *et al.* Conformational mimotopes for detecting specific antibodies. (2024).

291. Zhang, X., Zhang, X., Gao, H. & Qing, G. Phage display derived peptides for Alzheimer's disease therapy and diagnosis. *Theranostics* **12**, 2041–2062 (2022).

292. Larbanoix, L. *et al.* Design and evaluation of a 6-mer amyloid-beta protein derived phage display library for molecular targeting of amyloid plaques in Alzheimer's disease: Comparison with two cyclic heptapeptides derived from a randomized phage display library. *Peptides* **32**, 1232–1243 (2011).

293. Sciuto, E. L., Petralia, S., Calabrese, G. & Conoci, S. An integrated biosensor platform for extraction and detection of nucleic acids. *Biotechnology and Bioengineering* **117**, 1554–1561 (2020).

294. Nikolaou, P. *et al.* Ultrasensitive PCR-Free detection of whole virus genome by electrochemiluminescence. *Biosensors and Bioelectronics* **209**, 114165 (2022).

295. Sciuto, E. L., Petralia, S., van der Meer, J. R. & Conoci, S. Miniaturized electrochemical biosensor based on whole-cell for heavy metal ions detection in water. *Biotechnology and Bioengineering* **118**, 1456–1465 (2021).

296. Calorenni, P. *et al.* Silicon-Based Sensing Surface for Alzheimer's Disease Diagnosis by Phages Probes. *Advanced Materials Interfaces* **11**, 2300785 (2024).

297. Affinity of Protein A/G for IgG Types from Different Species | NEB. https://www.neb.com/en/tools-and-resources/selection-charts/affinity-of-protein-ag-for-igg-types-from-different-species.

298. Iijima, M., Somiya, M., Yoshimoto, N., Niimi, T. & Kuroda, S. Nano-visualization of oriented-immobilized IgGs on immunosensors by high-speed atomic force microscopy. *Sci Rep* **2**, 790 (2012).

299. Strasser, J. *et al.* Unraveling the Macromolecular Pathways of IgG Oligomerization and Complement Activation on Antigenic Surfaces. *Nano Lett.* **19**, 4787–4796 (2019).

300. Preiner, J. *et al.* IgGs are made for walking on bacterial and viral surfaces. *Nat Commun* **5**, 4394 (2014).

301. Yagi, H., Takahashi, N., Yamaguchi, Y. & Kato, K. Temperature-dependent isologous Fab-Fab interaction that mediates cryocrystallization of a monoclonal immunoglobulin G. *Mol Immunol* **41**, 1211–1215 (2004).

302. Ido, S. *et al.* Immunoactive two-dimensional self-assembly of monoclonal antibodies in aqueous solution revealed by atomic force microscopy. *Nature Mater* **13**, 264–270 (2014).

303. Chua, C. E. L. & Tang, B. L. miR-34a in Neurophysiology and Neuropathology. *Journal of Molecular Neuroscience* **67**, 235–246 (2019).

304. Modi, P. K., Jaiswal, S. & Sharma, P. Regulation of neuronal cell cycle and apoptosis by microRNA 34a. *Molecular and Cellular Biology* **36**, 84–94 (2016).

305. Cogswell, J. P. *et al.* Identification of miRNA changes in Alzheimer's disease brain and CSF yields putative biomarkers and insights into disease pathways. *Journal of Alzheimer's Disease* **14**, 27–41 (2008).

306. Jian, C. *et al.* miR-34a knockout attenuates cognitive deficits in APP/PS1 mice through inhibition of the amyloidogenic processing of APP. *Life Sciences* **182**, 104–111 (2017).

307. Wang, X. *et al.* miR-34a, a microRNA up-regulated in a double transgenic mouse model of Alzheimer's disease, inhibits bcl2 translation. *Brain Research Bulletin* **80**, 268–273 (2009).

308. Zhao, Y. *et al*. The potential markers of circulating micrornas and long non-coding RNAs in Alzheimer's disease. *Aging and Disease* **10**, 1293–1301 (2019).

309. Congur, G. & Erdem, A. PAMAM dendrimer modified screen printed electrodes for impedimetric detection of miRNA-34a. *Microchemical Journal* **148**, 748–758 (2019).

310. Nunomura, A. & Perry, G. RNA and Oxidative Stress in Alzheimer's Disease: Focus on microRNAs. *Oxidative Medicine and Cellular Longevity* **2020**, 2638130 (2020).

311. Serrano, V. M., Silva, I. S. P., Cardoso, A. R. & Sales, M. G. F. Carbon Electrodes with Gold Nanoparticles for the Electrochemical Detection of miRNA 21-5p. *Chemosensors* **10**, 189 (2022).

312. Mohammadi-Yeganeh, S. *et al*. Development of a robust, low cost stem-loop real-time quantification PCR technique for miRNA expression analysis. *Molecular Biology Reports* **40**, 3665–3674 (2013).

313. Scopus - Document details - Differential expression of microRNAs in Alzheimer's disease brain, blood, and cerebrospinal fluid | Signed in. https://www.scopus.com/record/display.uri?eid=2-s2.0-85071722717&origin=inward&txGid=3d1b3fd206f19d298886e8c2386ee1eb.

314. van den Berg, M. M. J. *et al*. Circulating microRNAs as potential biomarkers for psychiatric and neurodegenerative disorders. *Progress in Neurobiology* **185**, (2020).

315. Wu, Y. *et al*. Circulating microRNAs: Biomarkers of disease. *Clinica Chimica Acta* **516**, 46–54 (2021).

316. Galimberti, D. *et al*. Circulating miRNAs as potential biomarkers in alzheimer's disease. *Journal of Alzheimer's Disease* **42**, 1261–1267 (2014).

317. Turchinovich, A., Weiz, L., Langheinz, A. & Burwinkel, B. Characterization of extracellular circulating microRNA. *Nucleic Acids Research* **39**, 7223–7233 (2011).

318. Nagaraj, S., Zoltowska, K. M., Laskowska-Kaszub, K. & Wojda, U. microRNA diagnostic panel for Alzheimer's disease and epigenetic trade-off between neurodegeneration and cancer. *Ageing Research Reviews* **49**, 125–143 (2019).

319. Frontiers | The Regulation of microRNAs in Alzheimer's Disease. https://www.frontiersin.org/journals/neurology/articles/10.3389/fneur.2020.00288/full.

320. Yang, L., Lopes, I. C. & Vadgama, P. Self-cleaning sensors based on thermoresponsive polymeric film modified screen-printed platinum electrodes. *Chemical Engineering Journal* **474**, 145932 (2023).

321. Zhang, W., Bas, A. D., Ghali, E. & Choi, Y. Passive behavior of gold in sulfuric acid medium. *Transactions of Nonferrous Metals Society of China* **25**, 2037–2046 (2015).

322. Kang, X. *et al.* A graphene-based electrochemical sensor for sensitive detection of paracetamol. *Talanta* **81**, 754–759 (2010).

323. Zheng, M. *et al.* Electrocatalytical oxidation and sensitive determination of acetaminophen on glassy carbon electrode modified with graphene–chitosan composite. *Materials Science and Engineering: C* **33**, 1514–1520 (2013).

324. Konopka, S. J. & McDuffie, Bruce. Diffusion coefficients of ferri- and ferrocyanide ions in aqueous media, using twin-electrode thin-layer electrochemistry. *Anal. Chem.* **42**, 1741–1746 (1970).

325. Díaz, V., Real, S., Téliz, E., Zinola, C. F. & Martins, M. E. New experimental evidence on the formation of platinum superactive sites in an electrochemical environment. *International Journal of Hydrogen Energy* **34**, 3519–3530 (2009).

326. Calorenni, P. *et al.* PCR-Free Innovative Strategies for SARS-CoV-2 Detection. *Advanced Healthcare Materials* **12**, 2300512 (2023).

CHAPTER 5

Pubblications and Education

5. Pubblications and Education

5.1. Published papers

1. Calorenni P, Bella G, Nicolò MS, Sciuto EL, Balli MV, Valenti G, Gritti T, Varani S, Prodi L, Conoci S. Advanced DNA-Gold Biointerface for PCR-free molecular detection of Leishmania Infantum. Adv Mater. Interf. 2024 doi: https://doi.org/10.1002/admi.202400642. Epub 2024 Nov 7.
2. Calorenni P, Paratore V, Rizzo MG, De Plano LM, Condorelli GG, De Luca G, Oddo S, Guglielmino S, Sciuto EL, Conoci SLeonardi AA, Sciuto EL, Rizzo MG, Faro MJL, Fazio B, Irrera A, Conoci S. Silicon-Based Sensing Surface for Alzheimer's Disease Diagnosis by Phages Probes. Adv. Mater. Interf. 2023 doi: https://doi.org/10.1002/admi.202300785. Epub 2023 Dec 14.
3. Calorenni P, Leonardi AA, Sciuto EL, Rizzo MG, Faro MJL, Fazio B, Irrera A, Conoci S. “PCR-Free Innovative Strategies for SARS-CoV-2 Detection. Adv Healthc Mater. 2023. doi: 10.1002/adhm.202300512. Epub 2023 Jul 25.

5.2. Proceedings

1. Paolo Calorenni, Maria Giovanna Rizzo, Laura Maria de Plano, Antonio A. Leonardi, Vincenzo Paratore, Guglielmo Guido Condorelli, Alessia Irrera, Emanuele L. Sciuto, Salvatore Oddo, Sabrina Conoci “ Innovative Silicon-Based Sensing Strategy for the Alzheimer’s Disease Detection by Phage Display”,Proceedings of the MDPI proceedings journal, March 2024. DOI: https://doi.org/10.3390/proceedings2024097065

5.3. Conferences

1. Sciuto EL, Calorenni P(poster), Gritti T, Varani S, Valenti G, Balli MV, Prodi L and Conoci S “Electrochemical detection of pathogen nucleic acid for bio-sensing application” Eurosensors Conference 2024, Debrecen, Hungary, September 1-4 2024

2. Calorenni P(poster), De Plano LM, Caccamo A, Sciuto EL, Oddo S, Conoci S “PCR-free detection of miRNA biomarkers for neurodegenerative disorders” Eurosensors Conference 2024, Debrecen, Hungary, September 1-4 2024
3. Calorenni P(poster), Sciuto EL, Balli MV, Valenti G, Paolucci F, Prodi L, Conoci S “ECL-Based detection of pathogen genome for biosensing application” Lights Interactions with low-dimensional systems Messina, Italy, May 20 2024
4. Calorenni P(oral) “Study of solid-state DNA chemical properties on gold”, AISEM Conference 2023 Bologna, Italy, February 07-09 2024
5. P. Calorenni (oral) “Isoelectric and Grafting Density Profiling of Si- and Au-Immobilized Nucleic Acid”. Eurosensors Conference 2023, Lecce, Italy, September 10-13 2023

5.4. Courses attempting and school

1. Scuola di dottorato, “New trends in the application of Photonics”, Catania (CT), 11-15 Novembre 2024
2. Seminario – Probing the curious chemistry in micro – and – nanodroplets via nanoelectrochemistry – tenuto dal Prof. Jeffrey E. Dick, Bologna, 09 Giugno 2023
3. PhD visiting at University of Bologna (G. Ciamician), April 1st – July 1st, 2023, Bologna, Italy. Topic:
    - application of novel PCR-free biosensor for the early diagnosis of virus infection via electrochemistry and electrochemioluminescence
4. Scuola di Dottorato, “II Scuola Nazionale Sensori Chimici”, Palazzo Feltrinelli, Gargnano (BS), 17-19 Ottobre 2022

Acknowledgments

First of all, I would like to thank myself for reaching this unexpected goal. These have been three stimulating years in which I have learned to rely on my abilities and become a key figure in the lab.

I would like to thank my girlfriend Annamaria who has helped me during the most difficult moments of this journey for three years, especially when I thought about giving up.

I would like to thank Prof. Sabrina Conoci for the great opportunity, she gave me, to improve my scientific background and knowledges during these 3 years Ph.D. project.

Also, thanks to my colleagues who have helped me and taught me everything I needed to work in this wonderful multidisciplinary scientific field of nanotechnology.

Last but not least, thank to my beautiful family, composed by my sister Giusy, my mom Graziella and my dad Francesco who taught me how to face life adversities believing in myself and my abilities.

La borsa di dottorato cofinanziata con risorse del
Programma Operativo Nazionale Ricerca e Innovazione 2014-2020 (CCI 2014IT16M2OP005),
risorse Fondo Sociale Europeo REACT-EU, Azione IV.4 “Dottorati e contratti di ricerca su tematiche dell’innovazione” e Azione IV.5 “Dottorati su tematiche Green”